Magnetic Susceptibility Separation in Brain

by

Javad Hamidi Esfahani

A thesis submitted in partial fulfillment of the requirements for the degree of

Master of Science

Department of Biomedical Engineering
University of Alberta

Abstract

Quantitative susceptibility mapping (QSM) has become an area of intense interest in brain imaging due to its ability to quantify tissue magnetic susceptibility. QSM deploys a gradient echo sequence to produce phase images that are sensitive to susceptibility differences, which can then be processed into a susceptibility map. QSM exhibits promising performance in deep gray matter where iron-rich regions exist. Iron is paramagnetic and appears in QSM results as a positive source. In addition, QSM showed sensitivity to myelin due to its diamagnetic susceptibility. Myelin is abundant in white matter tracts, for example. Thus, QSM has been applied to study changes in iron and myelin in the brain. Of particular interest is the demyelinating disease multiple sclerosis (MS). However, in the same voxel, changes in both iron and myelin can occur which have confounding effects on the resulting mean susceptibility. For example, a loss of myelin or a gain in iron could have similar increases on the net susceptibility.

The challenge for conventional QSM has been distinguishing iron deposition (increasing paramagnetic component) from demyelination (decreasing diamagnetic component). Recently susceptibility separation methods were introduced as a means to solve the problem. The methods incorporate the reversible component of transverse relaxation known as R2' and assume diamagnetic and paramagnetic dephasing effects have similar contributions to R2', while they have opposing effects on the phase used for QSM. Utilizing both R2' and QSM it becomes possible to separate the dia- and paramagnetic components. However, the susceptibility separation methods

have only recently been introduced and there is no knowledge on the reliability of such methods. Particularly for longitudinal studies, high repeatability is necessary for any biomarker.

In this work, background information to understand susceptibility separation is introduced in Chapter 1. Then in Chapter 2, a study of scan-rescan repeatability is performed on healthy subjects. Optimal parameter choices for susceptibility separation are first investigated. In particular, variation of the relaxometric coefficient (D_r) was assessed in deep gray matter and white matter. This coefficient determines the relative weights of R2' with respect to absolute susceptibility values, and has typically been kept constant. The results show the optimal D_r value tends to be larger for dominant component and smaller for minor component e.g. in deep gray matter where strong paramagnetic sources exist D_r is larger for paramagnetic component than diamagnetic. With optimal choices, the repeatability of the method is examined using Bland-Altman plots, scan-rescan correlations and interclass correlation coefficients (ICC). The results suggest that separation methods are not as repeatable as conventional QSM in both deep gray matter and white matter. Conventional QSM had the largest average ICC scores of 0.97 and 0.88 in deep gray matter and white matter respectively. The separated paramagnetic component had ICC of 0.85 and 0.64 in deep gray matter and white matter, respectively. Diamagnetic components had the least average ICC scores of 0.45 and 0.45 in deep gray matter and white matter. However, the separation methods do offer qualitative distinction of paramagnetic and diamagnetic components. Two limitations were found. First, the R2' map is vulnerable to noise, thus its combination use with conventional QSM may propagate the noise into the separation maps. Second, the combination of multiple scans requires exact registration which is difficult to achieve for lower resolution imaging.

In Chapter 3, the conclusions of this thesis are discussed along with limitations and directions for the future. Overall susceptibility separation is an exciting new research field that is still in its infancy. Our work has illustrated both its current flaws and its promise for future examination of myelin and iron in the human brain.

Preface

This thesis is an original work by Javad Hamidi Esfahani. No part of this thesis has been previously published.

Acknowledgment

This page is the most qualitative part of the thesis written to thank people who had a part in this journey.

Maybe it is more than an hour at midnight that I am thinking of how I should start expressing my gratitude toward Dr. Alan Wilman, my supervisor. On the day I met him in RTF, I knew I was so lucky. His continuous supports and advices during my degree always shed light on the path I was taking. It was unfortunate that COVID-19 cut all the in-person contacts but he never stopped his supports. He professionally changed my project at the right time when all the student and patient access to MR center were stopped. In my first experience of abstract submission, he helped me to revise the text and provided me with insightful feedback. All in all, looking back to see the past, it was truly a pleasure to work with Dr. Wilman. I'd like to thank Nashwan Naji who was more than a colleague to me, sometimes he was my mentor. I'd like to thank Peter Seres for his technical assistance. Also, I'd like to thank my office mate, Ziyan Zhu, and other members of the group as I enjoyed working with them.

Last but not least, I'd like to thank my wife, Mahsa, who patiently supported me during the pandemic and my degree program. I'd like to thank my parents and friends that were supporting me throughout this journey.

Table of Contents

1 Introduction 1

1.1 Principals of Magnetic Resonance Imaging 1

1.2 RF Pulse, Gradients and Spatial Encoding 3

1.3 K-Space and Spatial Decoding 6

1.4 Parallel Imaging 7

1.5 Quantitative Susceptibility Mapping 8

1.5.1 Phase Unwrapping and Field Shift Map 11

1.5.1.1 Laplacian Phase Unwrapping 12

1.5.1.2 ROMEO 12

1.5.1.3 Field Fitting 14

1.5.2 Background field removal 15

1.5.3 Dipole Inversion 18

1.5.3.1 Truncated K-space Division (TKD) 19

1.5.3.2 Image Space Regularization Based Methods 19

1.6 Quantitative R2' Measurement 22

1.7 Susceptibility Separation Techniques 25

1.8 Motivation for the Thesis 30

References 31

2 Repeatability of Susceptibility Separation in Brain 38

2.1 Introduction 38

2.2 Methods 40

2.2.1 Data Acquisition 40

2.2.2 Post Processing and Registration 41

2.2.3 Susceptibility Separation Model 42

2.2.4 Statistical Analysis 44

2.3 Results 45

2.4 Discussion 55

2.5 Conclusion 59

References 60

3 Conclusion 66

3.1 Limitations 67
3.2 Future Directions 69
References 71
Bibliography 74

List of Tables

Table 1: Mean (M) relative difference error (%) and percent standard deviation (S) of paramagnetic maps over all subjects for different D_r values. The optimal values are bolded..... 54

Table 2: Mean (M) relative difference error (%) and standard deviation (S) of diamagnetic maps over all subjects for different D_r values. The optimal values are bolded..... 55

List of Figures

Figure 1.1: Components of magnetization vector in longitudinal and transverse planes. 2
Figure 1.2: Complex number presentation..... 3
Figure 1.3: Pulse sequence for a 3D image is depicted with slice selection..... 5
Figure 1.4: An example of image in spatial space and in k-space..... 7
Figure 1.5: The magnetic field created by a unit magnetic dipole in polar coordinate 11
Figure 1.6: Comparison of ROMEO and Laplacian. 14
Figure 1.7: Different background removal methods has been applied to a subject. 18
Figure 1.8: Different susceptibility inversion methods applied on local field shift map..... 21
Figure 1.9: QSM general pipeline..... 22
Figure 1.10: T2 and T2* Decay rates of magnitude component..... 24
Figure 1.11: The conventional QSM methods and Separation methods susceptibility map reconstructions 25
Figure 1.12: Effects of paramagnetic and diamagnetic susceptibility sources on relaxation decay. 27
Figure 1.13: Resulting susceptibility maps of the Shin susceptibility separation method as well as relaxation maps. 29
Figure 2.1: Susceptibility separation and its base images in normalized MNI space..... 46
Figure 2.2: Susceptibility separation and its base images of one subject. 47
Figure 2.3: Results of conventional QSM and the separation method on two scans of a subject 48
Figure 2.4: Scatter plots from both scans illustrate the range of values with all methods plotted in each panel..... 50
Figure 2.5: BA plots for the 4 DGM and 3 WM regions showing the four susceptibility outcomes, as well as R2' BA plot for the 3 WM regions 51
Figure 2.6: The ICC scores of DGM and WM regions..... 53
Figure 2.7: The correlation and BA plots of relaxometric coefficient..... 54
Figure 2.8: The difference maps of a subject from scan-rescan illustrating an artifact originating from the R2* map. 57

1 Introduction

This chapter introduces some of the basics of Magnetic Resonance Imaging (MRI) including how the signal is formed, Bloch equations, frequency and phase encoding gradients. After the basics of MRI, the necessary information to understand susceptibility separation is introduced.

1.1 Principals of Magnetic Resonance Imaging

Standard MRI is focused on acquiring images from hydrogen atoms and is well described in text books (Robert W. Brown, 2014, Liang Z-P, 2000, Bernstein MA, 2005, Donald W McRobbie, 2017). It takes advantage of magnetic moment of protons available in our body coming mostly from water, but also from small fat molecules.

A proton has a magnetic moment of μ (TW Redpath, 1988, Slichter CP, 1990) specified by:

$$\mu = \gamma J \tag{1.1}$$

$\vec{J}$ is the angular moment of the proton and γ is the gyromagnetic ratio. The value for γ is found experimentally and for proton is $\gamma = 2.675 \times 10^8 \frac{rad}{s\,T}$. The reason that imaging hydrogen is more feasible rather than other atoms which have a magnetic momentum such as oxygen, sodium, etc. is that hydrogen concentration is at least 1000 times more than them in the human body. As a result, the signal is stronger.

MR signal is ruled by a set of equations called Bloch equations. Basically, Bloch equations predict the behaviour of magnetic spins in the presence of external magnetic fields. Bloch equations can be described as follows (Robert W. Brown, 2014, Bloch, 1946):

$$\boldsymbol{M} = \sum \mu_{\boldsymbol{i}} \tag{1.2}$$

$$\frac{d\boldsymbol{M}}{dt} = \gamma \boldsymbol{M} \times \boldsymbol{B} - \frac{\boldsymbol{M_T}}{T_2} - \frac{(M_Z - M_{Z0})\boldsymbol{z}}{T_1} \tag{1.3}$$

Where **M** is the total magnetization vector for the sample and T_1 and T_2 are spin-lattice and spin-spin relaxation time respectively. $\mathbf{M}_T$ is transversal magnetization which is magnetization is x and y directions. **B** is the existing magnetic field and M_z is the total magnetization in z direction. Note that the typical assumption is that static magnetic field is in z direction it is also called longitudinal direction as well. Finally, M_{z0} is the initial magnetization in z direction (Khan, 2013). Figure 1.1 illustrates a picture of magnetization vector with its longitudinal and transverse components.

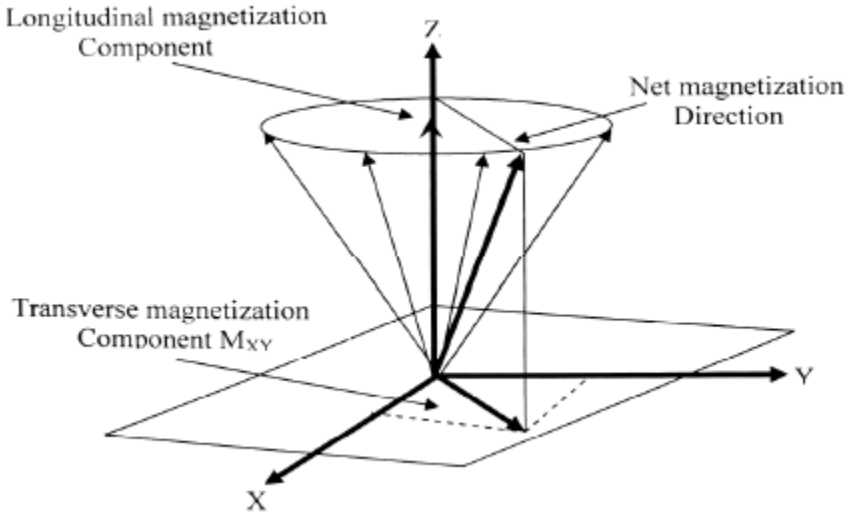

Figure 1.1: Components of magnetization vector in longitudinal and transverse planes.

By solving the differential equation (1.3) these two important results are achieved when the spin is in a static field:

$$M_z(t) = M_{z,eq} - \left(M_{z,eq} - M_{z0}\right)e^{-\frac{t}{T_1}} \tag{1.4}$$

$$\boldsymbol{M}_T(t) = \boldsymbol{M}_{T0}e^{-(\frac{t}{T_2}+iw_0t)} \tag{1.5}$$

$M_{z,eq}$ is the longitudinal magnetization in equilibrium and $\mathbf{M}_{T0}$ is the initial magnetization in transverse plane. w_0 is Larmor frequency:

$$w_0 = -\gamma B_z \tag{1.6}$$

B_z is the static field present, in this work a 3T Prisma scanner has been used. As a result, in this research the static field is 3T.

In MRI, signal received by receiver coils is in the rotating transverse magnetization which precesses in the transverse plane in the presence of the main static field, giving rise to a rotating magnetization that can produce a current in the coils. The longitudinal component (polarization) does not rotate and hence produces no new signal, though indirectly the original longitudinal component is the original source of the transverse signal. Since the transverse magnetization vector is in 2D plane it can be represented as a complex number which has a real and an imaginary part. The final output can be considered in form of magnitude and phase as M exp(iφ). In this case magnitude and phase can represent the complex number (figure 1.2). Typically the final generated images may include a magnitude and a corresponding phase image.

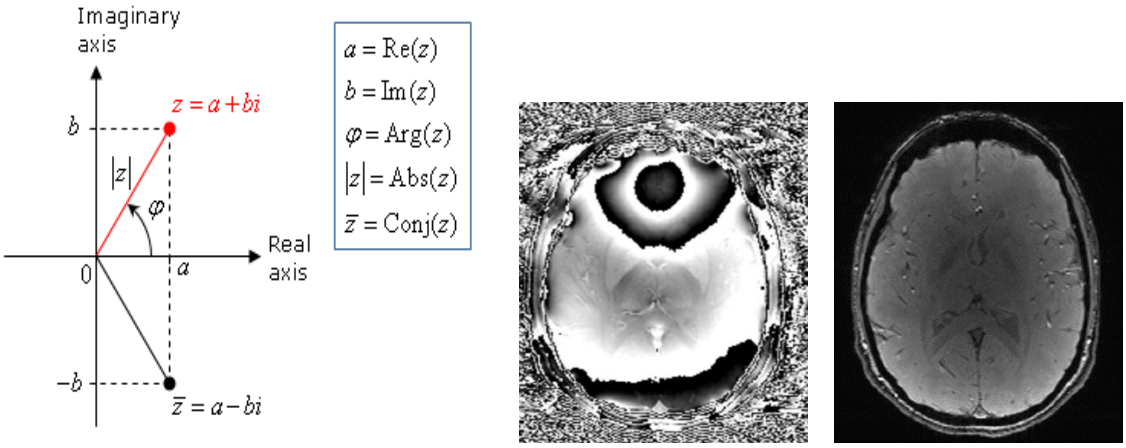

Figure 1.2: Complex number presentation can be in form of real and imaginary as well as magnitude and phase (left), the phase image (middle) and the magnitude image (right)

1.2 RF Pulse, Gradients and Spatial Encoding

In order to rotate longitudinal magnetization into the transverse plane, RF pulses are needed (Lauterbur PC, 1973, Liang Z-P, 2000, Mansfield P, 2001). The RF pulse is an alternating magnetic field perpendicular to static field causing the magnetization vector be tipped down into transverse plane when it is on resonance. The RF field is typically 1000 times weaker than the static field. The area under the RF pulse envelope is related to the flip angle which can be adjusted by altering the length of the RF pulse or its magnitude, to achieve the desired flip angle. Based on equation (1.6) the rotation frequency and flip angle can be derived for a simple rectangular pulse of duration Δt:

$$w_{RF} = \gamma B_1 \tag{1.7}$$

$$\alpha = w_{RF}\Delta t \tag{1.8}$$

B_1 is the magnetic field caused by RF pulse. After playing the RF pulse out, all the protons are tipped with α degree toward transverse plane. Since all the spins (magnetization vectors) are precessing around B_0, the B_1 field needs to rotate with the same precessional frequency for maximum effect. This frequency is called the Larmor frequency (equation 1.6). For simplicity we assume that all the vectors are in a rotating frame which is rotating around B_0 with Larmor frequency (Rabi II, 1954, Redfield AG, 1955). Therefore, using this rotating frame the transverse magnetization stationary in transverse plane.

Since the spins are precessing at the Larmor frequency around the external magnetic field direction, applying an RF pulse at the Larmor frequency can tip the spins into the transverse plane regardless of location. To overcome this issue a slice or slab selection gradient is applied during the RF pulse which causes a linear magnetic field variation in the slice select direction. Then the RF with the desired offset frequency is applied to select the slice of interest. Typically, the RF pulse is accompanied by amplitude modulated pulses that generate signal over a specific slice-selection bandwidth.

In order to acquire image in k-space, MR systems use gradient pulses. These pulses are used for encoding each spatial location within a slice. The gradient pulses have a linear relationship with spatial location (Paschal CB, 2004; Ernst RR, 2011). As a result, a spatially varying field is experienced by spins depending on the location. Note the field components are in direction of B_0, while the gradient of the field can take any direction

$$B_z(x, y, z) = B_0 + G(x, y, z) \,.\, [x, y, z] \tag{1.9}$$

$$\Delta w_z = \gamma \, G(x, y, z) \,.\, [x, y, z] \tag{1.10}$$

Equation (1.10) explains how these gradient pulses cause a difference in precessing frequency in different locations. With taking advantage of the gradient pulses acquiring an image and then reconstructing it becomes feasible.

Assuming a 3D sequence is being used, then there are 3 gradient pulses in each direction; frequency, phase and slice directions corresponding to x, y and z directions respectively. A frequency gradient pulse is a continuous pulse occurring simultaneously with sampling in x direction with a specific time interval, assuming a rectangular gradient pulse of length τ_x, the new phase change from the gradient would be

$$\varphi_x = -\gamma G_x x \, \Delta t_x \tag{1.11}$$

Where Δt_x is the sampling rate in second (s) and G_x is the gradient in x direction. For phase and slice encoding following equations are used, again assuming perfect rectangular gradient pulses:

$$\varphi_y = -\gamma G_y y \, \tau_y \tag{1.12}$$

$$\varphi_z = -\gamma G_z y \, \tau_z \tag{1.13}$$

These gradients are played out before frequency encoding and cause the spins to have an initial phase shift. Sometimes, a shaped RF pulse accompanied with slice selection pulse in z direction (main magnetic field direction) is desired in order to tip down the spins in a specific region. In figure 1.3 a pulse sequence for 3D imaging is shown.

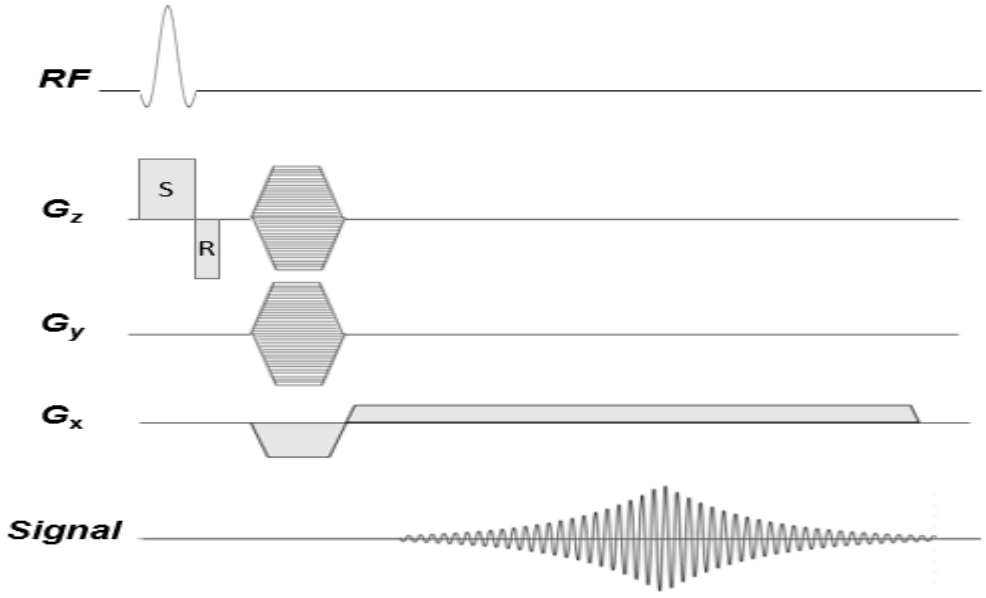

Figure 1.3: Pulse sequence for a 3D image is depicted with slice selection. Phase encoding increases every repetition time and frequency encoding has a negative lobe causing the acquired signal to reach its maximum at the echo time. The shaped RF pulse is played out with a slab selection gradient in order to

only tip down the spins in the region of interest. The slab selection gradient is indicated with 'S' and is followed by a refocussing lobe (R).

To ensure no aliasing, the Nyquist constraint on sampling requires that the sampling rate be at least twice the maximum frequency that occurs on the edge of the slice:

$$1 = \gamma G_x FOV_x \, \Delta t \tag{1.14}$$

Where FOV is total field of view which is the maximum size captured in the image.

1.3 K-Space and Spatial Decoding

The signal acquired by gradients is in k-space which is different from image space (spatial space):

$$S = \iiint_{FOV_-}^{FOV_+} M(x,y,z)\, e^{-i(\gamma G_x x\, \tau_x + \gamma G_y y\, \tau_y + \gamma G_z z\, \tau_z)} dxdydz \tag{1.15}$$

A rectangular k-space element is defined as:

$$k = \gamma G \tau \tag{1.16}$$

Combining equations (1.15) and (1.16) yields:

$$S(k_x, k_y, k_z) = \iiint_{FOV_-}^{FOV_+} M(x,y,z)\, e^{-i(k_x x + k_y y + k_z z)}\, dxdydz \tag{1.17}$$

Equation (1.17) shows the measured signal is the Fourier transform of the spins in the sample. Therefore, in order to reconstruct the image the inverse Fourier transform needs to be taken:

$$M(x,y,z) = \iiint_{k_-}^{k_+} S(k_x, k_y, k_z)\, e^{i(k_x x + k_y y + k_z z)}\, dk_x dk_y dk_z \tag{1.18}$$

For calculating the inverse Fourier transform in discrete domain, k-space has to be filled with evenly sampled space in each direction. Therefore, k-space steps for each dimension should be as follows if using rectangular gradient pulses:

$$\begin{cases} \Delta k_x = \gamma\, G_x\, \Delta t \\ \Delta k_y = \gamma\, \Delta G_y\ \ \tau_y \\ \Delta k_z = \gamma\, \Delta G_z\, \tau_z \end{cases} \tag{1.19}$$

Note frequency encoding gradient pulse has a trapezoidal part which adjust echo time to be at the center of k-space (Tabon SS, 2001). Sampling starts after the trapezoidal part is done:

$$k = \int_0^{\tau_1} G_x(t)\, dt \tag{1.20}$$

Note that the important relationship between k-space and FOV exists. It can be derived by combining equations (1.19) and (1.14):

$$\begin{cases} \Delta k_x = \frac{1}{FOV_x} \\ \Delta k_y = \frac{1}{FOV_y} \\ \Delta k_z = \frac{1}{FOV_z} \end{cases} \tag{1.21}$$

In figure 1.4 the examples of an image in the spatial domain and its k-space domain are shown. Note the center of k-space has the largest amplitude since echo time (TE) happens there.

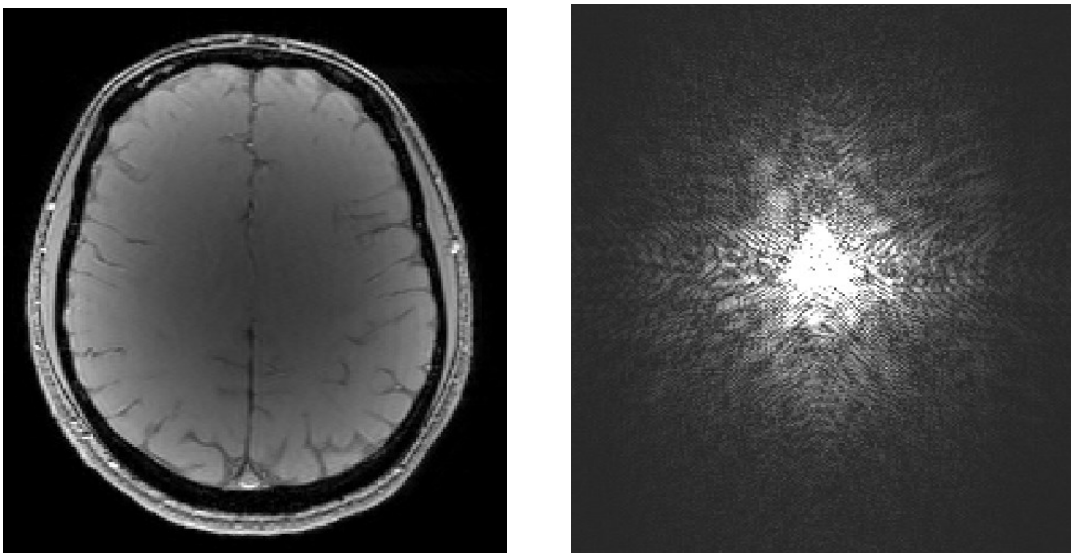

Figure 1.4: An example of image in spatial space (left) and in k-space (right)

1.4 Parallel Imaging

To perform parallel imaging the reconstruction procedure needs to incorporate the spatial information from each receiver coils. Having the information then scan time can be reduced by a

specific factor. Sensitivity Encoding (SENSE) (Pruessmann KP, 1999) is a common method taking advantage of this feature. With the simple assumption that there are two receiver coils, SENSE halves the FOV in phase encoding direction hence the scan time becomes half. With the reduced FOV, aliasing happens but since it is predictable, SENSE can remove the aliasing. For an arbitrary point r_A in the reduce FOV, each receiver coil receives a signal from r_A and r_B from outside of FOV due to aliasing:

$$\begin{cases} Coil\ 1: S_1 = C_1(r_A)S_A + C_1(r_B)S_B \\ Coil\ 2: S_2 = C_2(r_A)S_A + C_2(r_B)S_B \end{cases} \tag{1.22}$$

C_1 and C_2 are the coil sensitivity for coil 1 and coil 2, respectively. Obtaining the two signals from receivers, aliasing can be removed and the equation can be solved for S_A and S_B.

Another commonly used method is Generalized Autocalibrating Partially Parallel Acquisitions (GRAPPA) (Griswold MA, 2002). Whereas SENSE tries to retrieve the image from an aliased image, GRAPPA generates the missing lines of k-space from an undersampled data in k-space (Deshmane, 2012). GRAPPA relies on the fact that every image has repetitive patterns which can be predicted. The patterns are due to natural convolution operation that is done by receiver coils. Therefore, the information in the missing lines can be obtained from their neighbourhood. The combination of the adjacent lines is done with weighting each point in k-space with the coil's sensitivity matrix in k-space. Since the k-space information for each coil is obtained during every separate scan, it is called an autocalibrating method.

1.5 Quantitative Susceptibility Mapping

Magnetic susceptibility χ is a tissue property that describes the tendency of a material to be magnetized when interacting with an external field (Wang Y, 2015). This property is inherit and without dimensions, it is usually measured in ppm or ppb. In general, this value can be measured in microscopic and macroscopic (bulk) sizes but since in MRI the value for a voxel is important the bulk value is commonly used. Naturally three different types of susceptibility exist. Ferromagnetism is found in metals such as iron and nickel, and is very rare and happens in just a few metals and their alloys. When ferromagnetic item is placed in a magnetic field, its unpaired

electrons are oriented in the direction of the external magnetic field and add up their magnetic dipole moments causing the item to become a magnet. The ferromagnetic material often retain their orientation even after removing the external magnetic field and exhibit more non-linear behaviors with respect to external magnetic field. The second type is paramagnetism which is a weaker state of ferromagnetism and can be found in materials such as aluminium, oxygen. When an external magnetic field is applied the unpaired electron spins are oriented in direction of external magnetic field due to the torque provided by the field. When the external field is removed the spins return to their random positions due to thermal agitation hence, the dipole magnets in different directions cancel out each other and the item is not a magnet anymore. The last group is called diamagnetic materials which their induced internal magnetic field opposes the external magnetic field. The electrons of every material can be considered as a current loop therefore according to Faraday's law they oppose to change of existing magnetic field. This property exists in all the materials due to the nature of electrons but it is very weak hence paramagnetism and ferromagnetism can overcome diamagnetism. When they are absent the material is diamagnetic.

For measuring susceptibility in human brain, since brain is mainly made of water, we expect that its tissues will have a susceptibility value similar to water which is -9.035ppm, with subtle differences arising from other sources (Arrighini & Moccia, 1968). Since we are in an almost uniform region of water, it is the relative difference from that which creates susceptibility contrast not the absolute susceptibility values. Therefore, in this thesis when we talk about susceptibility, it is the relative difference from the brain's average susceptibility value.

The most abundant susceptibility sources in brain are iron and myelin. Iron and myelin have positive and negative susceptibility values, respectively. Iron can be found in many forms in human body. Heme iron in blood as hemoglobin is paramagnetic in its deoxy form, but diamagnetic when it is oxyhemoglobin. About a third of iron stored in body is in the form of ferritin which is paramagnetic. Ferritin depositions in brain are mostly found in deep gray matter e.g. globus pallidus, putamen (Duyn JH, 2007; Varsha Jain, 2012). The myelin sheath wrapped around the axons is made of protein and lipid which are diamagnetic. Calcium is another diamagnetic source in brain but is not as abundant as iron and myelin. Calcium can be found in areas that are being calcified (Vinayagamani S, 2021).

From electromagnetic physics, magnetic field has linear relationship with permeability:

$$B = \mu H \tag{1.23}$$

The magnetic susceptibility value is related to permeability:

$$\mu = (1 + \chi)\mu_0 \tag{1.24}$$

In human body and brain the susceptibility sources are very subtle ($\chi \ll 1$) hence the changes in the external magnetic field are subtle as well. With combining Eq (1.23) and (1.24):

$$B = (1 + \chi)\mu_0 H \Rightarrow B_0 + \Delta B = \mu_0 H + \chi\mu_0 H \Rightarrow \Delta B = \chi B_0 \tag{1.25}$$

Equation (1.25) is very important since it proves the changes in the magnetic field is linear to both susceptibility value and the external field. As a result, the phase shift can be reformulated to reveal the effects of susceptibility:

$$\phi = -\gamma B T_E \Rightarrow \Delta\phi = -\gamma\chi B_0 T_E \tag{1.26}$$

Equation (1.26) mentions that by capturing the phase shifts, a susceptibility map can be derived. However, this holds for inside an object with a broad uniform surrounding, which is not applicable to human brain since there are many different tissues in it each in close distance. Furthermore, outside of susceptibility source the equation (1.25) doesn't hold. For simplicity, it is assumed that susceptibility sources are in shape of a sphere and act like magnetic dipoles. With this assumption the relationship between the changes in magnetic field and the susceptibility source changes to a convolutional expression (Marques JP, 2005; Li L, 2001; Salomir R, 2003; De Rochefort, 2008):

$$\Delta B = d(r) * \chi(r)\, B_0 \tag{1.27}$$

Where d(r) is the magnetic field of a unit dipole:

$$d(r) = \frac{3\cos^2\theta - 1}{4\pi r^3} \tag{1.28}$$

From equation (1.27) and (1.28) the conclusion can be drawn that ΔB = 0 at locations that d(r) = 0. This problem makes the inverse problem an ill posed problem. Figure 1.5 shows the dipole magnetic kernel in polar coordinates. The convolution in equation (1.27) is done by calculation of Fourier transform in k-space and the multiplication by the susceptibility map.

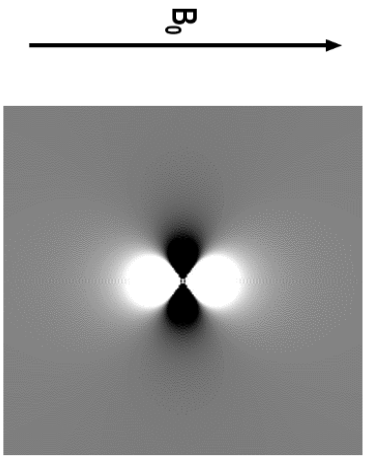

Figure 1.5: The magnetic field created by a unit magnetic dipole in polar coordinate

The main task in QSM is deriving the underlying susceptibility map that has caused the field shift. For this purpose, several steps has to be taken; phase unwrapping, background field removal and dipole inversion. In the following part each of these steps will be explained.

1.5.1 Phase Unwrapping and Field Shift Map

The final susceptibility map will be derived from the information lying in the phase map (De Rochefort L L. T., 2010; Liu J, 2012; Shmueli K, 2009). But before processing the phase map, the phase correction has to be done. Because of the protocols that MR machine algorithms have, the output phase is in the range of [-π π). Therefore, there might be several jumps when the phase value in the range increased or decreased beyond the range:

$$\varphi_{corrected} = \varphi_{measured} + k.2\pi \tag{1.29}$$

Where k is a signed integer. Equations (1.29) makes the final phase a map smooth and differentiable. There are several methods used is QSM for phase unwrapping such as path based methods which try to eliminate the jumps by looking through the adjacent voxel in a specific path (Abdul-Rahman HS, 2007; Bioucas-Dias JM, 2007; Jenkinson M, 2003). The methods suffer from noise i.e. if a significant noise exists in a voxel in a way that make its difference less than π with the adjacent voxel, the method cannot correct it (Robinson SD, 2017). Laplacian phase unwrapping is another method widely used in QSM (Li W A. A., 2014). Another newly introduced method is

rapid opensource minimum spanning tree algorithm (ROMEO) that is developed for ultra high magnetic fields and metal implantations (Dymerska, 2021).

1.5.1.1 Laplacian Phase Unwrapping

Based on the fact that Laplacian of corrected and measured phase are equal, the method calculates a Laplacian map of the measured phase and then derives the corrected map by taking inverse Laplacian:

$$\nabla^2\varphi_{corrected} = \cos(\varphi_{measured}).\nabla^2 sin(\varphi_{measured}) - sin(\varphi_{measured}).\nabla^2\cos(\varphi_{measured}) \quad (1.30)$$

While Laplacian method can handle the noisy singular voxels, it doesn't have an accurate performance in regions very close to susceptibility sources such as hemorrhage (Li W A. A., 2014). The Laplacian operation can be done in using matrix convolution in image space by defining the 3D kernel as follows (Ferdinand Schweser A. D., 2013):

$$\nabla^2 = \begin{bmatrix} 0 & 0 & 0 \\ 0 & \frac{1}{dz^2} & 0 \\ 0 & 0 & 0 \end{bmatrix}, \begin{bmatrix} 0 & \frac{1}{dx^2} & 0 \\ \frac{1}{dy^2} & c & \frac{1}{dy^2} \\ 0 & \frac{1}{dx^2} & 0 \end{bmatrix}, \begin{bmatrix} 0 & 0 & 0 \\ 0 & \frac{1}{dz^2} & 0 \\ 0 & 0 & 0 \end{bmatrix} \quad (1.31)$$

$$c = -\frac{2}{dz^2} - \frac{2}{dy^2} - \frac{2}{dx^2}$$

This convolution can be done faster by taking a Fourier transform and doing multiplication instead of convolution. The deconvolution also is done in Fourier domain by thresholding the inverse kernel in order to avoid dividing by zero (Biondetti, 2016):

$$FT\{\nabla^{-2}\} = \begin{cases} \frac{1}{FT\{\nabla^2\}} & FT\{\nabla^2\} > t \\ t & elsewhere \end{cases} \quad (1.32)$$

Laplacian method tends to eliminate some background fields as explained in 1.5.2.

1.5.1.2 ROMEO

ROMEO is path-based unwrapping phase method developed for both spatial and temporal phase unwrapping (Dymerska, 2021). As all the path-based methods, ROMEO finds the most reliable

path connecting all the voxels together. This helps the procedure by elimination of noisy connections. ROMEO at first, defines a quality map which consists of three different weightings using magnitude and phase images:

$$W_{i,j,t}^{\varphi,Spat} = 1 - \left| \frac{\Omega\left(\varphi_{i,t} - \varphi_{j,t}\right)}{\pi} \right| \tag{1.33}$$

$$W_{i,j,t}^{\varphi,Temp} = \max\left(0,1 - \left|\Omega\left(\varphi_{i,t-1} - \varphi_{j,t-1}\right) - \Omega\left(\varphi_{i,t} - \varphi_{j,t}\right).\frac{TE_{t-1}}{TE_t}\right|\right) \tag{1.34}$$

$$W_{i,j,t}^{M} = \frac{\min\left(M_{i,t}, M_{j,t}\right)}{\max\left(M_{i,t}, M_{j,t}\right)} \tag{1.35}$$

Where Ω is wrapping operator, i and j are neighbour voxels at time t. M is the magnitude of voxels. The temporal weights can be calculated in case gradient echo sequence. In a situation that the sequence has just one echo time this term can be omitted. The calculated weights are then multiplied and final weights are in the range of [0, 1] with 1 as the most reliable and 0 as the worst connection. The algorithm converts the weights into integer values and then sorts the weights to increase efficiency (Edelkamp S, 2011, Goodrich MT, 2014). ROMEO starts from a seed voxel which has the best reliability and then begins unwrapping throughout its path:

$$\theta_{2,t} = \varphi_{2,t} - 2\pi.round\left(\frac{\varphi_{2,t} - \theta_{1,t}}{2\pi}\right) \tag{1.36}$$

where $\varphi_{2,t}$ is the wrapped phase measured in voxel 2, $\theta_{1,t}$ is the phase in voxel 1, and $\theta_{2,t}$ is the unwrapped phase in voxel 2, all at a given time point *t*. Voxel 2 is subsequently marked as having been visited. New values are added to the queue, including the connections between voxel 2 and all of its neighbors not yet visited by the algorithm. When a new edge is drawn from the queue, a check is performed to see whether the voxels connected by the edge have both been visited: If they have, this edge is removed from the queue. The search for the minimal cost value and the unwrapping process are repeated iteratively until all voxels have been visited. ROMEO code is available in Julia language (Bezanson J, 2012). Path-based methods are used when accurate voxel values are necessary. Whereas Laplacian method causes some large variations across tissue (Robinson SD, 2017, Li W., 2011, Hsieh M-C, 2016, Liu S, 2013).

In addition to spatial unwrapping, temporal unwrapping has to be done as well. Temporal unwrapping is straightforward and done by checking for continuity of phase during echo times and correct the jump. Note that by doing temporal phase unwrapping, another spatial phase unwrapping might be needed. In some cases, such as some clinical applications that the image is acquired in just one echo, temporal unwrapping is not needed. Figure 1.6 is an example of Laplacian and ROMEO on the brain. ROMEO does not provide accurate values at the edge whereas Laplacian is more accurate at the edges.

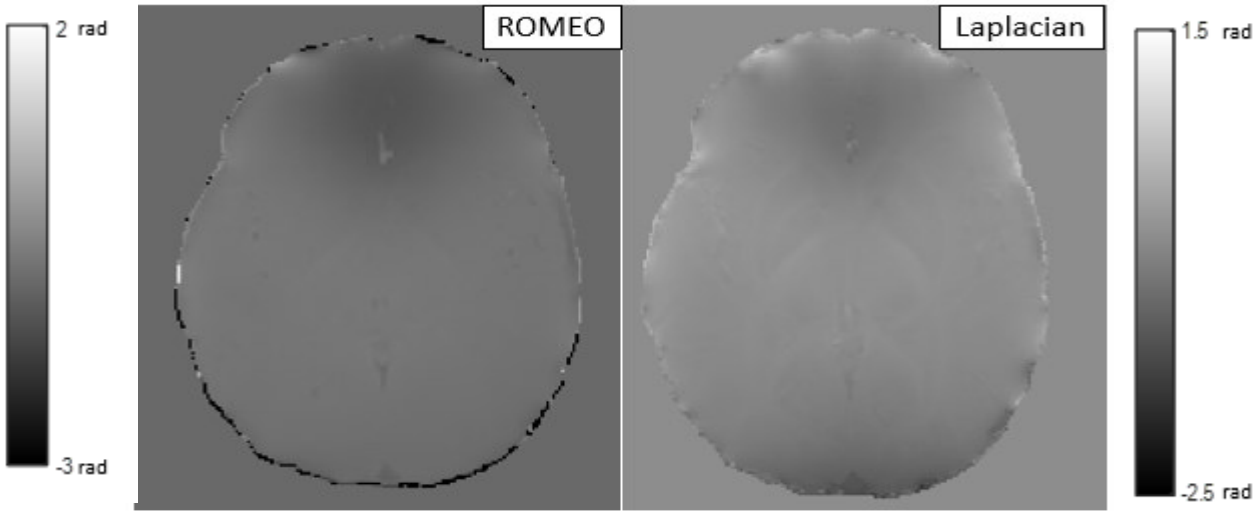

Figure 1.6: Comparison of ROMEO and Laplacian.

1.5.1.3 Field Fitting

When the phase map is unwrapped, total field shift map can be obtained by equation (1.37) for single echo and equation (1.38) for multi echo sequence (Gilbert G, 2012):

$$\Delta B = \frac{\varphi}{\gamma B_0 . TE} \tag{1.37}$$

$$argmin_{\Delta B} \left|\left| W(\varphi - \gamma B_0 . TE . \Delta B) \right|\right|^2 \tag{1.38}$$

W is the weight for the reliable and unreliable phases which is usually the magnitude map. The minimization equation put emphasize on initial echoes and reliable phases to obtain the total field

shift map. The scale of total shift map is parts per million (ppm) or parts per billion (ppb) as it is relative to the B_0.

1.5.2 Background field removal

Total field shift is summation of the external and local field shift:

$$\Delta B_{total} = \Delta B_{local} + \Delta B_{ext} \tag{1.39}$$

External field shift is caused by the inhomogeneity of the magnet field, air-tissue interface, chemical shift and imperfect coil shimming (Schenck, 1996). Local field shift is the component used for QSM and external field shift is not useful as it has no related information to susceptibility map. For filtering the external field shift out, several methods have been proposed. A widely used method is variable-radius sophisticated harmonic artifact reduction for phase data (V-SHARP) (BingWu, 2012) which is an extension SHARP method (Ferdinand Schweser A. D., 2011). SHARP uses symmetric spherical kernel ρ to eliminate the background field. Since susceptibility sources of the external field is outside of the FOV the spherical mean value can be used:

$$\Delta B_{ext} = \rho * \Delta B_{ext} \tag{1.40}$$

Combining equation (1.39) and (1.40):

$$(\delta - \rho) * \Delta B_{total} = \Delta B_{local} - \rho * \Delta B_{local} + \Delta B_{ext} - \rho * \Delta B_{ext}$$

$$\Delta B_S = (\delta - \rho) * \Delta B_{total}$$

$$\Delta B_S = (\delta - \rho) * \Delta B_{local} \quad , \tag{1.41}$$

SHARP defines a radius for ρ then constructs ΔB_S by transforming convolution operation to multiplication in Fourier domain then by applying an inverse kernel $(\delta - \rho)^{-1}$ to ΔB_S the local field shift map is yielded. In general a mask (M) is very common to define the region of interest (ROI). Therefore, the way that SHARP is done is shown:

$$K = F\{(\delta - \rho)\}$$

$$\Delta B_S = M\, F^{-1}\{\, K\, F\{\Delta B_{total}\}\}$$

$$\Delta B_{local} = M\, F^{-1}\{K^{-1}\, F\{\Delta B_S\}\} \tag{1.42}$$

F is Fourier transformation and F^{-1} is the inverse Fourier. The ρ kernel plays an important role as in regions close to boundary, a large radius will result in erosion of the image while at the central regions a small radius will result in poor accuracy. V-SHARP leverage a variable ρ kernel which is small close to boundary and large at center. The inverse convolution in V-SHARP is done by the largest kernel in Fourier domain. It should be noted that since the inverse convolution in Fourier domain is division, a threshold is needed to suppress division by zero. Another variant of SHARP is regularization enabled SHARP (RESHARP) which tries to obtain accurate result close to boundary by a regularization parameter (Sun H, 2014). SHARP suffers from lack of information at boundary of ROI. RESHARP leverages the fact that most of at boundary contribution is from air-tissue interface which is an order of magnitude greater of inter-tissue susceptibility difference. Thus, the magnitude of local field at the boundary should be minimized and problem is a constrained minimization problem:

$$argmin_{B_{local}} \left(\left|\left| \Delta B_S - \; M\, F^{-1}\{K\, F\{\Delta B_{local}\}\} \right|\right|_2^2 + \lambda \left|\left| \Delta B_{local} \right|\right|_2^2 \right) \tag{1.43}$$

The λ is regularization parameter. Concept of RESHARP is making a compromise between the first term (fidelity term) and the assumption of having minimal local field. First term used to satisfy SHARP condition and second term is an additional Tikhonov regularization.

Laplacian boundary value (LBV) is another background field removal method widely used in QSM (Dong Zhou, 2014). LBV takes the advantage of having a null Laplacian value for external field:

$$\nabla^2 B_{total} = \; \nabla^2 B_{local} + \; \nabla^2 B_{ext}$$

$$\nabla^2 B_{total} = \; \nabla^2 B_{local} \tag{1.44}$$

Equation (1.44) leads to a Poisson equation that needs boundary value information. Similar to RESHARP, LBV assumes the field shift at boundary is coming from external sources as a result the local field value is zero at the boundary:

$$\Delta B_{local}|_{\partial M} = 0 \tag{1.45}$$

Now the problem has a solution. But the assumption no field at boundary in some cases might be violated as the method is iterating.

Background field originating from external sources are orthogonal to the local field which has sources inside ROI (De Rochefort L L. T., 2010). Projection onto dipole field (PDF) is a method leveraging the fact (Duyn JH, 2007). PDF decomposes the field inside ROI into two orthogonal components and searches for an external susceptibility map distribution that can fit the orthogonal component inside:

$$\chi_{ext} = \ argmin_{\chi} \left\| MW \ (\Delta B_{total} - \ (1 - M) \ . \ F^{-1}\{D \ . \ F\{\chi\}\} \right\|_2^2 \tag{1.46}$$

D is the unit dipole kernel in Fourier domain and W is the weighting matrix and (1-M) is external mask. Equation (1.46) is looking for a susceptibility map outside ROI which yields similar field shift map inside ROI. When the method converges and the desired external susceptibility map is yielded, the local field shift map can be simply derived by subtracting background field from total field:

$$\Delta B_{local} = \ M\left(\Delta B_{total} - F^{-1}\{D \ . F\{\chi_{ext}\}\}\right) \tag{1.47}$$

Advantage of PDF is not having any boundary related assumption and condition. As a result, there is no artifacts at boundary which will propagate into ROI. The external distribution yielded from PDF may not exist in reality as it raises from the assumption that external sources must create such background map. However, PDF cannot remove the artifacts that are not originated from an external susceptibility source such as an imperfect coil shimming which results in inhomogeneous B_0 field.

The background field is an order of magnitude greater than the local field shift and varies slowly. In other words, the background field consists of low spatial frequency components therefore, it is prevalent to use a high pass filter to suppress the low frequency component of the total field (Haacke EM, 2009; AH Wilman, 2011). This helps the non-linear methods to also remove further background field but it also removes the low frequency component of local field.

In figure 1.7 different background removal methods has been applied to a subject and result can be compared. RESHARP and VSHARP both seemed to perform better further away from the edges

of the brain. However, due to the kernel size, RESHARP did not produce results at the brain edges (due to erosions) while VSHARP provided inaccurate local field values at the boundaries of the brain. PDF provided local field maps that appeared to have least artifact by visual inspection, though some residual background fields were still present at the brain edges which could not be removed by mask erosion (Karsa, 2018).

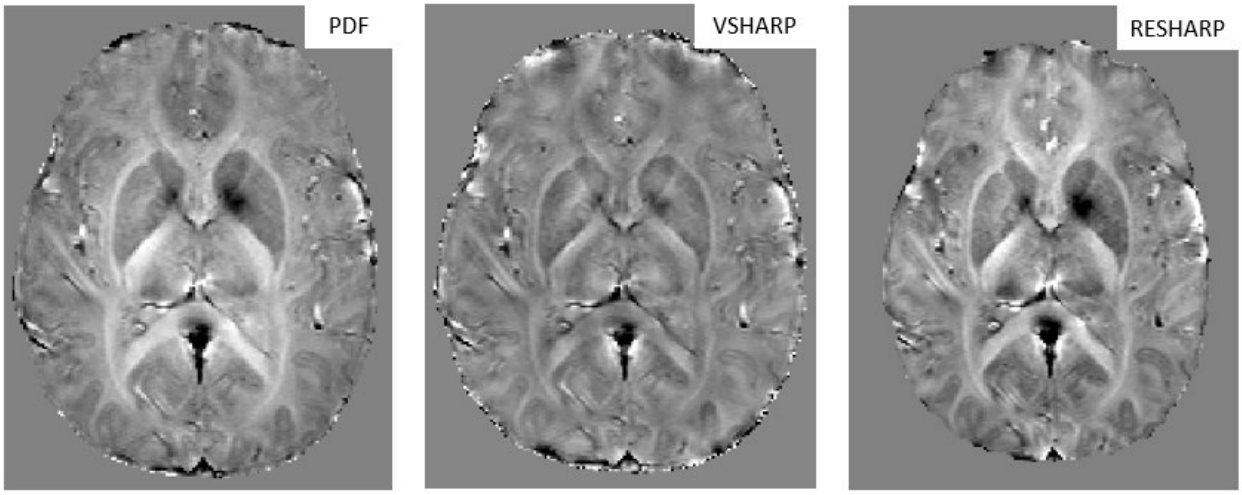

Figure 1.7: Different background removal methods has been applied to a subject.

1.5.3 Dipole Inversion

Previously the relation between susceptibility sources distribution and resulting field shift were discussed. Equation (1.27) exhibits the relation and equation (1.28) shows the effect of unit dipole on the surrounding magnetic field. For simplicity, the dipole effect kernel (equation (1.28)) is calculated in k-space:

$$D(\boldsymbol{K}) = \frac{1}{3} - \frac{K_z^2}{K_x^2+K_y^2+K_z^2} \tag{1.48}$$

The kernel has singularities at angle of 54.7° which is called magic angle where D(**K**) = 0. It makes the problem of finding susceptibility distribution given the field shift, an ill-posed problem. As a result, the local susceptibility distribution cannot be calculated directly ($\chi_{local} = F\{\Delta B_{local}\} / D(\boldsymbol{K})$). To solve the problem several methods have been proposed

1.5.3.1 Truncated K-space Division (TKD)

A simple approach to the problem can be using a threshold (t) to truncate the kernel and avoid dividing by zeros:

$$D_t(\boldsymbol{K}) = \begin{cases} D(\boldsymbol{K}) & |D(\boldsymbol{K})| > t \\ t & |D(\boldsymbol{K})| < t \end{cases} \tag{1.49}$$

The truncated kernel can be used to derive the susceptibility map:

$$\chi = \frac{\Delta B_{local}}{D_t(\boldsymbol{K})} \tag{1.50}$$

The method can avoid noise amplification made by regular dipole kernel but it underestimates the susceptibility values in some regions in addition, it comes with some striking artifacts (Schweser F D. A., 2013). Some methods have developed the idea of truncated kernel division.

1.5.3.2 Image Space Regularization Based Methods

The image space regularization based methods are a category of dipole inversion methods that all consists of two main components: (1) a fidelity term which ensures the consistency of the resulted susceptibility map with the local field shift map (2) a regularization term that tries to minimize effects of noise and incorporate additional information. There is a regularization coefficient that establishes a balance between the two terms. Therefore, the general minimization function for this category is:

$$argmin_{\chi} \left\| W \left(\Delta B_{local} - (d * \chi) \right) \right\|_2^2 + reg(\chi) \tag{1.51}$$

Morphology enabled dipole inversion (MEDI), Tikhonov regularization and total variation (TV) are the popular examples of this category which are explained below:

(i) Morphology Enabled Dipole Inversion (MEDI)

MEDI first developed by (Jing Liu, 2012). It introduces a new concept for regularization: the susceptibility map is related to the magnitude image in regions with high signal to noise ratio (SNR). As a result, in those regions susceptibility map should be smooth and not contain artifact:

$$argmin_{\chi} \left\| M\, W\, \left(\Delta B_{local} - (d * \chi)\right)\right\|_2^2 + \lambda \left\| M_G W_G\, \nabla \chi \right\|_1 \qquad (1.52)$$

M and W are binary mask and weight matrix respectively in ROI. M_G and W_G are binary mask and weight matrix for regions with small gradients in magnitude image, respectively. The regularization term is implicitly making the alignment between the susceptibility and magnitude map.

(ii) Tikhonov Regularization

Tikhonov regularization is another image space regularization base method that accounts for overfitting of susceptibility values (Ludovic de Rochefort, 2010). The susceptibility values are expected to be small in brain but just relying on fidelity term may result in large values. As a result, Tikhonov regularization introduces a L2 norm of susceptibility values which prevents the susceptibility map from having abnormal large values:

$$argmin_{\chi} \left\| M\, W\, \left(\Delta B_{local} - (d * \chi)\right)\right\|_2^2 + \alpha \left\| M\, .\, \chi \right\|_2^2 \qquad (1.53)$$

Equations (1.53) can be implemented using conjugate gradient method which converge to a solution by iteration.

(iii) Total Variation Regularization (TV)

Total variation (TV) is a generalized version of MEDI as it assumes the susceptibility map is piece-wise constant everywhere in ROI (Bilgic B, 2012). Whereas MEDI has the same assumption but in regions with low magnitude changes (gradient):

$$argmin_{\chi} \left\| M\, W\, \left(\Delta B_{local} - (d * \chi)\right)\right\|_2^2 + \lambda \left\| \nabla \chi \right\|_1 \qquad (1.54)$$

The gradient regularization makes TV to generate a piece-wise uniform map which is easy to understand. An issue for the method is that even an ROI is unlikely to have uniform distribution across. Therefore, the result might not be very realistic.

All in all, image space regularization methods are better options in terms of visualization and they have less variability than TKD methods. But TKD can be easily implemented and is faster than regularization methods. Figure 1.8 is a comparison of a TKD and an image space regularization method, TV. There are less noise is associated with TV and more variations with TKD. In addition, some striking artifacts exist in TKD processed map which are mitigated or fully eliminated in corresponding TV maps (Sun, 2015).

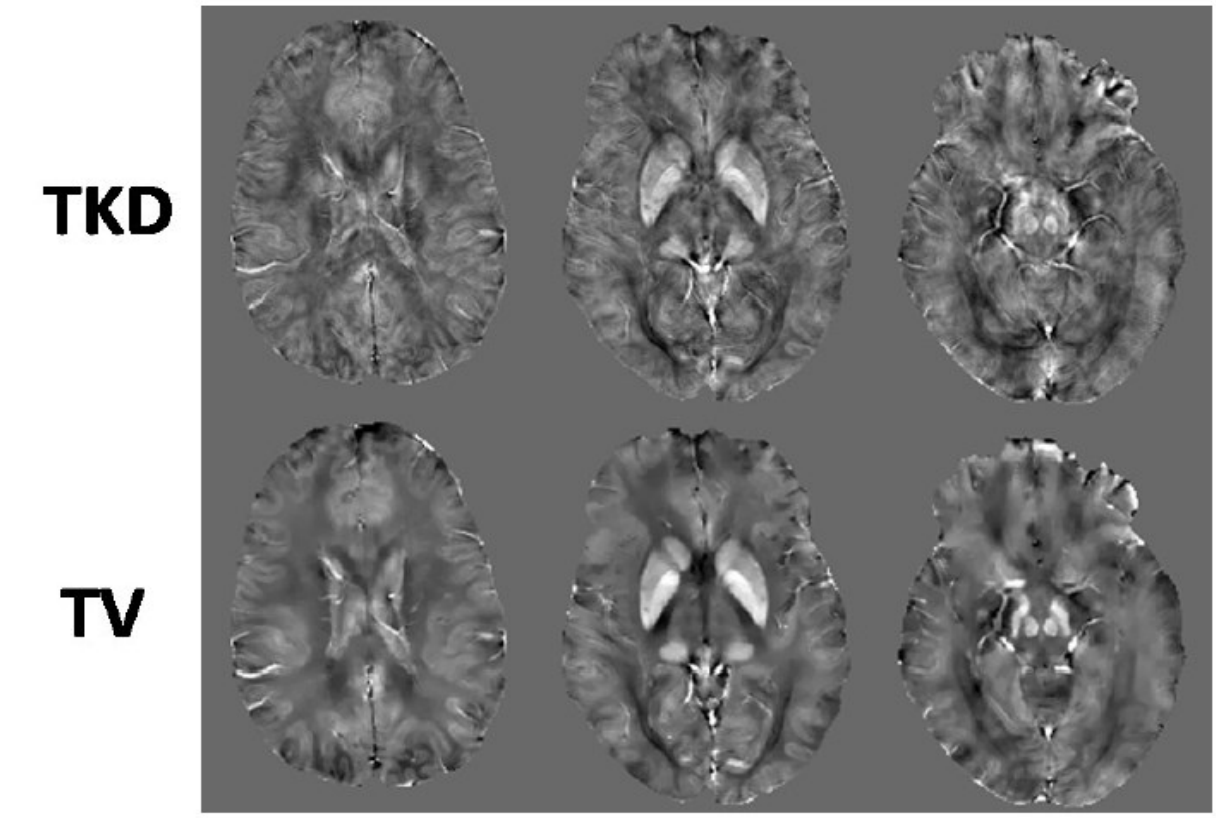

Figure 1.8: Different susceptibility inversion methods applied on local field shift map. Top row is multiple axial slices undergone TKD method. The bottom row is the same corresponding axial slices but were result of TV.

Overall figure 1.9 shows the pipeline for QSM; the phase image is unwrapped then using the mask extracted from magnitude image, background field is removed. At the end, the susceptibility map will be derived from local field shift by solving the inverse problem, equation (1.51), (Woojin Jung, 2020).

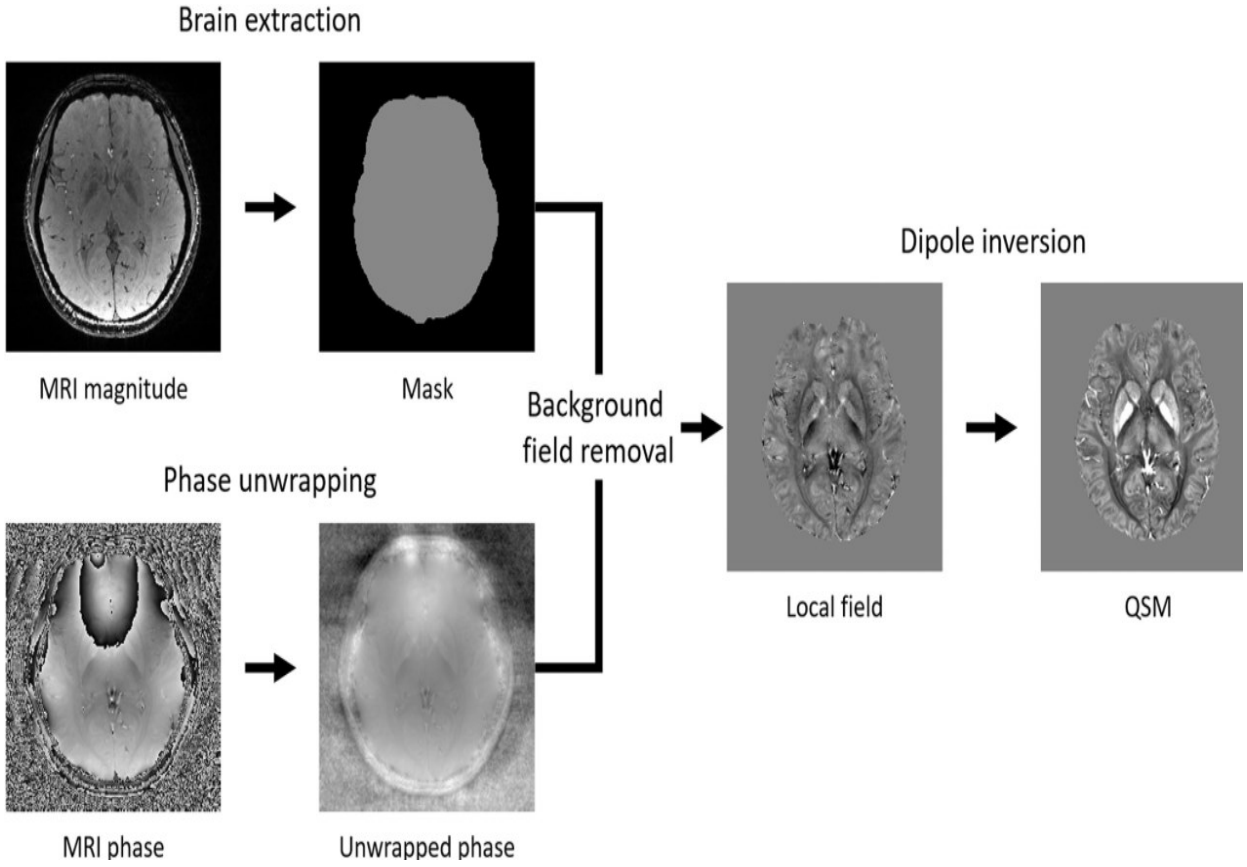

Figure 1.9: QSM general pipeline: the phase map is unwrapped and a mask is derived from magnitude image in parallel. Then background field is removed and final susceptibility map is obtained.

1.6 Quantitative R2' Measurement

The MR signal acquired at each echo time consists of a magnitude and a phase component. For R2 and R2* measurement, the focus is on the magnitude component (M). Magnitude during signal acquisition experiences different relaxation processes which are called spin-spin and spin-lattice relaxation. The first is known as R2 and the second is known as R1 relaxation. The transverse signal's magnitude is affected by R2 and some dephasing factors with relaxation rate of R2':

$$R2^{*} = R2' + R2 \tag{1.55}$$

Where R_2 and R_2' are the irreversible and reversible components of R_2^*. An R_2^* image is acquired using a MEGE sequence in order to capture all the factors dephasing the spins. To produce an R_2^* map, air-tissue background fields may be corrected first (Fernandez, 2000; Du YP, 2009) followed

by mono-exponential fitting to the magnitude image with respect to echo times (Pei, 2015). R_2^* can be affected by diffusion and anisotropic sources including myelin fibers, and may be multi-component in white matter (Dyun, 2017; S. Wharton, 2012; Sati P, 2013).

Example brain images of all three transverse relaxation rates will be shown in the next section. The magnitude component decay depends on these two relaxation rates as shown in figure 1.10. R_2 is an intrinsic feature of a tissue while R_2^* depends on additional environmental factors such as magnetic field inhomogeneity, imperfect shimming, air-tissue interfaces, susceptibility values, etc.

R_2 is also called the transverse relaxation rate and is the result of random interactions at the atomic and molecular levels. Transverse relaxation is primarily related to the intrinsic field caused by adjacent protons (spins) and hence is called spin-spin relaxation. Transverse relaxation causes irreversible dephasing of the transverse magnetization because the processes are dynamic and irreversible. Note the additional dephasing in R_2^*, arising from R_2' can be eliminated by using a 180° refocusing pulse, as in a spin-echo sequence. Hence, in a spin-echo sequence, only the "true" T_2 relaxation is seen, ideally (Chavhan, 2009). However, the R_2 measurement in-vivo comes with many difficulties including coping with relatively long inter-echo spacings of many ms (e.g. 10 ms) that give rise to an apparent R_2 that is affected by diffusion. Other difficulties are the problem of inaccurate refocusing pulses due to both B1+ field inhomogeneities and slice profile effects (J.T. Vaughan, 2001; David L. Thomas, 2005; Haiying Liu, 2002; Ke Li, 2014; Khader M. Hasan, 2009). Typically, R_2 is measured in-vivo with a multiple echo spin echo (MESE) sequence. Additional difficulties include the long acquisition time for MESE sequences. Alternatives for speeding up R_2 acquisitions include the sharing of echoes, by using multiple echo times towards each image or using methods such as compress sensing and machine learning to help reconstructing the image (Liu F, 2021; Lustig M, 2007; McPhee KC, 2017; Snyder J, 2021).

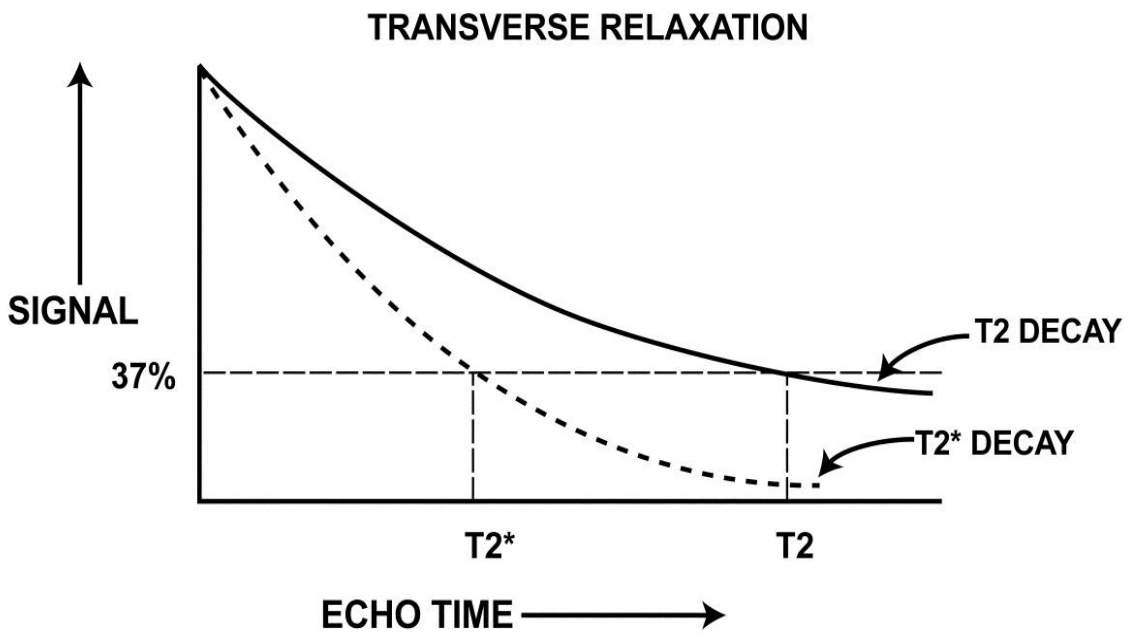

Figure 1.10: T2 and T2* Decay rates of magnitude component

After subtracting R_2 from R_2^*, R_2' is yielded. R_2' is referred to as the reversible part of dephasing and can be related directly to field inhomogeneity:

$$R_2' = \gamma \Delta B_{inhom} \tag{1.56}$$

ΔB_{inhom} is the magnetic field inhomogeneity across a voxel. Some studies have shown that R_2' strongly correlates to brain iron concentrations in normal volunteers, and has higher iron-related specificity and smaller iron-independent component (Qin, 2011) (Ordidge RJ G. J., 1994) (Gelman N, 1999) (Brass SD, 2006) . For this reason, R_2' is used to quantify iron levels in patients with Parkinson and Alzheimer Disease (AD) (Qin, 2011). The reason that R_2 and R_2^* are not as ideal for the purpose of iron quantification is they contain iron independent components as well. R_2^* suffers from coexisting water content which can lead to increased R_2^* values (Yan F, 2018). R_2^* images are more sensitive to microscopic inhomogeneities of the magnetic field reflecting iron deposition than R_2 images (Lehéricy S, 2020). R_2 also suffers from the effects of water content changes and iron changes which may be difficult to distinguish (Chen Y, 2018). Therefore, all the transverse relaxation methods do not reflect just iron content effects. In functional MRI (fMRI), separate measurement of R_2 and R_2' has been recognized as an approach to distinguish BOLD

responses in parenchyma from responses in large draining veins (Yablonskiy DA H. E., 1994). Also, the blood R_2 values can be useful to measure tissue oxygen extraction fractions while the changes in R_2' are approximately linearly related to the changes in blood oxygenation level (Ogawa S, 1993)

1.7 Susceptibility Separation Techniques

In recent years, the novel idea of separating susceptibility sources into paramagnetic and diamagnetic parts has flourished. Conventional QSM methods were not capable of separating susceptibility sources in each voxel because they yield only a net map. Separation methods can show the extent of paramagnetic and diamagnetic sources voxel-wise (Emmerich J 2021; Shin HG 2021). Figure 1.11 shows how conventional QSM and novel separation methods deal with a mix of sources in the voxel.

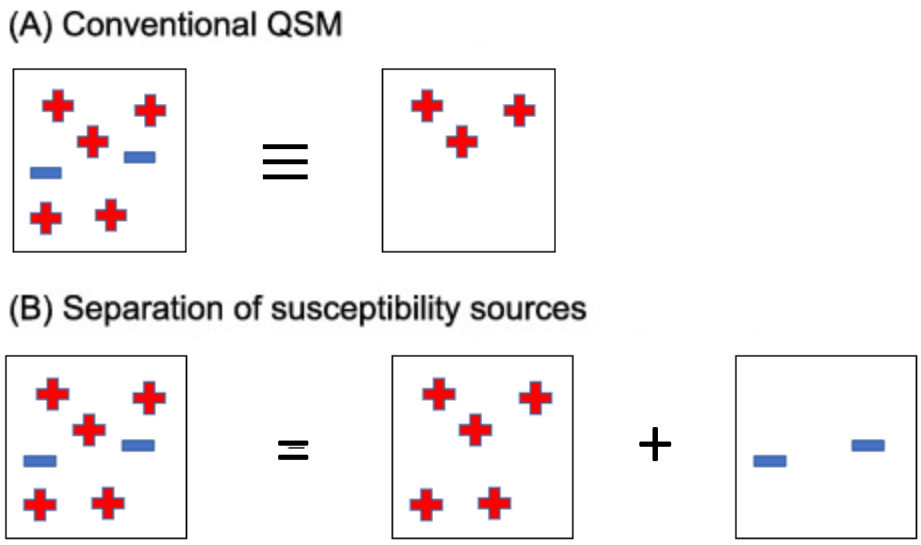

Figure 1.11: (A) The conventional QSM methods only reconstructs the net amount of susceptibility existing in a voxel. (B) Separation methods can distinguish the underlying paramagnetic and diamagnetic susceptibility sources in a voxel

This separation ability becomes critical when we are not sure about the underlying cause of a change in the voxel net susceptibility. For instance, an increase in net susceptibility could be made by either iron deposition or demyelination. Separation methods can determine the cause by

independently showing an increase in paramagnetic component (iron deposition) or a decrease in diamagnetic component (demyelination).

Among the separation methods, utilizing information in R_2' map is common. Usually it is assumed that R_2' map is perfectly made by susceptibility sources. Then the R_2' map will be directly related to susceptibility components in a voxel by a coefficient. Paramagnetic and diamagnetic sources coexisting in a voxel that are spherical add linearly to the relaxation if conditions of the static dephasing regime are not violated (Julian Emmerich P. B., 2020).

Julian Emmerich assumes the extra information needed to separate susceptibility sources can be extracted from an R_2^* map (Julian Emmerich P. B., 2021):

$$R^*_{2,tot} = \frac{1}{T_{2,0}} + \frac{1}{T^*_{2,ext}} + \Delta R^*_2 \tag{1.57}$$

In this model, the different contributions are considered to be mono exponential themselves. $T_{2,0}$ is the intrinsic transverse relaxation time of the sample without the influence of any voxel substructure. Effects by unknown sample substructure that are not covered by the used model of spherical perturbers and external field inhomogeneities are included in the term $T^*_{2,ext}$ (Lukas R. Buschle, 2015). The influence of randomly distributed spherical objects on the relaxation rate is described by the term ΔR^*_2 (Julian Emmerich P. B., 2021). The expressions describing the relaxation effects are linear in the susceptibility term:

$$\Delta R^*_2 = \frac{2\pi}{9\sqrt{3}} \gamma . \eta . \chi . B_0 \tag{1.58}$$

γ is the gyromagnetic ratio and η is the volume fraction. It was experimentally shown that in the presence of two coexisting susceptibility sources in the static dephasing regime (SDR) (Julian Emmerich P. B., 2020), the overall change in relaxation rate ΔR^*_2 can be written as:

$$\Delta R^*_2 = \frac{2\pi}{9\sqrt{3}} \gamma \left(\eta_{neg} \left| \chi_{neg} \right| + \eta_{pos} \left| \chi_{pos} \right|\right) B_0 \tag{1.59}$$

Where η_{neg} and η_{pos} are diamagnetic and paramagnetic sources fraction respectively. χ_{neg} and χ_{pos} are the diamagnetic and paramagnetic susceptibility sources respectively. As a consequence, the relaxation rate ΔR^*_2 is linear in both susceptibility arguments in the static dephasing regime and

relaxation effects add up linearly in an experimental setting if particles with different susceptibilities are present within the same volume. This holds only true for small volume fractions and in the absence of diffusion effects. Furthermore, it is assumed, that the size of the susceptibility sources is small compared to the length scale provided by the voxel size. This assumption causes, that blooming effects in relaxation rate mapping can be neglected.

Another method so-called χ separation (Shin HG 2021) assumes the R_2' relaxation originates primarily from magnetic susceptibility sources when ignoring chemical exchange and chemical shift effects. In the static dephasing regime, which postulates low diffusivity and low susceptibility source concentration, the decay of a voxel signal can be modeled as follows (Yablonskiy DA H. E., 1994):

$$R_2' = D_r \left(|\chi_{pos}| + |\chi_{neg}| \right) \tag{1.60}$$

Where D_r is a relaxometric constant between R_2' and susceptibility. This equation suggests that R_2' is linearly proportional to the concentration of susceptibility sources regardless of the sign of them. The relaxometric constant can be estimated by the ratio of R_2' to absolute susceptibility. Figure 1.12 provides an intuitive depiction of how paramagnetic and diamagnetic sources contribute to the R_2' relaxation.

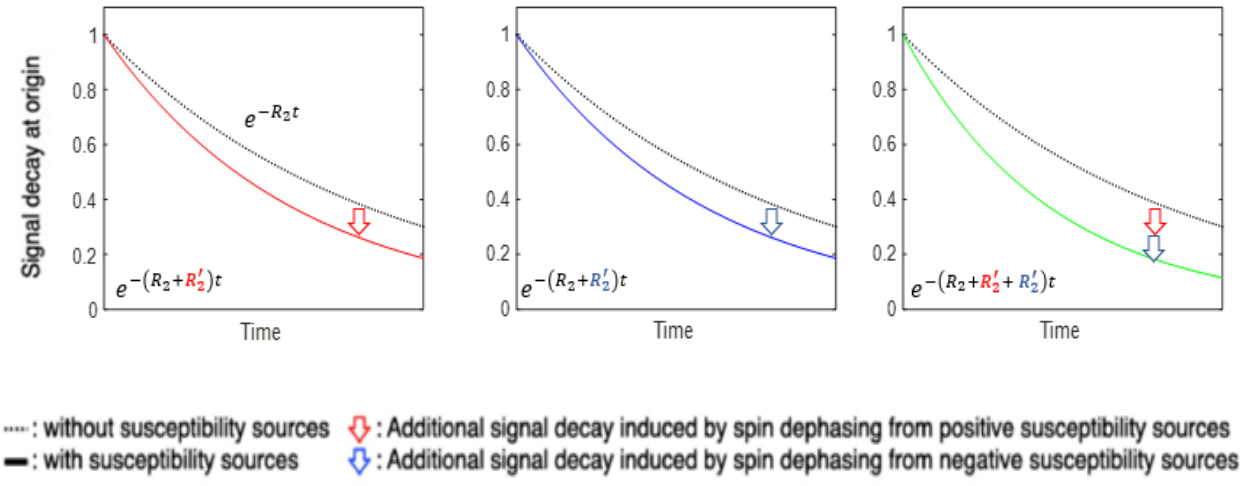

Figure 1.12: Effects of paramagnetic and diamagnetic susceptibility sources on relaxation decay. Both components contribute equally to the decay rate

Equation (1.60) can be extended to account for negative and positive values, separately:

$$R_2' = \left(D_{r,pos} \left|\chi_{pos}\right| + D_{r,neg} \left|\chi_{neg}\right| \right) \quad (1.61)$$

$D_{r,pos}$ and $D_{r,neg}$ are the relaxometric coefficient for paramagnetic and diamagnetic components, respectively. Note that this model assumes susceptibility is the primary source for frequency shift and R_2', while ignoring susceptibility anisotropy effects (J. Lee, 2010) or water compartmentalization (S. Wharton, 2015, 2012). By this definition of susceptibility sources, the equation for susceptibility sources magnetic field in a voxel can be rewritten:

$$\Delta B_{local} = D_f * \left(\chi_{pos} + \chi_{neg}\right) \quad (1.62)$$

Combining equations (1.61) and (1.62) yields a loss function to be minimized:

$$argmin_{\chi_{pos},\chi_{neg}} \left\| \Delta B_{local} - D_f * \left(\chi_{pos} + \chi_{neg}\right) + i2\pi \left(R_2' - \left(D_{r,pos} \left|\chi_{pos}\right| + D_{r,neg} \left|\chi_{neg}\right| \right) \right) \right\|_2^2 \quad (1.63)$$

Equation (1.63) is solved iteratively using a conjugate gradient descent algorithm. The method needs an initial map to develop. Such map can be obtained as follow:

$$\begin{cases} \chi_{conventional} = \left|\chi_{pos}\right| - \left|\chi_{neg}\right| \\ R_2' = \left(D_{r,pos} \left|\chi_{pos}\right| + D_{r,neg} \left|\chi_{neg}\right| \right) \end{cases} \quad (1.64)$$

$\chi_{conventional}$ is the susceptibility map obtained by conventional QSM pipeline. Equation (1.64) is subjected to restraints for positive and negative susceptibility sources as $\chi_{pos} \geq 0$ and $\chi_{neg} \leq 0$. The conjugate gradient solver builds on the initial map in every iteration.

Figure 1.13 is an example of the method established by (Shin HG 2021). The changes between conventional QSM and total susceptibility derived from separation method is subtle. The paramagnetic and diamagnetic maps are consistent. For better visualization different relaxation maps (R_2, R_2', R_2^*) are depicted as well.

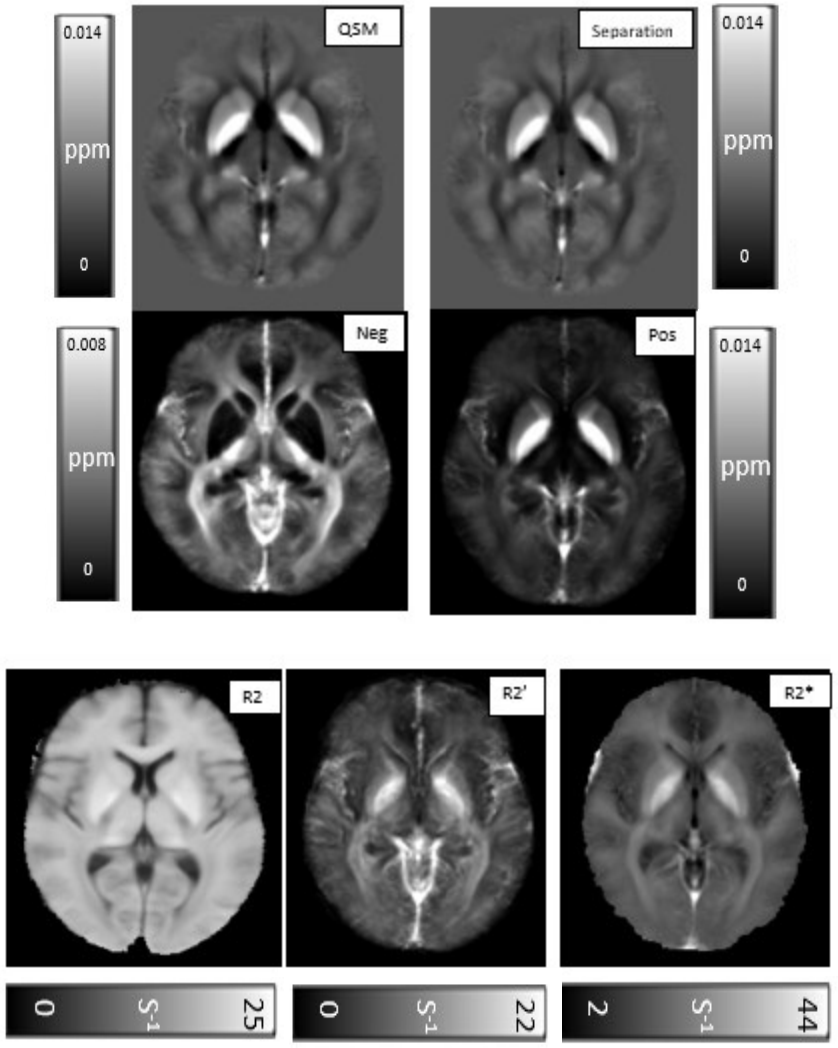

Figure 1.13: Resulting susceptibility maps of the Shin susceptibility separation method as well as relaxation maps.

1.8 Motivation for the Thesis

MRI is widely used but the signal is dependent on many factors. An area of intense focus is to make MRI both more quantitative and more specific to tissue properties. Quantitative measures might include volume measures or relaxation times T2 and T1. However, these measures generally lack specificity to only a particular tissue change (Stanisz GJ, 2005; Helen M, 2013; Ziemssen T, 2016). For example, in multiple sclerosis a long T2 time might indicate demyelination, inflammation or iron loss, amongst other possibilities (Lehéricy S, 2020). Recent methods such as QSM have provided a route to access more fundamental tissue properties (Elkady AM, 2018; Schweser F, 2021). However, in brain, the susceptibility is highly affected by diamagnetic myelin and paramagnetic iron (Schweser F, 2021 ;Liu C, 2015). In 2021, very promising methods to further specify the susceptibility source by performing susceptibility separation have been introduced, but these methods have not been tested for reliability, nor examined in detail. For any measure to be practical in clinical studies it must be reliable (Emmerich J 2021; Shin HG 2021). Thus, the focus of this thesis is examining parameter choices in susceptibility separation and testing its reliability in brain using healthy volunteers. If these methods can be proven reliable, they would open the door to quantifying myelin and iron changes in the brain that would be valuable for following many neurodegenerative diseases, including multiple sclerosis.

References

Abdul-Rahman HS, Gdeisat MA, Burton DR, Lalor MJ, Lilley F, Moore CJ. 2007. "Fast and robust three-dimensional best path phase unwrapping algorithm." *Appl Opt* 46: 6623-6635.

AG, Redfield. 1955. "Nuclear magnetic resonance saturation and rotary saturation in solids." *Phys Rev* 1787-1809.

AH, Walsh AJ & Wilman. 2011. "Susceptibility phase imaging with comparison to R2 mapping of iron-rich deep grey matter." *Neuroimage* 57: 452-461.

Arrighini, G. P., and M. Maestro & R. Moccia. 1968. "Magnetic Properties of Polyatomic Molecules: Magnetic Susceptibility of H2O, NH3, CH4, H2O2." *J. Chem. Phys* 49 (2): 882–889.

Bernstein MA, King KE, Zhou XJ, Fong W. 2005. *Handbook of MRI Pulse Sequences.* Med. Phys.

Bezanson J, Karpinski S, Shah VB, Julia EA. 2012. "A fast dynamic language for technical computing." *ArXiv.*

BingWu, Wei Li, Arnaud Guidon, and Chunlei Liu. 2012. "Whole brain susceptibility mapping." *Magnetic Resonance in Medicine* 137-147.

Biondetti, Emma. 2016. "Optimising MRI susceptibility mapping to image brain arteriovenous malformations." PhD Thesis.

Bioucas-Dias JM, Valadao G. 2007. "Phase unwrapping via graph cuts." *IEEE Trans Image Process* 16: 698-709.

Bloch, F. 1946. "Nuclear Induction." *American Physical Society.*

Brass SD, Chen T, Mulkern RV, et al. 2006. "Magnetic resonance imaging of iron deposition in neurological disorders." *Top Magn Reson Imaging* 31-40.

Chavhan, G. B., Babyn, P. S., Thomas, B., Shroff, M. M., & Haacke, E. M. 2009. "Principles, techniques, and applications of T2*-based MR imaging and its special applications." *Radiographics* 1433-1449.

Chen Y, Liu S, Wang Y, Kang Y, Haacke EM. 2018. "STrategically Acquired Gradient Echo (STAGE) imaging, part I: creating enhanced T1 contrast and standardized susceptibility weighted imaging and quantitative susceptibility mapping." *Magn Reson Imaging* 46: 130–139.

CP, Slichter. 1990. *Chapter 6 -Electric quadrupole effects BT - Principles of Magnetic Resonance. In: Principles of Magnetic Resonance.*

David L. Thomas, Enrico De Vita, Ralf Deichmann, Robert Turner, and Roger J. Ordidge. 2005. "3d MDEFT imaging of the human brain at 4.7 T with reduced sensitivity to radiofrequency inhomogeneity." *Magnetic resonance in medicine* 53(6): 1452-1458.

De Rochefort L, Brown R, Prince MR, Wang Y. 2008. "Quantitative MR susceptibility mapping using piece-wise constant regularized inversion of the magnetic field." *Magn. Reson. Med* 60: 1003–9.

De Rochefort L, Liu T, Kressler B, Liu J, Spincemaille P, Lebon V, Wu J, Wang Y. 2010. "Quantitative susceptibility map reconstruction from MR phase data using bayesian regularization: validation and application to brain imaging." *Magn. Reson. Med* 194-206.

Deshmane, A., Gulani, V., Griswold, M. A., & Seiberlich, N. 2012. "Parallel MR imaging. Journal of magnetic resonance imaging." *JMRI* 36(1): 55–72. doi:https://doi.org/10.1002/jmri.23639.

Donald W McRobbie, Elizabeth A Moore, and Martin J Graves. 2017. *MRI from Picture to Proton.* Cambridge University Press.

Dong Zhou, Tian Liu, Pascal Spincemaille, and Yi Wang. 2014. "Background field removal by solving the Laplacian boundary value problem." *NMR in Biomedicine* 27(3): 312-319.

Du YP, Jin Z, Hu Y, Tanabe J. 2009. "Multi-echo acquisition of MR angiography and venography of the brain at 3 Tesla." *J Magn Reson Imaging* 30: 449–454.

Duyn JH, van Gelderen P, Li T-Q, de Zwart J a, Koretsky AP, Fukunaga M. 2007. "High-field MRI of brain cortical substructure based on signal phase." *Proc. Natl. Acad. Sci. U. S. A.* 11796–801.

Dymerska, B., Eckstein, K., Bachrata, B., Siow, B., Trattnig, S., Shmueli, K., & Robinson, S. D. 2021. "Phase unwrapping with a rapid opensource minimum spanning tree algorithm (ROMEO)." *Magnetic resonance in medicine* 2294–2308.

Edelkamp S, Schroedl S. 2011. *Bucket data structures In: Heuristic Search: Theory and Applications.* Burlington, Massachusetts: Morgan Kaufmann Publishers.

Elkady AM, Cobzas D, Sun H, Blevins G, Wilman AH. 2018. "Discriminative analysis of regional evolution of iron and myelin/calcium in deep gray matter of multiple sclerosis and healthy subjects." *J Magn Reson Imaging.*

Emmerich J, Peter Bachert, Mark E. Ladd, Sina Straub. 2021. "On the separation of susceptibility sources in quantitative susceptibility mapping: Theory and phantom validation with an in vivo application to multiple sclerosis lesions of different age." *Journal of Magnetic Resonance.*

Emmerich J, Peter Bachert, Mark E. Ladd, Sina Straub. 2020. "On the influence of two coexisting species of susceptibility-producing structures on the R2∗ relaxation rate." *Magnetic Resonance Imaging* 170-177.

F, Fernández-Seara M & Wehrli. 2000. "Postprocessing technique to correct for background gradients in image-based R* 2 measurements." *Magnetic resonance in medicine* 44: 358-366.

Gelman N, Gorell JM, Barker PB, et al. 1999. "MR imaging of human brain at 3.0 T: preliminary report on transverse relaxation rates and relation to estimated iron content." *Radiology* 759-767.

Gilbert G, Savard G, Bard C, Beaudoin G. 2012. "Quantitative comparison between a multiecho sequence and a single-echo sequence for susceptibility-weighted phase imaging." *Magn. Reson. Imaging* 722-730.

Goodrich MT, Tamassia R, Goldwasser MH. 2014. *Data Structures and Algorithms in Java.* Hoboken, New Jersey: John Wiley & Sons.

Griswold MA, Jakob PM, Heidemann RM, et al. 2002. "Generalized autocalibrating partially parallel acquisitions (GRAPPA)." *Magn Reson Med* 47: 1202–1210.

Haiying Liu, Edward Michel, Sean O. Casey, and Charles L. Truwit. 2002. "Actual imaging slice profile of 2d MRI." *Physics of Medical Imaging* 4682: 767–773.

HM, Branson. 2013. "Normal myelination: a practical pictorial review." *Neuroimaging Clin N Am* 23(2): 183-95.

Hsieh M-C, Tsai C-Y, Liao M-C, Yang J-L, Su C-H, Chen J-H. 2016. "Quantitative susceptibility mapping-based microscopy of magnetic resonance venography (QSM-mMRV) for in vivo morphologically and functionally assessing cerebromicrovasculature in rat stroke model." *PLoS One.*

J. Lee, K. Shmueli, M. Fukunaga, P. Gelderen, H. van, Merkle, A.C. Silva, J.H. Duyn. 2010. "Sensitivity of MRI resonance frequency to the orientation of brain tissue microstructure." *Proc. Natl. Acad. Sci* 5130-5135.

J., Duyn JH & Schenck. 2017. "Contributions to magnetic susceptibility of brain tissue." *NMR Biomed* 30.

J.T. Vaughan, M. Garwood, C.m. Collins, W. Liu, L. DelaBarre, G. Adriany, P. Andersen, H. Merkle, R. Goebel, M.b. Smith, and K. Ugurbil. 2001. "7t vs. 4t: RF power, homogeneity, and signal-to-noise comparison in head images." *Magnetic Resonance in Medicine* 46(1): 24-30.

Jing Liu, Tian Liu, Ludovic de Rochefort, James Ledoux, Ildar Khalidov, Weiwei Chen, A. John Tsiouris, Cynthia Wisnie, and Yi Wang. 2012. "Morphology enabled dipole inversion for quantitative susceptibility mapping using structural consistency between the magnitude image and the susceptibility map." *NeuroImage* 2560-2568.

Karsa, Anita. 2018. "Optimising MRI Magnetic Susceptibility Mapping for Applications in Challenging Regions of the Body." PhD Thesis.

Ke Li, Richard D. Dortch, E. Brian Welch, Nathan D. Bryant, Amanda K.W. Buck et.al. 2014. "Multi-parametric MRI characterization of healthy human thigh muscles at 3.0T relaxation, magnetization transfer, fatwater, and diffusion tensor imaging." *NMR in biomedicine* 27(9): 1070–1084.

Khader M. Hasan, Christopher Halphen, Arash Kamali, Flavia M. Nelson, Jerry S.Wolinsky, and Ponnada A. Narayana. 2009. "Caudate Nuclei Volume, Diffusion Tensor Metrics, and T2 Relaxation in Healthy Adults and Relapsing-Remitting Multiple Sclerosis Patients: Implications to Understanding Gray Matter Degeneration." *Journal of magnetic resonance imaging* 29(1): 70–77.

Khan, Ahmad Raza. 2013. "RADIATION INDUCED MORPHOLOGICAL AND BIOCHEMICAL CHANGES IN MOUSE MODEL USING NMR IMAGING AND SPECTROSCOPY."

L, Li. 2001. "Magnetic susceptibility quantification for arbitrarily shaped objects in inhomogeneous fields." *Magn. Reson. Med* 46: 907–16.

Lehéricy S, Roze E, Goizet C, Mochel F. 2020. "MRI of neurodegeneration with brain iron accumulation." *Curr Opin Neurol* 33(4): 462-473.

Li W, Avram A V., Wu B, Xiao X, Liu C. 2014. "Integrated Laplacian-based phase unwrapping and background phase removal for quantitative susceptibility mapping." *NMR Biomed* 219-227.

Li W, Wu B, Liu C. 2011. " Quantitative susceptibility mapping of human brain reflects spatial variation in tissue composition." *Neuroimage* 1645-1656.

Liang Z-P, Lauterbur PC. 2000. *Principles of Magnetic Resonance Imaging: A Signal Processing Perspective.* IEEE Press.

Liu C, Li W, Tong KA, Yeom KW, Kuzminski S. 2015. "Susceptibility-weighted imaging and quantitative susceptibility mapping in the brain." *J Magn Reson Imaging* 42(1): 23-41.

Liu F, Kijowski R, El Fakhri G, Feng L. 2021. "Magnetic resonance parameter mapping using model-guided self-supervised deep learning." *Magn Reson Med.* 85(6): 3211-3226.

Liu J, Liu T, de Rochefort L, et al. 2012. "Morphology enabled dipole inversion for quantitative susceptibility mapping using structural consistency between the magnitude image and the susceptibility map." *Neuroimage* 59: 2560-2568.

Liu S, Buch S, Haacke EM. 2013. "Background field removal based on local complex phase unwrapping and spherical mean value property." *21st Annual Meeting of ISMRM* . Salt Lake City, Utah. 2496.

Ludovic de Rochefort, Tian Liu, Bryan Kressler, Jing Liu, Pascal Spincemaille, Vincent Lebon, Jianlin Wu, and Yi Wang. 2010. "Quantitative susceptibility map reconstruction from MR phase data using bayesian regularization: Validation and application to brain imaging." *Magnetic Resonance in Medicine* 194-206.

Lukas R. Buschle, Felix T. Kurz, Thomas Kampf, Simon M.F. Triphan, Heinz-Peter Schlemmer, Christian Herbert Ziener. 2015. "Diffusion-mediated dephasing in the dipole field around a single spherical magnetic object,." *Magnetic Resonance Imaging* 1126-1145.

Lustig M, Donoho D, Pauly JM. 2007. "Sparse MRI: The application of compressed sensing for rapid MR imaging." *Magn. Reson. Med* 58: 1182–95.

M, Jenkinson. 2003. "Fast, automated, N-dimensional phase-unwrapping algorithm." *Magn Reson Med* 49: 193-197.

Mansfield P, Grannell PK. 2001. "NMR “diffraction” in solids?" *J. Phys. C Solid State Phys* 422-426.

Marques JP, Bowtell RW. 2005. "Application of a Fourier-based method for rapid calculation of field inhomogeneity due to spatial variation of magnetic susceptibility." *Concepts Magn. Reson. Part B Magn. Reson. Eng.* 25B: 65–78.

McPhee KC, Wilman AH. 2017. "Transverse relaxation and flip angle mapping: Evaluation of simultaneous and independent methods using multiple spin echoes." *Magn Reson Med* 2057-2065.

Ogawa S, Menon RS, Tank DW, Kim SG, Merkle H, Ellermann JM, Ugurbil K. 1993. "Functional brain mapping by blood oxygenation level-dependent contrast magnetic resonance imaging. A comparison of signal characteristics with a biophysical model." *Biophys J* 803-812.

Ordidge RJ, Gorell JM, Deniau JC, et al. 1994. "Assessment of relative brain iron concentrations using T2-weighted and T2*-weighted MRI at 3 Tesla." *Magn Reson Med* 335-341.

Paschal CB, Morris CB. 2004. "K-space in the clinic." *J Magn Reson Imaging* 19: 145–159.

PC, LAUTERBUR. 1973. "Image Formation by Induced Local Interactions: Examples Employing Nuclear Magnetic Resonance." *Nature* 190-191.

Pei, M., Nguyen, T.D., Thimmappa, N.D., Salustri, C., Dong, F., Cooper, M.A., Li, J., Prince, M.R., Wang, Y. 2015. "Algorithm for fast monoexponential fitting based on Auto-Regression on Linear Operations (ARLO) of data." *Magn Reson Med* 843-850.

Pruessmann KP, Weiger M, Scheidegger MB, Boesiger P. 1999. "SENSE: sensitivity encoding for fast MRI." *Magn Reson Med* 42: 952–962.

Qin, Y., Zhu, W., Zhan, C. et al. 2011. "Investigation on positive correlation of increased brain iron deposition with cognitive impairment in Alzheimer disease by using quantitative MR R2′ mapping." *Med. Sci.*

Rabi II, Ramsey NF, Schwinger J. 1954. " Use of rotating coordinates in magnetic resonance problems." *Rev Mod Phys* 167-171.

Robert W. Brown, Yu-Chung N. Cheng, E. Mark Haacke, Michael R. Thompson, Ramesh Venkatesan. 2014. *Magnetic Resonance Imaging: Physical Principles and Sequence Design.* John Wiley & Sons, Inc.

Robinson SD, Bredies K, Khabipova D, Dymerska B, Marques JP, Schweser F. 2017. "An illustrated comparison of processing methods for MR phase imaging and QSM: Combining array coil signals and phase unwrapping." *NMR Biomed.*

RR, Ernst. 2011. "NMR fourier zeugmatography." *J. Magn. Reson* 510–512.

S. Wharton, R. Bowtell. 2015. "Effects of white matter microstructure on phase and susceptibility maps." *Magn. Reson. Med* 1258-1269.

S. Wharton, R. Bowtell. 2012. "Fiber orientation-dependent white matter contrast in gradient echo MRI." *Proceedings of the National Academy of Sciences* 18559-18564.

Salomir R, de Senneville BD, Moonen CT. 2003. "A fast calculation method for magnetic field inhomogeneity due to an arbitrary distribution of bulk susceptibility." *Concepts Magn. Reson* 19B: 26–34.

Sati P, van Gelderen P, Silva AC, et al. 2013. "Micro-compartment specific T2* relaxation in the brain." *Neuroimage* 77: 268-278.

Schweser F, Deistung A, Sommer K, Reichenbach JR. 2013. "Toward online reconstruction of quantitative susceptibility maps: Superfast dipole inversion." *Magn. Reson. Med* 1582-1594.

Schweser F, Hagemeier J, Dwyer MG, Bergsland N, Hametner S, Weinstock-Guttman B, Zivadinov R. 2021. "Decreasing brain iron in multiple sclerosis: The difference between concentration and content in iron MRI." *Hum Brain Mapp* 42(5): 1463-1474.

Shin HG, Lee J, Yun YH, Yoo SH, Jang J, Oh SH, Nam Y, Jung S, Kim S, Fukunaga M, Kim W, Choi HJ, Lee J. 2021. "χ-separation: Magnetic susceptibility source separation toward iron and myelin mapping in the brain." *Neuroimage.*

Snyder J, McPhee KC, Wilman AH. 2021. "T2 quantification in brain using 3D fast spin-echo imaging with long echo trains." *Magn Reson Med.*

SS, Hidalgo-Tabon. 2001. " Theory of gradient coil design methods for magnetic resonance imaging." *Concepts Mag Res Part A* 223-242.

Stanisz GJ, Odrobina EE, Pun J, Escaravage M, Graham SJ, Bronskill MJ, Henkelman RM. 2005. "T1, T2 relaxation and magnetization transfer in tissue at 3T." *Magn Reson Med* 54(3): 507-12.

Sun, Hongfu. 2015. "Quantitative Susceptibility Mapping in Human Brain: Methods Development and Applications." PhD Thesis.

TW, Redpath. 1988. "Principles of nuclear magnetic resonance in one and two dimensions." *Magn. Reson. Imaging.*

Vinayagamani S, Sheelakumari R, Sabarish S, Senthilvelan S, Ros R, Thomas B, Kesavadas C. 2021. "Quantitative Susceptibility Mapping: Technical Considerations and Clinical Applications in Neuroimaging." *J Magn Reson Imaging* 53(1): 23-37.

Wang Y, Liu T. 2015. "Quantitative susceptibility mapping (QSM): Decoding MRI data for a tissue magnetic biomarker." *Magn Reson Med* 73(1): 82-101.

Woojin Jung, Steffen Bollmann, Jongho Lee. 2020. "Overview of quantitative susceptibility mapping using deep learning: Current status, challenges and opportunities." *NMR in Biomedicine.*

Yablonskiy DA, Haacke EM. 1994. " Theory of NMR signal behavior in magnetically inhomogeneous tissues: the static dephasing regime. ." *Magn Reson Med* 749-763.

Yan F, He N, Lin H, Li R. 2018. "Iron deposition quantification: Applications in the brain and liver." *J Magn Reson Imaging* 48(2): 301-317.

Ziemssen T, Derfuss T, de Stefano N, Giovannoni G, Palavra F, Tomic D, Vollmer T, Schippling S. 2016. "Optimizing treatment success in multiple sclerosis." *J Neurol* 263(6): 1053-65.

2 Repeatability of Susceptibility Separation in Brain

2.1 Introduction

Quantitative Susceptibility mapping (QSM) provides a means to estimate magnetic susceptibility from gradient echo phase images (Haacke EM M. S., 2009; Haacke EM X. Y., 2004; Schafer A, 2009). Magnetic susceptibility sources inside and outside of the brain may affect the magnetic field of each voxel which is measured using phase evolution (Rauscher A S. J., 2005; Shmueli K, 2009; Bilgic B P. A., 2012). The typical reconstruction process involves unwrapping the phase images then removing background field contributions and then dipole inversion (Li W A. A., 2014; Liu S, 2013; Rauscher A B. M., 2008; Özbay PS, 2017; Sun H, 2014; Ferdinand Schweser A. D., 2013; Jing Liu, 2012). The field of QSM has evolved rapidly from pure research to clinical studies, with susceptibility providing unique insight due to its sensitivity to sources such as calcium, iron and myelin (Elkady AM, 2018; Bilgic B P. A., 2012; Yao B, 2009; Liu T E.-W. S., 2013). However, a remaining problem with QSM is the lack of tissue specificity to signal change (Wang Y, 2015; Schweser F D. A., 2016).

Two major susceptibility sources in brain are paramagnetic iron and diamagnetic myelin (Qin, 2011; Carsten Stüber, 2014; Yan F, 2018). Iron can be found throughout the brain, as iron is widely used for brain function both for oxygen transport via heme iron and non-heme iron uses such as neurotransmitter and myelin synthesis (Williams R, 2012). In the basal ganglia, an area of deep grey matter (DGM), the non-heme iron levels are particularly high, while in white matter (WM) myelin levels are higher than grey matter. Each macroscopic voxel is likely to contain a mix of myelin and iron contributions to susceptibility. However, due to their opposing magnetic susceptibility, the two may cancel out phase contrast and thus conventional QSM approaches are not able to separate nor quantify the levels of iron and myelin in the voxel (Lee H, 2021; Lambrecht V, 2020; Shin HG, 2021). In some areas of overwhelming high iron, like the basal ganglia, it may be possible to ignore the myelin contributions and assign QSM changes directly to iron, but more generally across the brain the lack of discrimination between iron and myelin changes is

problematic. This is particularly true of diseases like multiple sclerosis (MS) which can have both demyelination and iron accumulation (Deh K, 2018; Granziera C & Group, 2021; Wisnieff C R. S., 2015). Loss of myelin and gain of iron would both introduce a similar direction of change in susceptibility.

Hence, methods to separate myelin and iron become important as they can provide a route to a more accurate understanding of tissue changes. For example, separation methods could enable better understanding of tissue damage and recovery. Focusing again on MS, accurate maps of demyelination might be possible, if one could separate iron and myelin contributions (Eskreis-Winkler S, 2015). Current alternatives to achieve myelin-specific contrast are either time-consuming like myelin water imaging (A. Mackay, 1994), or lack full specificity like magnetization transfer contrast or diffusion (Van Obberghen E, 2018; Welker KM, 2012).

One solution to improving the specificity of QSM is to pair its analysis with that of the effective transverse relaxation rate (R_2^*). Fortuitously, QSM is often, though not always, performed with a multiple echo gradient echo sequence which enables dual analysis of R_2^* and QSM. Several methods have been developed to distinguish iron and myelin in a voxel using both R_2^* and QSM (Samir D. Sharma, 2017; Jafari R, 2021; Zhang Y, 2019; Chen J, 2021). Fortuitously, the coexistence of iron and myelin in a voxel may affect the acquired signal decay in a different way than it affects the phase evolution. More specifically, magnitude signal dephasing may arise from either paramagnetic or diamagnetic sources, while phase evolution (field changes) will have opposing directions for para and diamagnetic components (Qin, 2011). Since myelin and iron accumulation are both additive for R_2^* yet opposing for QSM, it becomes possible to distinguish directions of change by examining both methods simultaneously. Schweser et. al. for the first time combined QSM and R_2^* to delineate iron accumulation and demyelination (F. Schweser, 2012). Elkady examined R_2^* and QSM changes to try to distinguish myelin or iron, though only iron measures seemed robust in DGM (Elkady AM, 2018; 2017).

These early methods of susceptibility separation still had a large confound of water content changes. For example, R_2^* might drastically increase due to inflammation adding water content, while QSM might not be much affected by water changes. The use of the reversible relaxation component of R_2^*, that is R_2', provides a solution to limit water content confounds and is independent from the irreversible tissue relaxation rate R_2 (Paling D, 2012; Weiskopf N., 2013).

Despite the fact that artifacts related to field inhomogeneity affect the specificity of R_2' in detecting iron, these data suggest that R_2' may be a more specific measure of brain iron content than R_2 or R_2* (Neema M, 2007). Lee et al. introduced a separation method which builds on QSM and R_2' in order to separate para- and diamagnetic susceptibility sources (J Lee, 2017). The idea was further developed by Shin et al. and Emmerich et al, with both groups utilizing three measures: QSM, R_2* and R_2, hence adding an additional sequence to measure R_2, as well as the MEGE sequence for R_2* and QSM (Emmerich J, 2021; Shin HG, 2021). A QSM pipeline has resulted (Shin HG, 2021).

Currently, the use of both R_2' and QSM seems the most promising method for susceptibility separation into dia- and paramagnetic parts with both Shin and Emmerich using similar approaches, although with different definitions of relaxation components (Shin HG, 2021; Emmerich J, 2021). In these papers this separation method had been demonstrated in simulations, phantoms and healthy subjects as well as being applied to MS patients, demonstrating clear ability to separate diamagnetic and paramagnetic components. However, the repeatability of the method remains unknown. Particularly for following changes in an individual, the reliability of the method becomes essential. This work examines reliability of this most promising separation method. We examine the repeatability in brain of the susceptibility separation method introduced by (Shin HG, 2021; Emmerich J, 2021) and its sensitivity to parameter choices, in comparison to conventional QSM utilizing 24 subjects scanned twice at the same location.

2.2 Methods

2.2.1 Data Acquisition

The separation method was tested on 24 healthy subjects (age range of 20 to 49 yrs) who received two scans at the same site (Peter S. Allen MR Research Centre, University of Alberta) on the same system (3T Prisma, Siemens). The mean time between imaging exams was 15 days. Each subject gave written informed consent prior to imaging. The sequence for susceptibility and R2* images was a 3D multi-echo gradient echo with TE1=3.8ms, ΔTE= 5.5ms, 6 echoes, TR=37ms, flip angle=13°, slice thickness of 1.7mm with 88 slices, in-plane resolution of 0.94×0.94 mm^2. The protocol for R_2 images was a dual echo 2D turbo spin echo TE1=10ms, TE2=93ms, TR=4000ms, nominal refocusing flip angle 150°, slice thickness of 3.5 mm with 41 slices and in-plane resolution 0.9×0.9 mm^2. The acquisition times were 5:30 mins and 2:02 mins respectively. Whole brain B1+

maps were acquired using a dedicated Bloch-Siegert B1+ mapping sequence (turbo-flash base), axial-oblique, 1.3x1.3x3 mm^3, 40 slices, FOV 240x240 mm^2 in 39 sec. The exam also included a 3D T1-weighted MPRAGE scan for segmentation.

2.2.2 Post Processing and Registration

For the separation method, the result of conventional QSM is needed as starting point. Also for R_2' both the R_2^* and R_2 maps are needed. For the conventional QSM, a mask was generated from MEGE magnitude images via FSL's brain extraction tool (Smith, 2002) .The phase images were unwrapped using the Laplacian approach (Bagher-Ebadian, 2008). Then variable-radius sophisticated harmonic artifact reduction for phase (V-SHARP) (Li W W. B., 2011) with maximum kernel radius of 9mm was used for background removal and MEDI (Jing Liu, 2012) for susceptibility mapping. The R2* maps were derived using mono-exponential fitting of magnitude images using all 6 echo times (Pei, 2015). Prior to fitting, R_2* maps used a linear field correction to the MEGE magnitudes to remove some of the nonlocal components (Sedlacik, 2014). The R2 maps were generated by modeling the pulse sequence using Bloch equations to account for stimulated echoes and then dictionary fitting (McPhee KC, 2017).

For image registration of scans for each individual, all images from the scan and rescan were rigidly registered to the T1-weighted image of the first scan using FSL (Jenkinson M, 2002). The multiple gradient echo sequence used the third echo while the dual echo turbo spin echo used the T2-weighted echo for registration. This yielded the transformation matrices for each subject that were used to transform QSM, R_2*, and R_2 maps into T1 space of the first scan, providing all maps in a single T1 space. Regions-of interest (ROI) were measured included globus pallidus (GP), putamen, caudate and thalamus in DGM and posterior internal capsule (PIC), body of corpus callosum (BCC) and optic radiation (OR) in WM. Segmentations were done automatically in the same T1 space for regions of interest in DGM using volBrain, (Manjón JV, 2016), while WM segmentations used Johns Hopkins WM Atlas, (Oishi K, 2008). Segmentation masks in DGM were eroded by one voxel in all the directions in order to avoid any error coming from the edges of ROIs. When all the maps were registered, R_2' was calculated by subtraction of R_2 from R_2^*. In some voxels due to noise or artifact, R_2^* might be less than R_2. In these cases, voxels with negative

R_2' values were forced to zero. Negative R_2' values were common at the edges of brain while rare in other parts.

To register all individual data onto a group template, all results were transformed to MNI space using FSL package. The T1-weighted images of the first scan for each subject were processed using modified fsl_anat script (using 1mm MNI template instead of default 2mm), which provided transformation matrices used to transform all the maps from T1 into MNI space.

2.2.3 Susceptibility Separation Model

The susceptibility separation model used the following that was introduced in (Shin et al 2021), and is similar to that introduced by Emmerich et al. to enable paramagnetic and diamagnetic susceptibility sources images utilizing both QSM and the information in R_2':

$$R_2' = R_2^* - R_2 \tag{2.1}$$

R_2* is the effective transverse decay rate of the signal when all the dephasing causes are summed up. R_2 is an irreversible portion of the decay which can be measured by RF refocusing of the reversible R2' portion. Thus R2' is calculated indirectly via the above subtraction equation. Considering a spherical source with a constant magnetic susceptibility, in the case of a static dephasing regime, diffusion effects can be ignored, and the dephasing rate is linearly related to the susceptibility source (Julian Emmerich P. B., 2020). In general, this can be extended to coexisting para and diamagnetic sources:

$$R_2' = \left(D_{r,pos} \left|\chi_{pos}\right| + D_{r,neg} \left|\chi_{neg}\right| \right) \tag{2.2}$$

$D_{r,pos}$ and $D_{r,neg}$ are the relaxometric coefficients for paramagnetic and diamagnetic components, respectively, which are multiplied by the absolute value of the negative and positive susceptibility components χ_{neg} and χ_{pos}. As introduced in (Shin HG 2021), the loss function that the method is trying to minimize is:

$$argmin_{\chi_{pos},\,\chi_{neg}} \left\| W_r \cdot \left\{ {R_2}' - \left(\overline{D_{r,pos}} \cdot \left|\chi_{pos}\right| + \overline{D_{r,neg}} \cdot \left|\chi_{neg}\right| \right) \right\} + i2\pi \cdot W_f \cdot \left\{ f - D_f * \left(\chi_{pos} + \chi_{neg}\right) \right\} \right\|_2^2 + reg(\chi_{pos}, \chi_{neg}) \tag{2.3}$$

Where f and D_f are the local field shift after background field removal and magnetic dipole kernel, respectively. For in-vivo experiments $\overline{D_{r,pos}} = \overline{D_{r,neg}}$. An implicit constraint for positive and negative components is that they must retain their sign and cannot have values more or less than zero, respectively. The relaxometric coefficients are assumed to be spatially invariant. W_r and W_f are weightings for the R_2' and local field shift terms, respectively. The loss function makes a trade-off between R_2' and QSM information. The term $reg(\chi_{pos}, \chi_{neg})$ is a regularization term that prevents susceptibility values from becoming unrealistically large.

In the original work, $\overline{D_{r,pos}}$ was calculated as the slope of R_2' versus susceptibility using 5 iron-rich DGM regions including all subjects. In this work, $\overline{D_{r,pos}}$ was calculated independently for each subject, and only the three largest iron-rich regions were used: GP, caudate and putamen. As in (Shin et al 2021), the fitted slope also assumes that the line passes through the origin. The same value was used for $\overline{D_{r,neg}}$ (Shin HG 2021). Equation (2.3) was solved using the iterative conjugate gradient method. The stop criterion was $\frac{\Delta\chi^n_{pos+neg}}{\chi^{n-1}_{pos+neg}} < 0.01$ or the iterations exceed 15. $\chi^n_{pos+neg}$ is the sum of χ_{pos} and χ_{neg} at nth iteration and $\Delta\chi^n_{pos+neg} = \chi^n_{pos+neg} - \chi^{n-1}_{pos+neg}$. The same stopping criterion was used in the original work. The weights are defined to reduce the contribution of voxels with unreliable R_2'

$$W_r(\boldsymbol{r}) = \begin{cases} W_f(\boldsymbol{r})/10 & where\ R_2'(\boldsymbol{r}) > 30\ \text{Hz}\ or\ R_2'(\boldsymbol{r}) < 1\ \text{Hz}, \\ W_f(\boldsymbol{r}) & otherwise. \end{cases} \quad (2.4)$$

The regularization term is (Shin HG, 2021):

$$reg(\chi_{pos}, \chi_{neg}) = 2 \cdot \lambda_1 \left\| M_{Mag}(\nabla\chi_{total}) \right\|_1 + \lambda_1 \left\| M_{R_2'}(\nabla\chi_{pos}) \right\|_1 + \lambda_1 \left\| M_{R_2'}(\nabla\chi_{neg}) \right\|_1 +$$
$$\lambda_2 \left\| M_{CSF}(\chi_{pos} - \overline{\chi_{pos,CSF}}) \right\|_2^2 + \lambda_2 \left\| M_{CSF}(\chi_{neg} - \overline{\chi_{neg,CSF}}) \right\|_2^2 \quad (2.5)$$

where λ_1 and λ_2 are regularization parameters, ∇ is a gradient operation, χ_{total} is a total susceptibility map calculated as the sum of χ_{pos} and χ_{neg}, M_{Mag} is a binary edge mask from magnitude (Liu T. L., 2011) $M_{R_2'}$ is a binary edge mask from R_2', M_{CSF} is a binary mask of ventricular cerebrospinal fluid (CSF) and $\overline{\chi_{\cdot,CSF}}$ is the mean positive (or negative) susceptibility in M_{CSF} (Liu Z. S., 2018). In this work λ_2 was set to zero as CSF regularization worsened the results. λ_1 was experimentally set to 2. The problem was solved using iterative conjugate gradient

method. In each iteration the values of positive and negative components were checked to ensure they didn't exceed zero. The χ_{pos} and χ_{neg} maps are initialized as the solution of the following two linear equations:

$$D_{r,pos}(\boldsymbol{r}) \cdot |\chi_{pos}(\boldsymbol{r})| + D_{r,neg}(\boldsymbol{r}) \cdot |\chi_{neg}(\boldsymbol{r})| \; = \; R_2{}'(\boldsymbol{r}),$$

$$\chi_{pos} + \chi_{neg} = \chi_{conventional\ QSM} \tag{2.6}$$

Convergence of the method depended on regularization choices. Using large λ_1 (λ_1 >1) helped the method to converge at maximum 5 iterations while small choice of λ_1 (λ_1 <10^{-3}) had an adverse impact which intensified the existing noise. The method did not converge with small λ_1.

All the implementations and codes were done in MATLAB (version R2020a; MathWorks, MA, USA). The codes are available upon receiving a reasonable request.

2.2.4 Statistical Analysis

Intraclass correlation coefficient (ICC) for all the components was measured and reported in the 7 ROIs; GP, Putamen, Caudate, Thalamus in DGM and PIC, BCC and OR in WM. The ICC estimates the ratio of between-subject variance to the total variance which was calculated based on a single-rating, absolute agreement, 2-way mixed-effects model (Koo, 2016).

Paired *t* test and Bland-Altman plot are methods for assessing agreement, and Pearson correlation coefficient is only a measurement for correlation, and therefore, they are nonideal measurements of reliability (Bruton A, 2000; Bland JM, 1986; Brown BW, 1962; WG, 2000). A more practical measurement of reliability should reflect both the extent of correlation and the degree of agreement between all the measurements. Intraclass correlation coefficient (ICC) is the desired index reflecting both indices (Koo, 2016). There are several types of ICC scores which has specific application for different types of experiments. The ICC used in the paper is based on two-way mixed effects model, absolute agreement and single rater (Koo, 2016). For an N by 2 matrix where N is number of subjects (24 in this paper) done 2 scans, the ICC score in each region is calculated as follows:

$$ICC = \frac{MS_R - MS_E}{MS_R + MS_E + \frac{(MS_C - MS_E)}{N}} \tag{2.7}$$

Where MS_R and MS_C are variance of mean squared rows and columns, respectively. MS_E is the variance of mean squared error. Error is the difference between the two scans. The ICC score is equivalent to the ratio of between-subject variance to total variance (McGraw, 1996):

$$ICC = \frac{\sigma_r^2}{\sigma_r^2 + \sigma_e^2 + \sigma_c^2} = \frac{\sigma_r^2}{\sigma_{Total}^2} \tag{2.8}$$

Where σ_r^2, σ_c^2 and σ_e^2 are variance between rows, columns and the error in each value.

Pearson correlation was calculated for each ROI and Bland Altman (BA) plots together with correlation plots were used for better visualization of the data (Klein, 2021). The plots compare conventional QSM, total separation, paramagnetic and diamagnetic components of sources. Histograms of several ROIs have been depicted in order to provide insight into separation method procedure. In addition, spatially normalized maps obtained by averaging each component across all the subjects in MNI space were measured. The normalized maps are calculated for conventional QSM, total, para- and diamagnetic maps from separation method and for relaxation maps (R_2, R_2' and R_2^*). Furthermore, we study the effects on repeatability of varying D_r. The metric used for evaluation is the relative error e between scan and rescan in ROIs:

$$e = \frac{\sum \frac{\chi_1 - \chi_2}{(\chi_1 + \chi_2) * 0.5}}{N} \tag{2.9}$$

χ_1 and χ_2 are susceptibility values of scan and rescan, respectively and N is number of subjects.

2.3 Results

An example of the separation method is shown along with relaxation maps and conventional QSM in figure 2.1 and 2.2; the slice is from the spatially normalized maps of all subjects in MNI space and a single subject, respectively. The conventional QSM and total separation results are consistent with each other. There are a few subtle differences. The paramagnetic map shows strong contrast in iron-rich GP and putamen in DGM. The WM tracts such as internal capsule in the diamagnetic map also are vivid. The results of conventional QSM and paramagnetic and diamagnetic maps are shown in Figure 2.3. This figure shows two slices, one from DGM and one from more superior in the brain, of both scans.

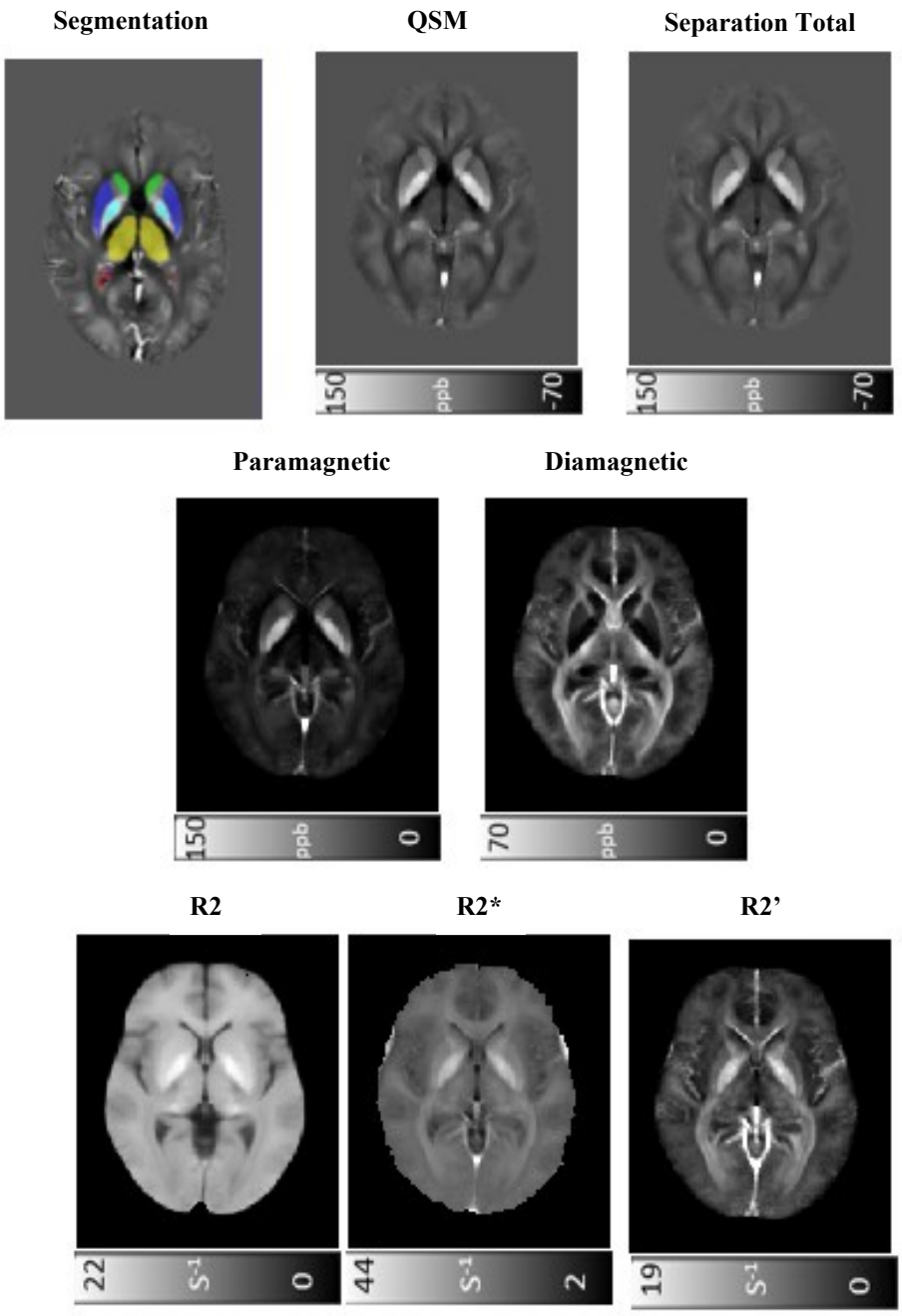

Figure 2.1: Susceptibility separation and its base images in normalized MNI space derived from all subjects. Conventional QSM, Results of applying separation method and relaxation maps. Total separation (paramagnetic + diamagnetic) is consistent with conventional QSM both visually and quantitatively. The paramagnetic component has large values in GP and Pt as expected. The diamagnetic component has small values in DGM iron-rich ROIs such as GP and Pt which confirms the regions have a small portion of myelin. The diamagnetic map is large in WM tracts containing high amount of myelin such internal capsule (IC). Note, the diamagnetic map shows the absolute values. The R_2, R_2^* and R_2' relaxation maps in the bottom row illustrate the source relaxation images. Susceptibility maps have units of ppb while relaxation maps use s^{-1}. For DGM a segmentation map is also shown overlaying on a subject's conventional QSM in the

first row. The colors red, green, yellow, blue and cyan indicate CSF, caudate, thalamus, putamen and GP, respectively.

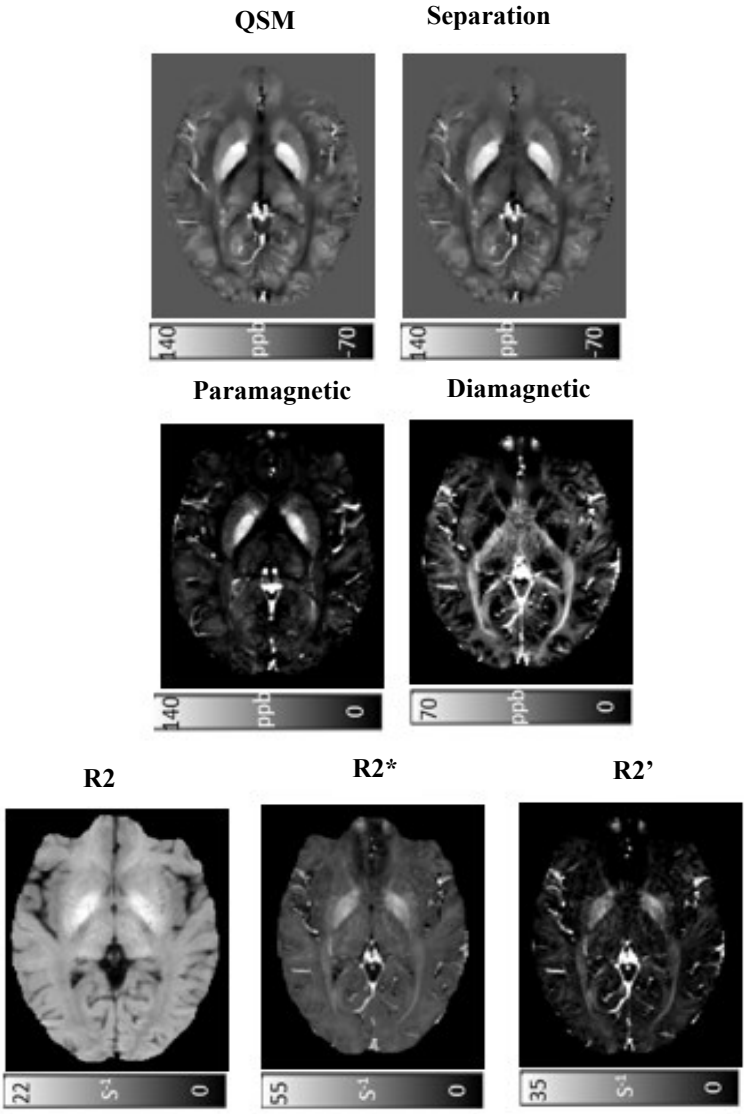

Figure 2.2: Susceptibility separation and its base images of one subject. Conventional QSM, Results of applying separation method and relaxation maps. Total separation (paramagnetic + diamagnetic) is consistent with conventional QSM both visually and quantitatively. The paramagnetic component has large values in GP and Pt as expected. The diamagnetic component has small values in DGM iron-rich ROIs such as GP and Pt which confirms the regions have a small portion of myelin. The diamagnetic map is large in WM tracts containing high amount of myelin such internal capsule (IC). Note, the diamagnetic map shows the absolute values. The R_2, R_2^* and R_2' relaxation maps in the bottom row illustrate the source relaxation images. Susceptibility maps have units of ppb while relaxation maps use s^{-1}.

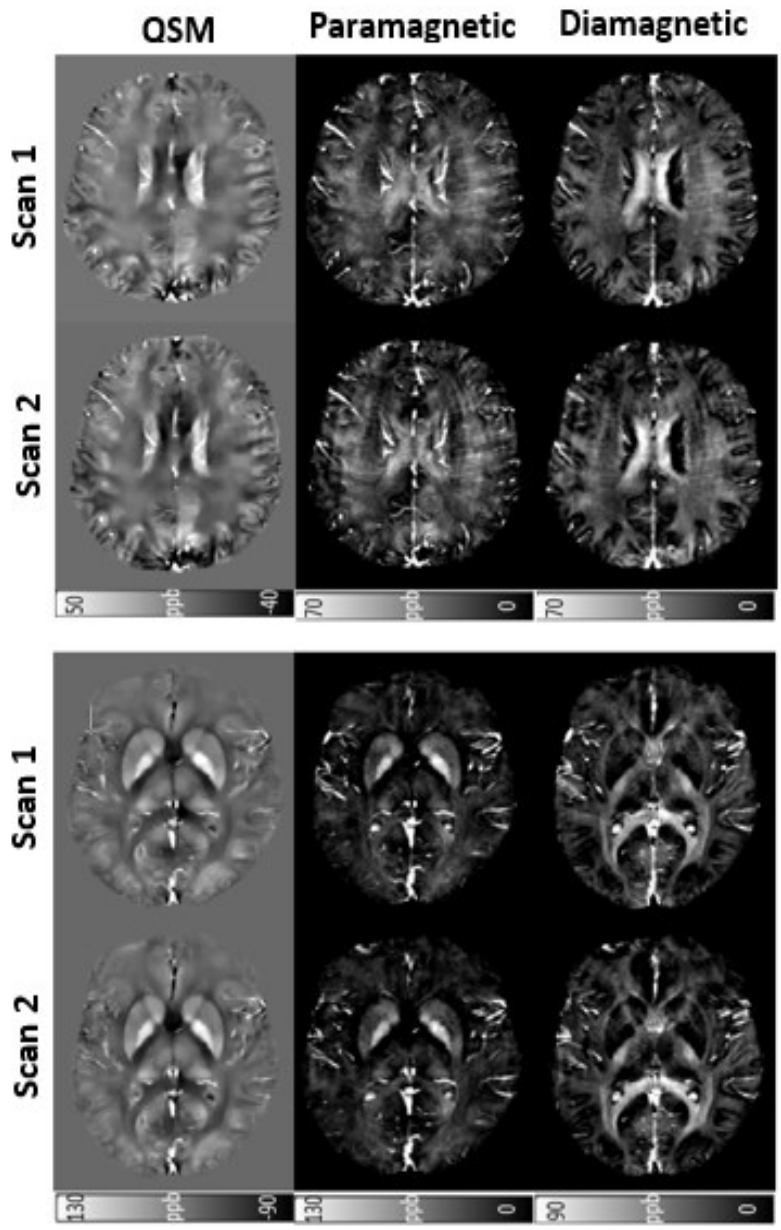

Figure 2.3: Results of conventional QSM and the separation method on two scans of a subject. The top pictures show top brain and bottom pictures show deep gray matter. The left column pictures are conventional QSM results, the middle and right column are paramagnetic and diamagnetic maps, respectively, resulted from applying the separation method

The data from both scans for 7 ROIs are depicted in figure 2.4 as scatter plots, with conventional and total QSM, as well as paramagnetic and diamagnetic components all shown on each plot. In DGM compared to WM, generally the values of scan-rescan show a better consistency and repeatability except in thalamus where susceptibility values are small.

Repeatability and bias are examined in more detail in Figure 2.5 which demonstrates the BA plots for all ROIs. In iron-rich regions, GP, Putamen and Caudate, the diamagnetic component has small mean but large error which indicates that the diamagnetic component in iron-rich regions is not reliable. The means of scans in Caudate are in the range of [-15, 0]ppb while the error is within [-4, 6]ppb. The corresponding means range of GP and Putamen are [-5, -1]ppb and [-15, -7]ppb and their error ranges are [-5, 2]ppb and [-6, 6]ppb, respectively. The WM regions are more disparate as in PIC a shift between conventional QSM and total separation is observed whereas total separation values are the same as conventional QSM in OR and BCC. These differences in PIC arise from a few reasons. First, the net susceptibility value of PIC from conventional QSM is more negative ([-48, -20]ppb) than BCC ([-20, -6]ppb) and OR ([-30, -12]ppb). When the net value is highly negative, the gap between paramagnetic and diamagnetic is large as well. Such a large gap can be observed in PIC (figure 2.5(e)). As a result, a relatively small paramagnetic component is expected in order to be highly diamagnetic, which is true in PIC. Second, the R_2' in PIC is lower than BCC and OR which leads to smaller absolute values for both diamagnetic and paramagnetic components. It can be verified in figure 2.5(h) when R_2' values of PIC in red circles are closer to zero. Together these two cause the paramagnetic value in many voxels to be zero and then equation (3), in order to adjust loss for R_2', starts decreasing only the diamagnetic values as the paramagnetic is already zero and cannot decrease. Then the net susceptibility is shifted towards zero. The first reason which is a significant gap between the components, caused the same issue in GP where an observable shift occurred in total separation compared to conventional QSM. The standard deviation (SD) and limit of agreement (LOA) were calculated for all the methods and components together.

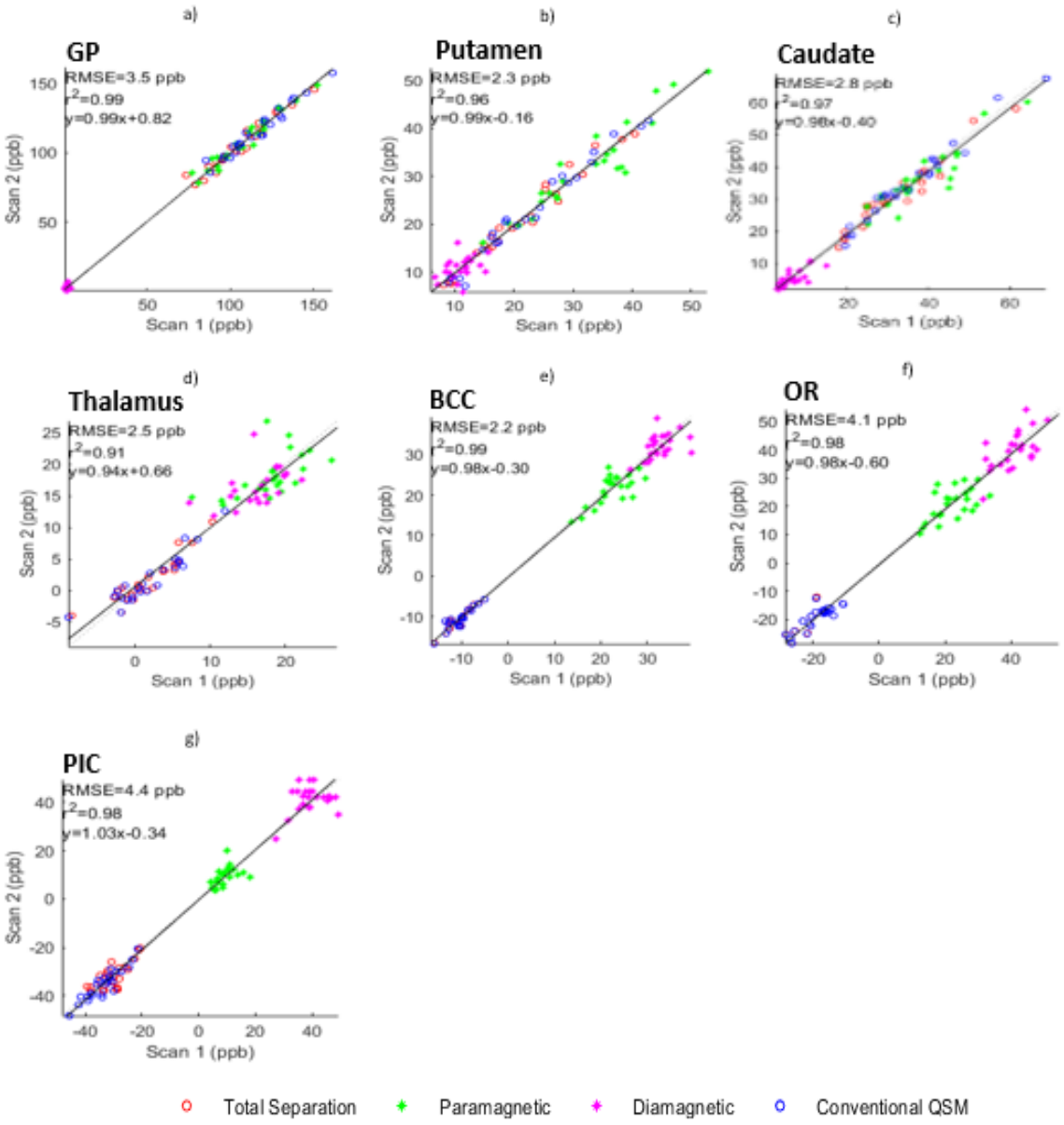

Figure 2.4: Scatter plots from both scans illustrate the range of values with all methods plotted in each panel (total and conventional susceptibility, diamagnetic and paramagnetic components). For better visualization of the diamagnetic component the absolute value is plotted. GP (a), Putamen(b), Caudate (c) and Thalamus (d) are DGM regions which (except thalamus) show a large difference between total separation and conventional QSM. BCC (e), OR (f), PIC (g) are WM regions. All the charts include conventional QSM (blue circle), total separation (red circle), paramagnetic component (green asterisk) and diamagnetic component (pink asterisk). All the values are in ppb. The black line indicates y=x.

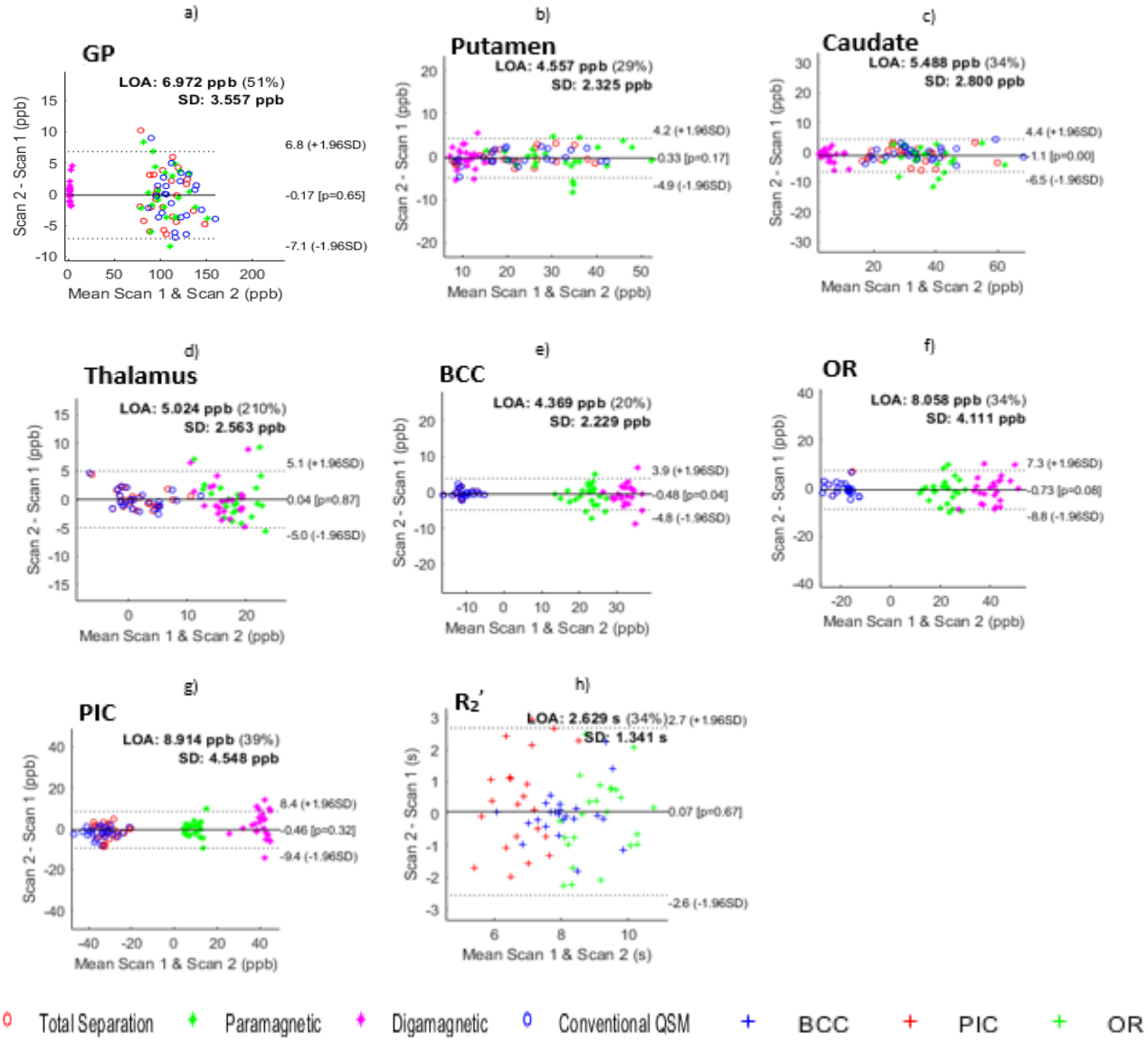

Figure 2.5: BA plots for the 4 DGM and 3 WM regions showing the four susceptibility outcomes, as well as R_2' BA plot for the 3 WM regions. The BA plots use a variable y-axis to show the spread of the data. GP (a), Putamen (b), Caudate (c) and Thalamus (d) are DGM regions. Except Th, the rest have tiny diamagnetic components which causes a shift in total separation with respect to conventional QSM. BCC (e), OR (f), PIC (g) are WM regions. All the charts include conventional QSM (blue circle), total separation (red circle), paramagnetic component (green circle) and diamagnetic component (pink circle) (plots a-g). For easier visualization, instead of actual value, the absolute value is used for diamagnetic components only. The R2' BA plot of 3 WM regions (h) is depicted for better illustration of their differences.

The ICC scores for all the 7 ROIs are illustrated in figure 2.6. Overall, the best scores belonged to conventional QSM in both DGM and WM regions with average scores of 0.97 and 0.88, respectively. The diamagnetic component had the lowest scores in both DGM and WM regions with average scores of 0.45 for both. For paramagnetic components, GP had the largest ICC score (0.98) and thalamus the least ICC score (0.81) in DGM. BCC had the best and PIC had the worst overall performance in WM with average scores of 0.74 and 0.59 over all the components and methods, respectively. For the paramagnetic component the largest and least ICC indices in WM belonged to BCC (0.69) and PIC (0.48), respectively. For the diamagnetic component OR (0.61) and PIC (0.27) had the largest and the least ICC scores, respectively. Due to aforementioned reasons, PIC is not as reliable as BCC and OR when the separation method is used. In conventional QSM, PIC has a larger score (0.88) than OR (0.85) but when the separation method is used PIC's ICC scores drops dramatically (0.72) while OR is barely affected (0.84). Overall, the total separation had larger scores comparing to paramagnetic and diamagnetic components, but total separation serves no distinct value over conventional QSM. R_2' relaxation showed a significant variation in DGM and WM and overall R_2' is less reliable than conventional QSM. Therefore, total separation which is compromise between conventional QSM and R_2', had scores between these two.

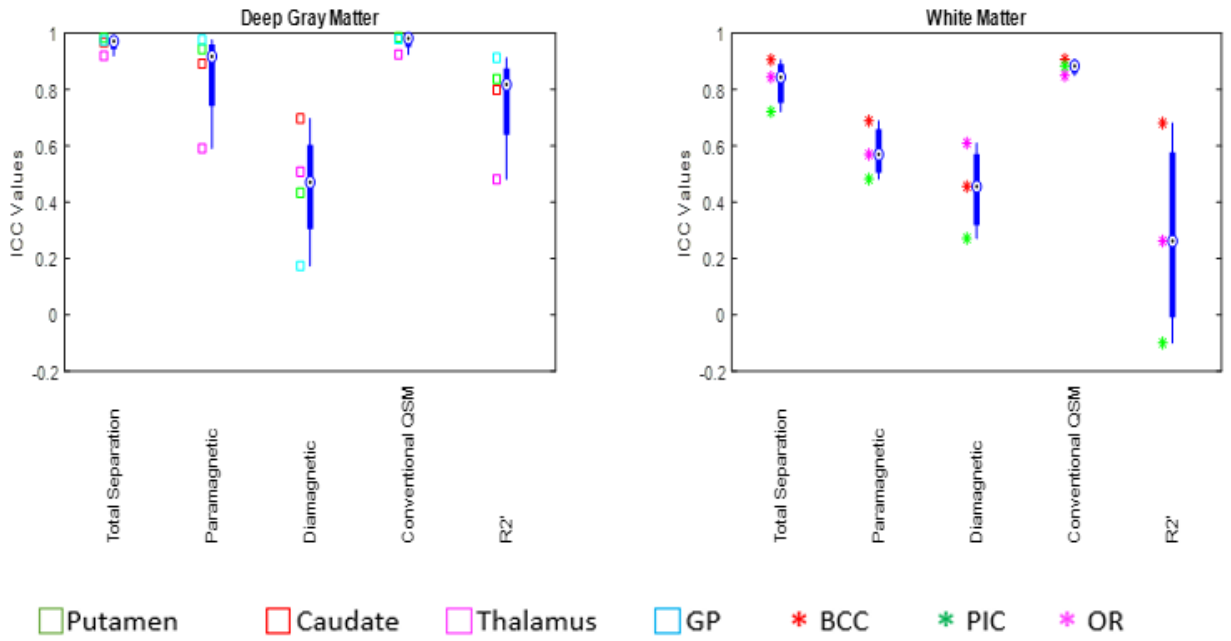

Figure 2.6: The ICC scores of DGM and WM regions. The DGM regions due to their high iron content show a high repeatability in their net susceptibility values by both total separation and conventional QSM. The diamagnetic component has the lowest repeatability in both DGM and WM, overall. PIC is the least repeatable ROI in WM and Thalamus is least repeatable ROI in DGM. Total separation showed a stronger repeatability comparing to diamagnetic and paramagnetic components; however, the purpose of the method is the separation of components.

The D_r values from all subjects had a mean of 151.3 and SD of 20.1. In addition figure 2.7 shows the correlation and BA plots for D_r. The correlation coefficient was 0.79 and the slope of fitted line was 0.89. The limit of agreement (LOA) was 20.4 and the SD of the data was 10.4. Effects of varying the relaxometry coefficient D_r in paramagnetic and diamagnetic components are shown in Tables 1 and 2, reporting the relative error between scan and rescan in each ROI. In these tables, the same D_r value is applied for all subjects, unlike the results reported earlier that use an independent D_r calculation for each scan. Optimal D_r for best repeatability varies with structure and component. Best repeatability for D_r was in the range [180, 230]s^{-1} for paramagnetic components in DGM and diamagnetic components in WM. In contrast, the best repeatability was achieved with the lowest D_r tested ($45s^{-1}$) for the diamagnetic component in iron-rich DGM, or paramagnetic in WM. In thalamus where there is no dominant magnetic component, para- and diamagnetic components had the minimum error at $D_r = 230s^{-1}$.

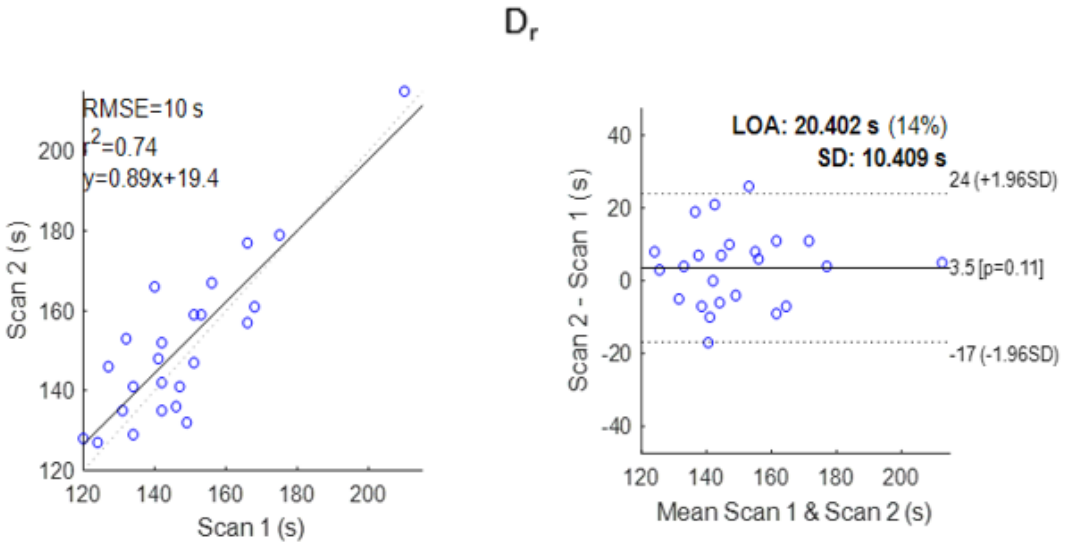

Figure 2.7: The correlation and BA plots of relaxometric coefficient (D_r). (a) correlation coefficient was r^2 = 0.74 and the slope of fitted line was 0.89. (b) The BA plot shows a limit of agreement (LOA) of 20.4 and SD of 10.4. The D_r values are clustered in the range [120,180] with one outlier at much higher levels due to extremely high $R_2^{'}$ values in the three ROIs arising partly from artifacts in the R_2* maps.

Table 1: Paramagnetic component mean (M) relative difference error (%) and percent standard deviation (S) over all subjects for different D_r values. The lowest errors are bolded.

D_r (s^{-1})	45		80		115		180		230		310		420		640	
	M	S	M	S	M	S	M	S	M	S	M	S	M	S	M	S
GP	4.8	0.05	4.0	0.04	3.6	0.04	**3.2**	**0.03**	3.3	0.03	25.0	0.48	57.7	0.56	7.16	0.05
Thalamus (Th)	15.2	0.16	15.2	0.15	15.1	0.15	14.9	0.14	**14.7**	**0.13**	19.7	0.20	45.9	0.41	15.1	0.15
Putamen (Pt)	11.1	0.09	10.2	0.08	9.5	0.07	8.6	0.07	**8.0**	**0.06**	18.8	0.25	45.8	0.41	10.7	0.12
Caudate (Ca)	10.5	0.10	9.6	0.09	9.1	0.09	8.4	0.08	**8.0**	**0.07**	25.7	0.30	58.7	0.56	13.1	0.13
BCC	**6.04**	**0.06**	6.34	0.07	6.73	0.07	7.76	0.07	8.62	0.08	13.5	0.21	27.3	0.31	12.8	0.11
PIC	**24.8**	**0.15**	27.9	0.18	29.4	0.19	28.5	0.20	27.1	0.18	42.6	0.44	91.6	0.61	44.7	0.36
OR	**12.2**	**0.09**	13.1	0.09	14.4	0.10	17.4	0.13	19.4	0.15	32.0	0.32	54.5	0.50	44.6	0.34

Table 2: Diamagnetic component mean (M) relative difference error (%) and standard deviation (S) over all subjects for different D_r values. The lowest errors are bolded.

D_r (s^{-1})	45		80		115		180		230		310		420		640	
	M	S	M	S	M	S	M	S	M	S	M	S	M	S	M	S
GP	**10.8**	**0.08**	19.6	0.12	39.1	0.21	79.3	0.50	124	0.54	68.2	1.29	141	0.58	67.9	0.46
Thalamus (Th)	15.5	0.16	15.4	0.16	15.3	0.15	14.9	0.14	**14.4**	**0.14**	18.9	0.25	42.6	0.43	15.3	0.13
Putamen (Pt)	**14.9**	**0.12**	16.9	0.14	18.5	0.15	20.2	0.16	20.5	0.17	38.7	0.56	74.0	0.61	37.7	0.35
Caudate (Ca)	**14.9**	**0.13**	18.2	0.15	21.4	0.17	25.2	0.21	29.1	0.22	55.1	0.90	1.06	0.72	55.3	0.42
BCC	5.61	0.06	5.51	0.06	5.42	0.06	5.26	0.05	**5.16**	**0.05**	7.24	0.10	18.0	0.22	6.85	0.07
PIC	17.5	0.11	15.8	0.10	14.5	0.10	12.7	0.09	**11.7**	**0.09**	24.2	0.35	61.2	0.50	17.6	0.25
OR	10.4	0.08	10.0	0.07	9.65	0.07	9.09	0.07	**8.73**	**0.07**	16.6	0.23	34.7	0.40	12.1	0.12

For paramagnetic maps in DGM, the optimal scan-rescan difference errors were 3.2%, 14.7%, 8% and 8% in GP, thalamus, putamen and caudate, respectively. While optimal diamagnetic errors in WM are 5.2%, 11.7% and 8.7% in BCC, PIC and OR, respectively. As paramagnetic is the minor component in WM, its error rates are larger than diamagnetic in the measured WM tracts. The errors for paramagnetic maps in WM are 6.04%, 24.8% and 12.2% in BCC, PIC and OR, respectively. Since diamagnetic is the minor component in DGM (except Th), its errors are higher. Diamagnetic errors in DGM are 10.8%, 14.4%, 14.9% and 14.9% in GP, thalamus, putamen and caudate, respectively.

2.4 Discussion

The separation method showed lower repeatability than conventional QSM in terms of ICC scores in both paramagnetic and diamagnetic components as well as the total value. Yet the separation method ICC scores are interpreted to have good repeatability. Scores from 0 to 0.5 means no repeatability, from 0.5 to 0.75 means moderate, from 0.75 to 0.9 means good and from 0.9 to 1

means excellent repeatability (Koo, 2016). The total separation's ICC scores were only slightly less than conventional QSM from 0.01 to 0.03. The diamagnetic component exhibited the least ICC scores in all the measured ROIs. Overall, the paramagnetic and diamagnetic components showed less repeatability in comparison with conventional QSM. Significant gaps between paramagnetic and diamagnetic components and low R_2' values have impact on the total separation and repeatability. These two agents in some regions can lead to a shift toward zero in total separation depending on the extent of the two effects. PIC, GP, caudate and putamen are examples where the shift occurs.

The separation model was developed to distinguish the paramagnetic and diamagnetic components in each voxel which needs a combination of information from local field shift and R_2'. Local field shift is subject to many noise sources such as changes at air-tissue and tissue-vein interfaces and noises at edges where harmonic background removal is not able to perform well. A possible way to reduce artifacts is finding an optimal pipeline for conventional QSM whose results are adaptive with the separation pipeline. Furthermore, R_2^* maps vary between each scan depending on the head tilt, subject motion, magnetic field inhomogeneity and shimming (Zhang Y, 2019). Head tilt in WM leads to different tract orientations. The change in orientation due to anisotropy effects of susceptibility sources will create a different local field shift (Kaden E, 2020; Li W W. B., 2012). Due to the mentioned reasons several patients had a shift and change of variance in their R_2' histograms as several subjects were found to have their head tilted.

The current separation model does not consider fat-water chemical shift, water compartmentalization and susceptibility anisotropy (Shin HG, 2021). While the R_2 mapping pipeline is quite repeatable, the shifts in R_2^* can cause problematic maps. Figure 2.8 contains difference maps of a subject's two scans as well the two scans. The artifact occurred in GP is indicated with red circle. Conventional QSM (left column) had no sign of artifact while the paramagnetic component (right column) and R_2^* (middle column) have a black region in GP. The artifact arose from the large difference between the two scans. This artifact at first originated from R_2^* and then propagated to R_2' and then to the paramagnetic map. Since conventional QSM can remove the field disturbance and inhomogeneities in the background field removal stage (Schweser F R. S., 2017), the disturbed field existing in R_2^*, didn't exist in local field shift. Maybe a proper background field correction method for R_2^* images can mitigate this issue.

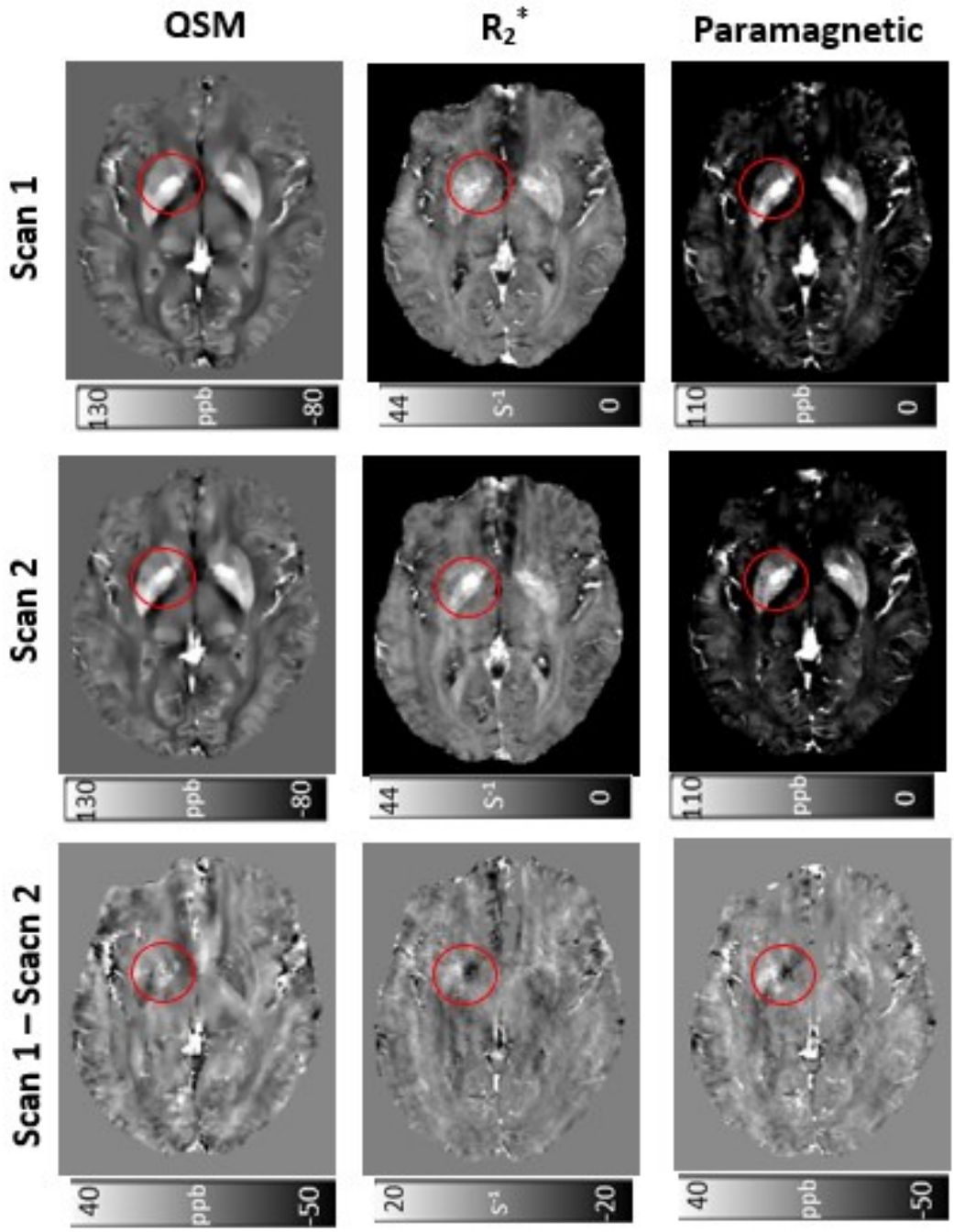

Figure 2.8: The difference maps of a subject from scan-rescan illustrating an artifact originating from the R2* map. Top row, middle row and bottom row indicate scan 1, scan 2 and difference maps respectively. Left column, middle column and right column indicate conventional QSM, R_2^* and paramagnetic maps respectively.

Another path to explore is trying a local relaxometric coefficient (D_r) for each ROI. As it might help the separation method to account for anisotropy and non-spherical susceptibility effects. So far, a global D_r is estimated from iron-rich regions in DGM (Shin et al, 2021) first and then extended to the whole brain. However, the method could suffer from overestimation of D_r, since, conventional QSM underestimates susceptibility values when compared to ground truth methods (Samir D. Sharma, 2017). In addition, calculation of R_2^* relaxation rates by mono exponential fitting requires small voxel sizes to ensure a minimal contribution from background field perturbations. However, the voxel size is also controlled by available scan time and SNR limits which might lead to a slight overestimation of relaxation rates for lower image resolution (Emmerich J, 2021).

The relaxometric coefficient plays a significant role in repeatability assessment. Choosing a constant D_r for a subject was used in the previous works (Shin HG, 2021; Emmerich J, 2021). Here, we used a separate D_r calculation for each subject and scan. However, as table 1 and 2 suggest, when using a predefined global D_r for all subjects, least repeatability errors were shown to vary with structure. The results show if the dia- or paramagnetic component is dominant the D_r coefficient with least error will be in range of [180, 230] but if the component is minor, optimal choice of the coefficient will be much reduced, in this case to the lowest value tested ($45s^{-1}$). Note that the experimental D_r values used in most of this work used determined from strong paramagnetic sources in DGM, but produced D_r values slightly below the range given above.

In addition, using a local D_r might overcome the anisotropic effects in WM which the global D_r cannot overcome. A possible path to explore could be evaluating impacts of varying D_r. The idea can be further extended to evaluation of varying $D_{r,pos}$ and $D_{r,neg}$. In equation [2.3], the λ_1 value adjusts regularization weights. Varying λ_1 can affect the D_r value as high regularization supresses changes from the data fidelity term. Thus changing λ_1 could alter the optimal D_r values. Furthermore, we tested using a mean D_r for each subject based on their two scans, rather than an independent D_r for each scan. This only slightly improved ICC scores in WM but had no change in DGM.

A possible way to improve the separation method is improving R_2^* and R_2 which are the two components of R_2'. The sequence used for R_2 mapping in this work had low resolution in the slice direction (3.5mm) due to SNR limitations of 2D sequences but also to keep scan time reasonable.

Thus the slice dimensions for R_2 mapping was much larger, and may have been affected by boundary partial voluming, particularly near CSF. To mitigate effects, ROIs were eroded by one voxel and R_2 maps were interpolated to the same voxel dimensions as R_2* maps. A higher resolution R_2 mapping sequence might be possible with 3D methods, though these can be time consuming. On the other hand, R_2^* showed less robustness to noise and also less repeatability than conventional QSM and R_2 due to the presence of field inhomogeneities (Leutritz, 2020). Only a simple signal correction for linear background fields was performed using adjacent voxels (Sedlacik, 2014). Ordidge et al. developed a method of field inhomogeneity correction that allows the separation of global and local field inhomogeneities, leading to more accurate T_2* measurements and hence, T_2' values (Ordidge RJ G. J., 1994). This approach relies on repeat scans with varying slice refocusing gradients.

Another difficulty with the separation is motion within scans or between scans. While rigid registration can correct for between-scan motion, the background field is altered if the head is tilted differently. Within scan motion could be improved with prospective motion correction to correct patient motion in brain (Maclaren, 2013).

2.5 Conclusion

This work measured repeatability of a susceptibility separation method at 3T. The results demonstrated a reduced repeatability factor in the susceptibility separation components with respect to conventional QSM. The paramagnetic component performed best in iron-rich deep grey matter, while the diamagnetic results were similar in deep grey and white matter. The reduced repeatability largely was due to R_2' variability originating from R_2^*. Low resolution R_2 imaging also can lead to contamination from CSF, if not carefully managed which can result in large paramagnetic and diamagnetic components. The D_r value for highest repeatability was found to be varying depending on whether paramagnetic or diamagnetic components dominated. Overall, qualitative depiction of the paramagnetic and diamagnetic components was achieved, though further improvements is susceptibility methods are warranted for precise quantitative results.

References

A. Mackay, K. Whittall, J. Adler, D. Li, D. Paty, and D. Graeb. 1994. "In vivo visualization of myelin water in brain by magnetic resonance." *Magnetic Resonance in Medicine* 31: 673–677.

Bagher-Ebadian, H., Jiang, Q., Ewing, J.R. 2008. "A modified fourier-based phase unwrapping algorithm with an application to MRI venography." *J. Magn. Reson. Imaging* 27: 649–652.

Bilgic B, Pfefferbaum A, Rohlfing T, Sullivan E V, Adalsteinsson E. 2012. "MRI estimates of brain iron concentration in normal aging using quantitative susceptibility mapping." *Neuroimage* 59: 2625–35.

Bland JM, Altman DG. 1986. "Statistical methods for assessing agreement between two methods of clinical measurement." *Lancet.* 1: 307–310.

Brown BW, Jr., Lucero RJ, Foss AB. 1962. "A situation where the Pearson correlation coefficient leads to erroneous assessment of reliability." *J Clin Psychol* 18: 95–97.

Bruton A, Conway JH, Holgate ST. 2000. "Reliability: what is it, and how is it measured?" *Physiotherapy* 86: 94–99.

Carsten Stüber, Markus Morawski, Andreas Schäfer, Christian Labadie, Miriam Wähnert, Christoph Leuze, Markus Streicher, Nirav Barapatre, Katja Reimann, Stefan Geyer, Daniel Spemann, Robert Turner. 2014. "Myelin and iron concentration in the human brain: a quantitative study of MRI contrast." *Neuroimage* 95-106.

Chen J, Gong NJ, Chaim KT, Otaduy MCG, Liu C. 2021. "Decompose quantitative susceptibility mapping (QSM) to sub-voxel diamagnetic and paramagnetic components based on gradient-echo MRI data." *Neuroimage* 242:118477.

Deh K, Ponath GD, Molvi Z, Parel GT, Gillen KM, Zhang S, Nguyen TD, Spincemaille P, Ma Y, Gupta A, Gauthier SA, Pitt D, Wang Y. 2018. "Magnetic susceptibility increases as diamagnetic molecules breakdown: Myelin digestion during multiple sclerosis lesion formation contributes to increase on QSM." *J Magn Reson Imaging* 48(5): 1281-1287.

Elkady AM, Cobzas D, Sun H, Blevins G, Wilman AH. 2018. "Discriminative analysis of regional evolution of iron and myelin/calcium in deep gray matter of multiple sclerosis and healthy subjects." *J Magn Reson Imaging.*

Elkady AM, Cobzas D, Sun H, Blevins G, Wilman AH. 2017. "Progressive iron accumulation across multiple sclerosis phenotypes revealed by sparse classification of deep gray matter." *J Magn Reson Imaging* 46(5): 1464-1473.

Emmerich J, Bachert P, Ladd ME, Straub S. 2021. "On the separation of susceptibility sources in quantitative susceptibility mapping: Theory and phantom validation with an in vivo application to multiple sclerosis lesions of different age." *J Magn Reson.*

Emmerich Julian, Peter Bachert, Mark E. Ladd, Sina Straub. 2020. "On the influence of two coexisting species of susceptibility-producing structures on the R2∗ relaxation rate." *Magnetic Resonance Imaging* 170-177.

Eskreis-Winkler S, Deh K, Gupta A, Liu T, Wisnieff C, Jin M, Gauthier SA, Wang Y, Spincemaille P. 2015. "Multiple sclerosis lesion geometry in quantitative susceptibility mapping (QSM) and phase imaging." *J Magn Reson Imaging* 42(1): 224-9.

Granziera C, Wuerfel J, Barkhof F, Calabrese M, De Stefano N, Enzinger C, Evangelou N, Filippi M, Geurts JJG, Reich DS, Rocca MA, Ropele S, Rovira À, Sati P, Toosy AT, Vrenken H, Gandini Wheeler-Kingshott CAM, Kappos L, and MAGNIMS Study Group. 2021. "Quantitative magnetic resonance imaging towards clinical application in multiple sclerosis." *Brain* 144(5): 1296-1311.

Haacke EM, Mittal S, Wu Z, Neelavalli J, Cheng YC. 2009. "Susceptibility-weighted imaging: technical aspects and clinical applications, part 1." *AJNR Am J Neuroradiol* 30(1): 19-30.

Haacke EM, Xu Y, Cheng YC, Reichenbach JR. 2004. "Susceptibility weighted imaging (SWI)." *Magn Reson Med* 52(3): 612-18.

Helms G., Dathe H., Dechent P. 2008a. "Quantitative FLASH MRI at 3T using a rational approximation of the Ernst equation." *Magn. Reson. Med.* 667–672.

Helms G., Dathe H., Kallenberg K., Dechent P. 2008b. "High-resolution maps of magnetization transfer with inherent correction for RF inhomogeneity and T1 relaxation obtained from 3D FLASH MRI. ." *Magn. Reson. Med* 1396–1407.

J Lee, Y Nam, JY Choi, H Shin, T Hwang, J Lee. 2017. "Separating positive and negative susceptibility sources in QSM." *Intl. Soc. Magn. Reson. Med.* 25.

Jafari R, Hectors SJ, Koehne de González AK, Spincemaille P, Prince MR, Brittenham GM, Wang Y. 2021. "Integrated quantitative susceptibility and R2 * mapping for evaluation of liver fibrosis: An ex vivo feasibility study." *NMR Biomed* 34(1).

Jenkinson M, Beckmann CF, Behrens TE, Woolrich MW, Smith SM. 2002. "FSL." *Neuroimage.*

Jiji S, Smitha KA, Gupta AK, Pillai VP, Jayasree RS. 2013. "Segmentation and volumetric analysis of the caudate nucleus in Alzheimer's disease." *Eur J Radiol* 1525-1530.

Jing Liu, Tian Liu, Ludovic de Rochefort, James Ledoux, Ildar Khalidov, Weiwei Chen, A. John Tsiouris, Cynthia Wisnie, and Yi Wang. 2012. "Morphology enabled dipole inversion for quantitative susceptibility mapping using structural consistency between the magnitude image and the susceptibility map." *NeuroImage* 2560-2568.

Klein, R. 2021. "Bland-Altman and Correlation Plot - File Exchange - MATLAB Central [WWW Document]. MATLAB Cent. File Exch."

Koo, T.K., Li, M.Y. 2016. "A Guideline of Selecting and Reporting Intraclass Correlation Coefficients for Reliability Research. ." *J. Chiropr. Med* 155–163.

Lambrecht V, Hanspach J, Hoffmann A, Seyler L, Mennecke A, Straub S, Marxreiter F, Bäuerle T, Laun FB, Winkler J. 2020. "Quantitative susceptibility mapping depicts severe myelin deficit and iron deposition in a transgenic model of multiple system atrophy." *Exp Neurol* 329.

Lee H, Cho H, Lee MJ, Kim TH, Roh J, Lee JH. 2021. "Differential Effect of Iron and Myelin on Susceptibility MRI in the Substantia Nigra." *Radiology* 301(3): 682-691.

Leutritz, T., Seif, M., Helms, G., Samson, R. S., Curt, A., Freund, P., & Weiskopf, N. 2020. "Multiparameter mapping of relaxation (R1, R2*), proton density and magnetization transfer saturation at 3 T: A multicenter dual-vendor reproducibility and repeatability study." *Hum Brain Mapp* 4232-4247.

Li W, Avram A V., Wu B, Xiao X, Liu C. 2014. "Integrated Laplacian-based phase unwrapping and background phase removal for quantitative susceptibility mapping." *NMR Biomed* 219-227.

Li W, Wu B, Liu C. 2011. " Quantitative susceptibility mapping of human brain reflects spatial variation in tissue composition." *Neuroimage* 1645-1656.

Liu S, Buch S, Haacke EM. 2013. "Background field removal based on local complex phase unwrapping and spherical mean value property." *21st Annual Meeting of ISMRM* . Salt Lake City, Utah. 2496.

Liu T, Eskreis-Winkler S, Schweitzer AD, Chen W, Kaplitt MG, Tsiouris AJ, Wang Y. 2013. "Improved subthalamic nucleus depiction with quantitative susceptibility mapping." *Radiology* 269: 216–23.

Liu, T., Liu, J., Rochefort, L. de, Spincemaille, P., Khalidov, I., Ledoux, J.R., Wang, Y. 2011. "Morphology enabled dipole inversion (MEDI) from a single-angle acquisition: Comparison with COSMOS in human brain imaging." *Magnet Reson Med* 66: 777–783.

Liu, Z., Spincemaille, P., Yao, Y., Zhang, Y., Wang, Y. 2018. "MEDI+0: Morphology enabled dipole inversion with automatic uniform cerebrospinal fluid zero reference for quantitative susceptibility mapping." *Magnet Reson Med* 79: 2795-2803.

Manjón JV, Coupé P. 2016. "volBrain: An Online MRI Brain Volumetry System." *Front Neuroinform.*

María-Trinidad Herrero, Carlos Barcia, Juana Mari Navarro. 2002 . "Functional anatomy of thalamus and basal ganglia." *Child's Nerv Syst* 386–404.

McGraw, K. O., & Wong, S. P. . , 1(1), 30. 1996. "Forming inferences about some intraclass correlation coefficients." *Psychological methods* 30-46.

McPhee KC, Wilman AH. 2017. "Transverse relaxation and flip angle mapping: Evaluation of simultaneous and independent methods using multiple spin echoes." *Magn Reson Med* 2057-2065.

Mure H, Hirano S, Tang CC, et al. 2011. "Parkinson's disease tremor-related metabolic network: characterization, progression, and treatment effects." *NeuroImage* 1244-1253.

Neema M, Stankiewicz J, Arora A, Dandamudi VS, Batt CE, Guss ZD, Al-Sabbagh A, Bakshi R. 2007. "T1- and T2-based MRI measures of diffuse gray matter and white matter damage in patients with multiple sclerosis." *J Neuroimaging* 17: Suppl 1:16S-21S.

Oishi K, Zilles K, Amunts K, Faria A, Jiang H, Li X, Akhter K, Hua K, Woods R, Toga AW, Pike GB, Rosa-Neto P, Evans A, Zhang J, Huang H, Miller MI, van Zijl PC, Mazziotta J, Mori S. 2008. "Human brain white matter atlas: identification and assignment of common anatomical structures in superficial white matter." *Neuroimage* 447-57.

Ordidge RJ, Gorell JM, Deniau JC, Knight RA, Helpern JA. 1994. "Assessment of relative brain iron concentrations using T2-weighted and T2*-weighted MRI at 3 Tesla." *Magn Reson Med* 335-41.

Özbay PS, Deistung A, Feng X, Nanz D, Reichenbach JR, Schweser F. 2017. "A comprehensive numerical analysis of background phase correction with V-SHARP." *NMR Biomed.* 30(4).

Paling D, Tozer D, Wheeler-Kingshott C, Kapoor R, Miller DH, Golay X. 2012. "Reduced R2' in multiple sclerosis normal appearing white matter and lesions may reflect decreased myelin and iron content." *J Neurol Neurosurg Psychiatry* 83(8): 785-92.

Pei, M., Nguyen, T.D., Thimmappa, N.D., Salustri, C., Dong, F., Cooper, M.A., Li, J., Prince, M.R., Wang, Y. 2015. "Algorithm for fast monoexponential fitting based on Auto-Regression on Linear Operations (ARLO) of data." *Magn Reson Med* 843-850.

Qin, Y., Zhu, W., Zhan, C. et al. 2011. "Investigation on positive correlation of increased brain iron deposition with cognitive impairment in Alzheimer disease by using quantitative MR R2′ mapping." *Med. Sci.*

Rauscher A, Barth M, Herrmann KH, Witoszynskyj S, Deistung A, Reichenbach JR. 2008. "Improved elimination of phase effects from background field inhomogeneities for susceptibility weighted imaging at high magnetic field strengths." *Magn Reson Imaging* 26: 1145–1151.

Rauscher A, Sedlacik J, Barth M, Mentzel HJ, Reichenbach JR. 2005. "Magnetic susceptibility-weighted MR phase imaging of the human brain." *AJNR Am J Neuroradiol* 26(4): 736-42.

Samir D. Sharma, Roland Fischer, Bjoern P. Schoennagel, Peter Nielsen, Hendrik Kooijman, Jin Yamamura, Gerhard Adam, Peter Bannas, Diego Hernando, Scott B. Reeder. 2017. "MRI-based quantitative susceptibility mapping (QSM) and R2* mapping of liver iron overload: Comparison with SQUID-based biomagnetic liver susceptometry." *Magn. Reson. Med* 264-270.

Schafer A, Wharton S, Gowland P, Bowtell R. 2009. "Using magnetic field simulation to study susceptibility-related phase contrast in gradient echo MRI ." *Neuroimage* 48(1): 126-37.

Schweser F, A. Deistung, K. Sommer and J. R. Reichenbach. 2012. "Disentangling contributions from iron and myelin architecture to brain tissue magnetic susceptibility by using Quantitative Susceptibility Mapping (QSM)." *In: Proc. Int. Soc. Magn. Reson. Med* 20.

Schweser Ferdinand, Andreas Deistung, Berengar Wendel Lehr, Jürgen Rainer Reichenbach. 2011. "Quantitative imaging of intrinsic magnetic tissue properties using MRI signal phase: An approach to in vivo brain iron metabolism." *NeuroImage* 2789-2807.

Schweser Ferdinand, Andreas Deistung, Karsten Sommer, and Jurgen Rainer Reichenbach,. 2013. "Toward online reconstruction of quantitative susceptibility maps: Superfast dipole inversion." *Magnetic Resonance in Medicine* 1581-1593.

Schweser F, Deistung A, Reichenbach JR. 2016. "Foundations of MRI phase imaging and processing for Quantitative Susceptibility Mapping (QSM)." *Z Med Phys* 26(1): 6-34.

Schweser F, Robinson SD, de Rochefort L, Li W, Bredies K. 2017. "An illustrated comparison of processing methods for phase MRI and QSM: removal of background field contributions from sources outside the region of interest." *NMR Biomed.*

Sedlacik, J., Boelmans, K., Löbel, U., Holst, B., Siemonsen, S., Fiehler, J. 2014. "Reversible, irreversible and effective transverse relaxation rates in normal aging brain at 3T." *Neuroimage* 1032–1041.

Shen, B., Pan, Y., Jiang, X., Wu, Z., Zhu, J., Dong, J., Zhang, W., Xu, P., Dai, Y., Gao, Y., Xiao, C., & Zhang, L. 2020. "Altered putamen and cerebellum connectivity among different subtypes of Parkinson's disease. ." *CNS neuroscience & therapeutics* 207-214.

Shin HG, Lee J, Yun YH, Yoo SH, Jang J, Oh SH, Nam Y, Jung S, Kim S, Fukunaga M, Kim W, Choi HJ, Lee J. 2021. "χ-separation: Magnetic susceptibility source separation toward iron and myelin mapping in the brain." *Neuroimage.*

Shmueli K, de Zwart JA, van Gelderen P, Li TQ, Dodd SJ, Duyn JH. 2009. "Magnetic susceptibility mapping of brain tissue in vivo using MRI phase data." *Magn Reson Med* 62(6): 1510-22.

Sun H, Wilman AH. 2014. "Background field removal using spherical mean value filtering and Tikhonov regularization." *Magn Reson Med* 71(3): 1151-1157.

Van Obberghen E, Mchinda S, le Troter A, Prevost VH, Viout P, Guye M, Varma G, Alsop DC, Ranjeva JP, Pelletier J, Girard O, Duhamel G. 2018. "Evaluation of the Sensitivity of

Inhomogeneous Magnetization Transfer (ihMT) MRI for Multiple Sclerosis." *AJNR Am J Neuroradiol* 39(4): 634-64.

Wang Y, Liu T. 2015. "Quantitative susceptibility mapping (QSM): Decoding MRI data for a tissue magnetic biomarker." *Magn Reson Med* 73(1): 82-101.

Weiskopf N., Suckling J., Williams G., Correia M. M., Inkster B., Tait R., et al. 2013. "Quantitative multi-parameter mapping of R1, PD*, MT, and R2* at 3T: a multi-center validation." *Front. Neurosci.*

Weiskopf, N., Callaghan, M. F., Josephs, O., Lutti, A., & Mohammadi, S. 2014. "Estimating the apparent transverse relaxation time (R2(*)) from images with different contrasts (ESTATICS) reduces motion artifacts." *Frontiers in neuroscience.*

Welker KM, Patton A. 2012. "Assessment of normal myelination with magnetic resonance imaging." *Semin Neurol* 32(1): 15-28.

WG, Hopkins. 2000. "Measures of reliability in sports medicine and science." *Sports Med* 30: 1–15.

Williams R, Buchheit CL, Berman NE & LeVine SM. 2012. "Pathogenic implications of iron accumulation in multiple sclerosis." *J Neurochem* 120: 7-25.

Wisnieff C, Ramanan S, Olesik J, Gauthier S, Wang Y, Pitt D. 2015. "Quantitative susceptibility mapping (QSM) of white matter multiple sclerosis lesions: Interpreting positive susceptibility and the presence of iron." *Magn Reson Med* 74(2): 564-70.

Yan F, He N, Lin H, Li R. 2018. "Iron deposition quantification: Applications in the brain and liver." *J Magn Reson Imaging* 48(2): 301-317.

Yao B, Li T, Gelderen P Van, Shmueli K, de Zwart JA, Duyn JH. 2009. "Susceptibility contrast in high field MRI of human brain as a function of tissue iron content." *Neuroimage* 44: 1259–66.

Zhang Y, Rauscher A, Kames C, Weber AM. 2019. "Quantitative Analysis of Punctate White Matter Lesions in Neonates Using Quantitative Susceptibility Mapping and R2* Relaxation." *AJNR Am J Neuroradiol* 40(7): 1221-1226.

3 Conclusion

The purpose of this work was facilitating QSM as a contrast method to identify iron and myelin inside brain by splitting the QSM signal into diamagnetic and paramagnetic components. Although QSM is relatively new compared to relaxation measures T_1, T_2 and T_2*, it offers unique contrast directly related to tissue magnetic susceptibility value, and is seeing widespread use, even in clinical studies.

Conventional QSM uses a typical pipeline to find a net susceptibility map from the phase image. This net susceptibility map doesn't contain direct information about the individual paramagnetic and diamagnetic sources in a voxel. Instead, it provides the net sum of all para- and diamagnetic components. Susceptibility separation methods (Emmerich J 2021; Shin HG 2021) have been recently introduced in order to address this problem. The methods use information in the R_2' map along with a QSM pipeline to extract paramagnetic and diamagnetic sources in each voxel. So far, the repeatability of the methods has not been assessed. High reliability is necessary for further usage of this method in clinical studies, particularly if the ultimate goal is tracking changes in an individual. The focus of this thesis was the assessment of reliability of susceptibility separation in brain.

In chapter 2 the separation method (Shin HG 2021) was compared with conventional QSM. Although the method was able to achieve a paramagnetic and diamagnetic map and as a result a total map, it was not as reliable as conventional QSM. Intraclass correlation (ICC) scores (McGraw, 1996) were calculated for conventional QSM, total separation, paramagnetic and diamagnetic components. Overall, the best scores belonged to conventional QSM in both DGM and WM regions with average scores of 0.97 and 0.88, respectively. The diamagnetic component had the least scores in both DGM and WM regions with average scores of 0.45 and 0.45, respectively. Paramagnetic component and total separation had smaller scores than conventional QSM in all the measured regions in DGM. The DGM ICC scores for conventional QSM fell in the range of [0.93, 0.99] ([0.98, 0.99] excluding thalamus) whereas the corresponding ranges for paramagnetic component and total separation were [0.59, 0.98] ([0.89, 0.98] excluding thalamus) and [0.92, 0.98] ([0.97, 0.98] excluding thalamus), respectively. In WM the ICC scores for conventional QSM were in the range of [0.85, 0.91] while the corresponding ranges for

diamagnetic, paramagnetic components and total separation were [0.27, 0.70], [0.48, 0.69] and [0.72, 0.91], respectively. In addition, the effects of the relaxometric coefficient were investigated. The results showed the relaxometric coefficient tends to be larger for dominant component and smaller for minor component e.g. in deep gray matter where strong paramagnetic sources exist, D_r is larger for paramagnetic component than diamagnetic. While in white matter where diamagnetic sources are dominant, D_r is larger for diamagnetic component than paramagnetic.

A major limitation occurred when one of the diamagnetic or paramagnetic components is expected to be less than 0.01ppm in an ROI. This caused the opposite component to keep decreasing in order to satisfy R_2' condition. As this reduction had randomness in it, the overall repeatability was reduced. In addition, the repeatability of each component was significantly less than conventional QSM with the diamagnetic component having the least amount of repeatability.

The separation method is sensitive to the perturbations occurring in the magnetic field from outside the voxel including tissue-tissue or air-tissue interfaces. While conventional QSM, due to its background field removal stage, was quite robust to this noise. The perturbations impacting the R_2^* map are propagated to the R_2' map. Since in the separation method R_2' directly affects all the components, the noise easily propagates. Further improvements to removal of background field effects in R2* might improve this situation.

Overall, this work presented some of the issues associated with separation methods and assessed their repeatability. The separation method showed promising performance but the method still has room to improve.

3.1 Limitations

Although many pipelines for every stage of QSM has been designed and developed, QSM suffers from lack of a gold standard. Calculation Of Susceptibility through Multiple Orientation Sampling (COSMOS) (Liu T S. P., 2019) is considered a gold standard method but it needs several acquisitions with different orientations each time. Maintaining a head tilt for in-vivo experiments is difficult and multiple experiments are time consuming, thus the COSMOS approach is rarely undertaken. However, recent studies such as the QSM challenge have demonstrated that many

QSM reconstruction methods can approach the ground truth of QSM. Nevertheless, each QSM algorithm leaves some imperfections (QSM Challenge 2.0 Organization Committee, 2021).

Conventional QSM and separation methods do not consider anisotropy effects of susceptibility sources, which is prevalent in white matter (Wisnieff C L. T., 2013; Li W W. B., 2012; Wharton S, 2012; C, 2010; Kaden E, 2020). Without considering anisotropic effects in WM tracts, the QSM methods fail. Furthermore, the assumptions made in separation methods are valid in a static dephasing regime where diffusion effects are negligible (Yablonskiy DA H. E., 1994; Yablonskiy DA S. A., 2018). As a result, orientations and implicit assumptions in QSM methods are major limitations. In addition, the separation method dedicates all the field perturbation effects in R_2' to susceptibility sources whereas, fat-water chemical shift, patient motion, imperfect shimming, air-tissue or vein-tissue interface, etc. could be other factors causing the magnetic field perturbation (Huanzhou Yu, 2008; Filippo Del Grande, 2014; Schenck, 1996; Varsha Jain, 2012; Berglund J, 2020).

Background field removal is a stage that is done before susceptibility inversion. Several methods have been developed for removing the background field (Rauscher A B. M., 2008; Ferdinand Schweser A. D., 2011; Sun H, 2014; Özbay PS, 2017) but none of them can remove background field near edges effectively. They are either inaccurate or erode the image a few voxels. Therefore, in important cortical regions, QSM fails to obtain an accurate map which translates to susceptibility separation inaccuracies as well. The erosion at the edges does not affect QSM in DGM.

All the limitations on conventional QSM affect susceptibility separation methods as well since, separation methods use the processed maps in conventional QSM as the input. A limitation affecting only R_2 mapping is the sequence and parameters used for T_2-w imaging. As shown in chapter 2 the resolution plays a significant role in the regions close to (cerebrospinal fluid) CSF. CSF is known for its very low R_2 relaxation rate (Kwon JW, 2012), and any partial volume effects could alter neighboring voxel mean values. The QSM and R_2^* images used a resolution of $0.94\times0.94\times1.7$ mm^3 while the R_2 map had the resolution of $0.9\times0.9\times3.5$ mm^3 which is more than two times greater in the axial direction. While interpolation can equalize voxel sizes, better results may be achieved by matching acquisition voxel sizes. The original work by Shin also had voxel size of $1\times1\times2$mm^3 for both QSM and R_2 images.

A further limitation is the measurement of R_2' was a 3D sequence was used for R_2^* but only a 2D method for R_2. This led to not only voxel size differences in the slice direction, but also differences in the shape of these voxels, owing to the 2D slice profile.

The separation methods assume susceptibility sources just affect the voxel's relaxation rate which is not true all the time. Beside anisotropic impacts which alter both QSM and R_2', the susceptibility source acts as a dipole creating a magnetic field based on equation [1.26]. In some cases. A susceptibility source could be located at the edge of a voxel as a result the perturbation in the voxel is almost equal with the adjacent voxel. In DGM due to its uniformity and shape, this is less a concern but in WM where tracts are narrow and anisotropic effects are not negligible, the issue becomes important. Another limitation arising from R_2^* is the overestimation of R_2^* values that happens in mono-exponential fitting. Since mono-exponential fitting requires small voxel size to ensure minimal contribution from background perturbations. The small voxel size leads to a low SNR. The overestimation of R_2^* due to the low SNR might lead to slight overestimation of the relaxometric coefficient, D_r (Julian Emmerich P. B., 2021).

An additional limitation for R_2^* and R_2 measures in this work has been the assumption of single component decay. In particular, voxels with myelin present will tend to have trapped myelin water that has a far higher relaxation rate than typical intra-extracellular water (A. Mackay, 1994). Finally, the susceptibility separation method relies on multiple acquisitions which can always be subject to patient motion and registration errors. Alternative methods of susceptibility separation that rely on only one acquisition, using only QSM and R_2^* might overcome this.

3.2 Future Directions

The conventional QSM and separation methods have room for improvement. Separation methods benefit from any improvement on conventional QSM since conventional QSM results are used directly in separation methods. In QSM, edges are the most challenging regions to deal with. Since edges are not well defined in phase unwrapping (first stage in QSM) and usually they have boundary value problems (Li W A. A., 2014). Then during background field removal, edges are not accurately processed and become eroded or otherwise their assigned value is not reliable (Robinson SD, 2017). The erosions are common in DGM QSM, but when QSM in cortical areas

is desired the edges need to be reliable. New QSM algorithms that do not require an independent background removal step may help solve the edge problem with QSM such as single step QSM and machine learning approaches (Chatnuntawech I, 2017; Wei H, 2019).

Considering a localized D_r is a possible development for the separation method. It means each region or even each voxel might have their specific D_r instead of being global. This can to some extent compensate for anisotropic effects of susceptibility sources in WM tracts. However, this needs to be done without sacrificing the accuracy as segmentation might allow for noise and also some regions (such as edges) might not be reliable to have a local D_r. The localization could include both paramagnetic and diamagnetic relaxometric coefficients. D_r adjusts the extent that the separation results are dependent to the R_2' information. Using a localized D_r needs to be implemented with caution since in regions with overestimated R_2' values, D_r is also overestimated which can amplify the noise at the output.

A 3D sequence to acquire R_2 map is desirable for future works. Since, a 3D sequence has the capability to acquire an image with high resolution, it is already the standard for R2* and QSM which were acquired at much higher resolution than 2D R2 maps. Ideally spatial resolution would be matched between both QSM and R_2 images. Being time consuming is a major downside of 3D R2 mapping methods. Use of a 3D dual echo spin echo might be a possible solution, along with further means to reduce scan time. A way to reduce scan time might be using compressed sensing (Lustig M, 2007) or machine learning in image processing (Liu F, 2021). By taking advantage of these novel methods, images can be acquired partially. Then the fully reconstructed version is obtained by using the methods. However, training an artificial network to produce the desired results may require significant effort and time.

The separation method can also be applied to patients with carotid plaque to distinguish intraplaque hemorrhage (IPH), which is the characteristic of vulnerable plaques from calcification which is an indicator for a low risk plaque (Liu XS, 2012). So far, CT imaging is the standard for identification of carotid plaque stenosis but it cannot accurately diagnose IPH (Zhou T, 2019). IPH and calcium have opposite magnetic susceptibility. IPH is highly positive while calcium is highly negative (Liu T S. K., 2012 ; Chen W, 2014). As a result the separation method, when is sufficiently developed, can be applied in order to distinguish the two plaque characteristics.

References

A. Mackay, K. Whittall, J. Adler, D. Li, D. Paty, and D. Graeb. 1994. "In vivo visualization of myelin water in brain by magnetic resonance." *Magnetic Resonance in Medicine* 31: 673–677.

Berglund J, Rydén H, Avventi E, Norbeck O, Sprenger T, Skare S. 2020. "Fat/water separation in k-space with real-valued estimates and its combination with POCS." *Magn Reson Med* 83(2): 653-661.

C, Liu. 2010. "Susceptibility tensor imaging." *Magn. Reson. Med* 63: 1471–7.

Chatnuntawech I, McDaniel P, Cauley SF, Gagoski BA, Langkammer C, Martin A, Grant PE, Wald LL, Setsompop K, Adalsteinsson E, Bilgic B. 2017. "Single-step quantitative susceptibility mapping with variational penalties." *NMR Biomed* 30.

Chen W, Zhu W, Kovanlikaya I, Kovanlikaya A, Liu T, Wang S, Salustri C, Wang Y. 2014 . "Intracranial calcifications and hemorrhages: characterization with quantitative susceptibility mapping." *Radiology* 270: 496-505.

Deshmane, A., Gulani, V., Griswold, M. A., & Seiberlich, N. 2012. "Parallel MR imaging. Journal of magnetic resonance imaging." *JMRI* 36(1): 55–72. doi:https://doi.org/10.1002/jmri.23639.

Emmerich Julian, Peter Bachert, Mark E. Ladd, Sina Straub. 2021. "On the separation of susceptibility sources in quantitative susceptibility mapping: Theory and phantom validation with an in vivo application to multiple sclerosis lesions of different age." *Journal of Magnetic Resonance.*

Filippo Del Grande, Francesco Santini, Daniel A Herzka, Michael R Aro, Cooper W Dean, Garry E Gold, and John A Carrino. 2014. "Fat-suppression techniques for 3-T MR imaging of the musculoskeletal system." *Radiographics* 34: 217-233.

Huanzhou Yu, Ann Shimakawa, Charles A McKenzie, Ethan Brodsky, Jean H Brittain, Scott B Reeder. 2008. "Multiecho water-fat separation and simultaneous R2* estimation with multifrequency fat spectrum modeling." *Magnetic Resonance in Medicine* 60(5): 1122-1134.

Kaden E, Gyori NG, Rudrapatna SU, Barskaya IY, Dragonu I, Does MD, Jones DK, Clark CA, Alexander DC. 2020. "Microscopic susceptibility anisotropy imaging." *Magn Reson Med* 84(5): 2739-2753.

Kwon JW, Yoon YC, Choi SH. 2012. "Three-dimensional isotropic T2-weighted cervical MRI at 3T: comparison with two-dimensional T2-weighted sequences." *Clin Radiol* 67(2): 106-113.

Li W, Avram A V., Wu B, Xiao X, Liu C. 2014. "Integrated Laplacian-based phase unwrapping and background phase removal for quantitative susceptibility mapping." *NMR Biomed* 219-227.

Li W, Wu B, Avram A V, Liu C. 2012. "Magnetic susceptibility anisotropy of human brain in vivo and its molecular underpinnings." *Neuroimage* 59: 2088–97.

Liu F, Kijowski R, El Fakhri G, Feng L. 2021. "Magnetic resonance parameter mapping using model-guided self-supervised deep learning." *Magn Reson Med.* 85(6): 3211-3226.

Liu T, Spincemaille P, De Rochefort L, Kressler B, Wang Y. 2019. "Calculation of susceptibility through multiple orientation sampling (COSMOS): A method for conditioning the inverse problem from measured magnetic field map to susceptibility source image in MRI." *Magn Reson Med* 61: 196–204. doi:10.1002/mrm.21828.

Liu T, Surapaneni K, Lou M, Cheng L, Spincemaille P, Wang Y. 2012 . "Cerebral microbleeds: burden assessment by using quantitative susceptibility mapping." *Radiology* 262: 269-78.

Liu XS, Zhao HL, Cao Y, et al. 2012. "Comparison of carotid atherosclerotic plaque characteristics by high-resolution black-blood MR imaging between patients with first-time and recurrent acute ischemic stroke." *AJNR Am J Neuroradiol* 33: 1257–61.

Lustig M, Donoho D, Pauly JM. 2007. "Sparse MRI: The application of compressed sensing for rapid MR imaging." *Magn. Reson. Med* 58: 1182–95.

McGraw, K. O., & Wong, S. P. . , 1(1), 30. 1996. "Forming inferences about some intraclass correlation coefficients." *Psychological methods* 30-46.

Özbay PS, Deistung A, Feng X, Nanz D, Reichenbach JR, Schweser F. 2017. "A comprehensive numerical analysis of background phase correction with V-SHARP." *NMR Biomed.* 30(4).

QSM Challenge 2.0 Organization Committee, Bilgic, B, Langkammer, C, Marques, JP, Meineke, J, Milovic, C, Schweser, F. 2021. "QSM reconstruction challenge 2.0: Design and report of results." *Magn Reson Med* 86: 1241- 1255.

Rauscher A, Barth M, Herrmann KH, Witoszynskyj S, Deistung A, Reichenbach JR. 2008. "Improved elimination of phase effects from background field inhomogeneities for susceptibility weighted imaging at high magnetic field strengths." *Magn Reson Imaging* 26: 1145–1151.

Robinson SD, Bredies K, Khabipova D, Dymerska B, Marques JP, Schweser F. 2017. "An illustrated comparison of processing methods for MR phase imaging and QSM: Combining array coil signals and phase unwrapping." *NMR Biomed.*

Schenck, John F. 1996. "The role of magnetic susceptibility in magnetic resonance imaging: MRI magnetic compatibility of the first and second kinds ." *Medical Physics* 815-850.

Schweser Ferdinand, Andreas Deistung, Berengar Wendel Lehr, Jürgen Rainer Reichenbach. 2011. "Quantitative imaging of intrinsic magnetic tissue properties using MRI signal phase: An approach to in vivo brain iron metabolism." *NeuroImage* 2789-2807.

Shin HG, Lee J, Yun YH, Yoo SH, Jang J, Oh SH, Nam Y, Jung S, Kim S, Fukunaga M, Kim W, Choi HJ, Lee J. 2021. "χ-separation: Magnetic susceptibility source separation toward iron and myelin mapping in the brain." *Neuroimage.*

Sun H, Wilman AH. 2014. "Background field removal using spherical mean value filtering and Tikhonov regularization." *Magn Reson Med* 71(3): 1151-1157.

Varsha Jain, Osheiza Abdulmalik, Kathleen Joy Propert, and Felix W Wehrli. 2012. "Investigating the magnetic susceptibility properties of fresh human blood for noninvasive oxygen saturation quantification." *Magnetic Resonance in Medicine* 68: 863-867.

Wei H, Cao S, Zhang Y, Guan X, Yan F, Yeom KW, Liu C. 2019. "Learning-based single-step quantitative susceptibility mapping reconstruction without brain extraction." *Neuroimage.*

Wharton S, Bowtell R. 2012. "Fiber orientation-dependent white matter contrast in gradient echo MRI." *Proc. Natl. Acad. Sci. U. S. A.* 109: 18559–64.

Wisnieff C, Liu T, Spincemaille P, Wang S, Zhou D, Wang Y. 2013. "Magnetic susceptibility anisotropy: cylindrical symmetry from macroscopically ordered anisotropic molecules and accuracy of MRI measurements using few orientations." *Neuroimage* 70: 363–76.

Yablonskiy DA, Haacke EM. 1994. " Theory of NMR signal behavior in magnetically inhomogeneous tissues: the static dephasing regime. ." *Magn Reson Med* 749-763.

Yablonskiy DA, Sukstanskii AL. 2018. "Lorentzian effects in magnetic susceptibility mapping of anisotropic biological tissues." *J Magn Reson* 292: 129-136.

Zhou T, Jia S, Wang X, Wang B, Wang Z, Wu T, Li Y, Chen Y, Yang C, Li Q, Yang Z, Li M, Sun G. 2019. "Diagnostic performance of MRI for detecting intraplaque hemorrhage in the carotid arteries: a meta-analysis." *Eur Radiol* 29: 5129-5138.

Bibliography

A. Mackay, K. Whittall, J. Adler, D. Li, D. Paty, and D. Graeb. 1994. "In vivo visualization of myelin water in brain by magnetic resonance." *Magnetic Resonance in Medicine* 31: 673–677.

Abdul-Rahman HS, Gdeisat MA, Burton DR, Lalor MJ, Lilley F, Moore CJ. 2007. "Fast and robust three-dimensional best path phase unwrapping algorithm." *Appl Opt* 46: 6623-6635.

AG, Redfield. 1955. "Nuclear magnetic resonance saturation and rotary saturation in solids." *Phys Rev* 1787-1809.

AH, Walsh AJ & Wilman. 2011. "Susceptibility phase imaging with comparison to R2 mapping of iron-rich deep grey matter." *Neuroimage* 57: 452-461.

Arrighini, G. P., and M. Maestro & R. Moccia. 1968. "Magnetic Properties of Polyatomic Molecules: Magnetic Susceptibility of H2O, NH3, CH4, H2O2." *J. Chem. Phys* 49 (2): 882–889.

Bagher-Ebadian, H., Jiang, Q., Ewing, J.R. 2008. "A modified fourier-based phase unwrapping algorithm with an application to MRI venography." *J. Magn. Reson. Imaging* 27: 649–652.

Berglund J, Rydén H, Avventi E, Norbeck O, Sprenger T, Skare S. 2020. "Fat/water separation in k-space with real-valued estimates and its combination with POCS." *Magn Reson Med* 83(2): 653-661.

Bernstein MA, King KE, Zhou XJ, Fong W. 2005. *Handbook of MRI Pulse Sequences.* Med. Phys.

Bezanson J, Karpinski S, Shah VB, Julia EA. 2012. "A fast dynamic language for technical computing." *ArXiv.*

Bilgic B, Pfefferbaum A, Rohlfing T, Sullivan E V, Adalsteinsson E. 2012. "MRI estimates of brain iron concentration in normal aging using quantitative susceptibility mapping." *Neuroimage* 59: 2625–35.

BingWu, Wei Li, Arnaud Guidon, and Chunlei Liu. 2012. "Whole brain susceptibility mapping." *Magnetic Resonance in Medicine* 137-147.

Biondetti, Emma. 2016. "Optimising MRI susceptibility mapping to image brain arteriovenous malformations." PhD Thesis

Bioucas-Dias JM, Valadao G. 2007. "Phase unwrapping via graph cuts." *IEEE Trans Image Process* 16: 698-709.

Bland JM, Altman DG. 1986. "Statistical methods for assessing agreement between two methods of clinical measurement." *Lancet.* 1: 307–310.

Bloch, F. 1946. "Nuclear Induction." *American Physical Society.*

Brass SD, Chen T, Mulkern RV, et al. 2006. "Magnetic resonance imaging of iron deposition in neurological disorders." *Top Magn Reson Imaging* 31-40.

Brown BW, Jr., Lucero RJ, Foss AB. 1962. "A situation where the Pearson correlation coefficient leads to erroneous assessment of reliability." *J Clin Psychol* 18: 95–97.

Bruton A, Conway JH, Holgate ST. 2000. "Reliability: what is it, and how is it measured?" *Physiotherapy* 86: 94–99.

C, Liu. 2010. "Susceptibility tensor imaging." *Magn. Reson. Med* 63: 1471–7.

Carsten Stüber, Markus Morawski, Andreas Schäfer, Christian Labadie, Miriam Wähnert, Christoph Leuze, Markus Streicher, Nirav Barapatre, Katja Reimann, Stefan Geyer, Daniel Spemann, Robert Turner. 2014. "Myelin and iron concentration in the human brain: a quantitative study of MRI contrast." *Neuroimage* 95-106.

Chatnuntawech I, McDaniel P, Cauley SF, Gagoski BA, Langkammer C, Martin A, Grant PE, Wald LL, Setsompop K, Adalsteinsson E, Bilgic B. 2017. "Single-step quantitative susceptibility mapping with variational penalties." *NMR Biomed* 30.

Chavhan, G. B., Babyn, P. S., Thomas, B., Shroff, M. M., & Haacke, E. M. 2009. "Principles, techniques, and applications of T2*-based MR imaging and its special applications." *Radiographics* 1433-1449.

Chen J, Gong NJ, Chaim KT, Otaduy MCG, Liu C. 2021. "Decompose quantitative susceptibility mapping (QSM) to sub-voxel diamagnetic and paramagnetic components based on gradient-echo MRI data. Neuroimage. Nov 15. 242:118477."

Chen W, Zhu W, Kovanlikaya I, Kovanlikaya A, Liu T, Wang S, Salustri C, Wang Y. 2014 . "Intracranial calcifications and hemorrhages: characterization with quantitative susceptibility mapping." *Radiology* 270: 496-505.

Chen Y, Liu S, Wang Y, Kang Y, Haacke EM. 2018. "STrategically Acquired Gradient Echo (STAGE) imaging, part I: creating enhanced T1 contrast and standardized susceptibility weighted imaging and quantitative susceptibility mapping." *Magn Reson Imaging* 46: 130–139.

CP, Slichter. 1990. *Chapter 6 -Electric quadrupole effects BT - Principles of Magnetic Resonance. In: Principles of Magnetic Resonance.*

David L. Thomas, Enrico De Vita, Ralf Deichmann, Robert Turner, and Roger J. Ordidge. 2005. "3d MDEFT imaging of the human brain at 4.7 T with reduced sensitivity to radiofrequency inhomogeneity." *Magnetic resonance in medicine* 53(6): 1452-1458.

De Rochefort L, Brown R, Prince MR, Wang Y. 2008. "Quantitative MR susceptibility mapping using piece-wise constant regularized inversion of the magnetic field." *Magn. Reson. Med* 60: 1003–9.

De Rochefort L, Liu T, Kressler B, Liu J, Spincemaille P, Lebon V, Wu J, Wang Y. 2010. "Quantitative susceptibility map reconstruction from MR phase data using bayesian regularization: validation and application to brain imaging." *Magn. Reson. Med* 194-206.

Deh K, Ponath GD, Molvi Z, Parel GT, Gillen KM, Zhang S, Nguyen TD, Spincemaille P, Ma Y, Gupta A, Gauthier SA, Pitt D, Wang Y. 2018. "Magnetic susceptibility increases as diamagnetic molecules breakdown: Myelin digestion during multiple sclerosis lesion formation contributes to increase on QSM." *J Magn Reson Imaging* 48(5): 1281-1287.

Deshmane, A., Gulani, V., Griswold, M. A., & Seiberlich, N. 2012. "Parallel MR imaging. Journal of magnetic resonance imaging." *JMRI* 36(1): 55–72. doi:https://doi.org/10.1002/jmri.23639.

Donald W McRobbie, Elizabeth A Moore, and Martin J Graves. 2017. *MRI from Picture to Proton.* Cambridge University Press.

Dong Zhou, Tian Liu, Pascal Spincemaille, and Yi Wang. 2014. "Background field removal by solving the Laplacian boundary value problem." *NMR in Biomedicine* 27(3): 312-319.

Du YP, Jin Z, Hu Y, Tanabe J. 2009. "Multi-echo acquisition of MR angiography and venography of the brain at 3 Tesla." *J Magn Reson Imaging* 30: 449–454.

Duyn JH, van Gelderen P, Li T-Q, de Zwart J a, Koretsky AP, Fukunaga M. 2007. "High-field MRI of brain cortical substructure based on signal phase." *Proc. Natl. Acad. Sci. U. S. A.* 11796–801.

Dymerska, B., Eckstein, K., Bachrata, B., Siow, B., Trattnig, S., Shmueli, K., & Robinson, S. D. 2021. "Phase unwrapping with a rapid opensource minimum spanning tree algorithm (ROMEO)." *Magnetic resonance in medicine* 2294–2308.

Edelkamp S, Schroedl S. 2011. *Bucket data structures In: Heuristic Search: Theory and Applications.* Burlington, Massachusetts: Morgan Kaufmann Publishers.

Elkady AM, Cobzas D, Sun H, Blevins G, Wilman AH. 2018. "Discriminative analysis of regional evolution of iron and myelin/calcium in deep gray matter of multiple sclerosis and healthy subjects." *J Magn Reson Imaging.*

Elkady AM, Cobzas D, Sun H, Blevins G, Wilman AH. 2017. "Progressive iron accumulation across multiple sclerosis phenotypes revealed by sparse classification of deep gray matter." *J Magn Reson Imaging* 46(5): 1464-1473.

Emmerich J, Bachert P, Ladd ME, Straub S. 2021. "On the separation of susceptibility sources in quantitative susceptibility mapping: Theory and phantom validation with an in vivo application to multiple sclerosis lesions of different age." *J Magn Reson.*

Emmerich Julian, Peter Bachert, Mark E. Ladd, Sina Straub. 2020. "On the influence of two coexisting species of susceptibility-producing structures on the R2∗ relaxation rate." *Magnetic Resonance Imaging* 170-177.

Eskreis-Winkler S, Deh K, Gupta A, Liu T, Wisnieff C, Jin M, Gauthier SA, Wang Y, Spincemaille P. 2015. "Multiple sclerosis lesion geometry in quantitative susceptibility mapping (QSM) and phase imaging." *J Magn Reson Imaging* 42(1): 224-9.

F, Fernández-Seara M & Wehrli. 2000. "Postprocessing technique to correct for background gradients in image-based R* 2 measurements." *Magnetic resonance in medicine* 44: 358-366.

Filippo Del Grande, Francesco Santini, Daniel A Herzka, Michael R Aro, Cooper W Dean, Garry E Gold, and John A Carrino. 2014. "Fat-suppression techniques for 3-T MR imaging of the musculoskeletal system." *Radiographics* 34: 217-233.

Gelman N, Gorell JM, Barker PB, et al. 1999. "MR imaging of human brain at 3.0 T: preliminary report on transverse relaxation rates and relation to estimated iron content." *Radiology* 759-767.

Gilbert G, Savard G, Bard C, Beaudoin G. 2012. "Quantitative comparison between a multiecho sequence and a single-echo sequence for susceptibility-weighted phase imaging." *Magn. Reson. Imaging* 722-730.

Goodrich MT, Tamassia R, Goldwasser MH. 2014. *Data Structures and Algorithms in Java.* Hoboken, New Jersey: John Wiley & Sons.

Granziera C, Wuerfel J, Barkhof F, Calabrese M, De Stefano N, Enzinger C, Evangelou N, Filippi M, Geurts JJG, Reich DS, Rocca MA, Ropele S, Rovira À, Sati P, Toosy AT, Vrenken H, Gandini Wheeler-Kingshott CAM, Kappos L, and MAGNIMS Study Group. 2021. "Quantitative magnetic resonance imaging towards clinical application in multiple sclerosis." *Brain* 144(5): 1296-1311.

Griswold MA, Jakob PM, Heidemann RM, et al. 2002. "Generalized autocalibrating partially parallel acquisitions (GRAPPA)." *Magn Reson Med* 47: 1202–1210.

Haacke EM, Mittal S, Wu Z, Neelavalli J, Cheng YC. 2009. "Susceptibility-weighted imaging: technical aspects and clinical applications, part 1." *AJNR Am J Neuroradiol* 30(1): 19-30.

Haacke EM, Xu Y, Cheng YC, Reichenbach JR. 2004. "Susceptibility weighted imaging (SWI)." *Magn Reson Med* 52(3): 612-18.

Haiying Liu, Edward Michel, Sean O. Casey, and Charles L. Truwit. 2002. "Actual imaging slice profile of 2d MRI." *Physics of Medical Imaging* 4682: 767–773.

Helms G., Dathe H., Dechent P. 2008a. "Quantitative FLASH MRI at 3T using a rational approximation of the Ernst equation." *Magn. Reson. Med.* 667–672.

Helms G., Dathe H., Kallenberg K., Dechent P. 2008b. "High-resolution maps of magnetization transfer with inherent correction for RF inhomogeneity and T1 relaxation obtained from 3D FLASH MRI. ." *Magn. Reson. Med* 1396–1407.

HM, Branson. 2013. "Normal myelination: a practical pictorial review." *Neuroimaging Clin N Am* 23(2): 183-95.

Hsieh M-C, Tsai C-Y, Liao M-C, Yang J-L, Su C-H, Chen J-H. 2016. "Quantitative susceptibility mapping-based microscopy of magnetic resonance venography (QSM-mMRV) for in vivo morphologically and functionally assessing cerebromicrovasculature in rat stroke model." *PLoS One.*

Huanzhou Yu, Ann Shimakawa, Charles A McKenzie, Ethan Brodsky, Jean H Brittain, Scott B Reeder. 2008. "Multiecho water-fat separation and simultaneous R2* estimation with multifrequency fat spectrum modeling." *Magnetic Resonance in Medicine* 60(5): 1122-1134.

J Lee, Y Nam, JY Choi, H Shin, T Hwang, J Lee. 2017. "Separating positive and negative susceptibility sources in QSM." *Intl. Soc. Magn. Reson. Med.* 25.

J. Lee, K. Shmueli, M. Fukunaga, P. Gelderen, H. van, Merkle, A.C. Silva, J.H. Duyn. 2010. "Sensitivity of MRI resonance frequency to the orientation of brain tissue microstructure." *Proc. Natl. Acad. Sci* 5130-5135.

J., Duyn JH & Schenck. 2017. "Contributions to magnetic susceptibility of brain tissue." *NMR Biomed* 30.

J.T. Vaughan, M. Garwood, C.m. Collins, W. Liu, L. DelaBarre, G. Adriany, P. Andersen, H. Merkle, R. Goebel, M.b. Smith, and K. Ugurbil. 2001. "7t vs. 4t: RF power, homogeneity, and signal-to-noise comparison in head images." *Magnetic Resonance in Medicine* 46(1): 24-30.

Jafari R, Hectors SJ, Koehne de González AK, Spincemaille P, Prince MR, Brittenham GM, Wang Y. 2021. "Integrated quantitative susceptibility and R2 * mapping for evaluation of liver fibrosis: An ex vivo feasibility study." *NMR Biomed* 34(1).

Jenkinson M, Beckmann CF, Behrens TE, Woolrich MW, Smith SM. 2002. "FSL." *Neuroimage.*

Jezzard P, Balaban RS. 1995. "Correction for geometric distortion in echo planar images from B0 field variations." *Magn Reson Med* 34: 65-73.

Jiji S, Smitha KA, Gupta AK, Pillai VP, Jayasree RS. 2013. "Segmentation and volumetric analysis of the caudate nucleus in Alzheimer's disease." *Eur J Radiol* 1525-1530.

Jing Liu, Tian Liu, Ludovic de Rochefort, James Ledoux, Ildar Khalidov, Weiwei Chen, A. John Tsiouris, Cynthia Wisnie, and Yi Wang. 2012. "Morphology enabled dipole inversion for quantitative susceptibility mapping using structural consistency between the magnitude image and the susceptibility map." *NeuroImage* 2560-2568.

Kaden E, Gyori NG, Rudrapatna SU, Barskaya IY, Dragonu I, Does MD, Jones DK, Clark CA, Alexander DC. 2020. "Microscopic susceptibility anisotropy imaging." *Magn Reson Med* 84(5): 2739-2753.

Karsa, Anita. 2018. "Optimising MRI Magnetic Susceptibility Mapping for Applications in Challenging Regions of the Body." PhD Thesis

Ke Li, Richard D. Dortch, E. Brian Welch, Nathan D. Bryant, Amanda K.W. Buck et.al. 2014. "Multi-parametric MRI characterization of healthy human thigh muscles at 3.0T relaxation, magnetization transfer, fatwater, and diffusion tensor imaging." *NMR in biomedicine* 27(9): 1070–1084.

Khader M. Hasan, Christopher Halphen, Arash Kamali, Flavia M. Nelson, Jerry S.Wolinsky, and Ponnada A. Narayana. 2009. "Caudate Nuclei Volume, Diffusion Tensor Metrics, and T2 Relaxation in Healthy Adults and Relapsing-Remitting Multiple Sclerosis Patients: Implications to Understanding Gray Matter Degeneration." *Journal of magnetic resonance imaging* 29(1): 70–77.

Khan, Ahmad Raza. 2013. "RADIATION INDUCED MORPHOLOGICAL AND BIOCHEMICAL CHANGES IN MOUSE MODEL USING NMR IMAGING AND SPECTROSCOPY."

Klein, R. 2021. "Bland-Altman and Correlation Plot - File Exchange - MATLAB Central [WWW Document]. MATLAB Cent. File Exch."

Koo, T.K., Li, M.Y. 2016. "A Guideline of Selecting and Reporting Intraclass Correlation Coefficients for Reliability Research. ." *J. Chiropr. Med* 155–163.

Kwon JW, Yoon YC, Choi SH. 2012. "Three-dimensional isotropic T2-weighted cervical MRI at 3T: comparison with two-dimensional T2-weighted sequences." *Clin Radiol* 67(2): 106-113.

L, Li. 2001. "Magnetic susceptibility quantification for arbitrarily shaped objects in inhomogeneous fields." *Magn. Reson. Med* 46: 907–16.

Lambrecht V, Hanspach J, Hoffmann A, Seyler L, Mennecke A, Straub S, Marxreiter F, Bäuerle T, Laun FB, Winkler J. 2020. "Quantitative susceptibility mapping depicts severe myelin deficit and iron deposition in a transgenic model of multiple system atrophy." *Exp Neurol* 329.

Lee H, Cho H, Lee MJ, Kim TH, Roh J, Lee JH. 2021. "Differential Effect of Iron and Myelin on Susceptibility MRI in the Substantia Nigra." *Radiology* 301(3): 682-691.

Lehéricy S, Roze E, Goizet C, Mochel F. 2020. "MRI of neurodegeneration with brain iron accumulation." *Curr Opin Neurol* 33(4): 462-473.

Leutritz, T., Seif, M., Helms, G., Samson, R. S., Curt, A., Freund, P., & Weiskopf, N. 2020. "Multiparameter mapping of relaxation (R1, R2*), proton density and magnetization

transfer saturation at 3 T: A multicenter dual-vendor reproducibility and repeatability study." *Hum Brain Mapp* 4232-4247.

Li W, Avram A V., Wu B, Xiao X, Liu C. 2014. "Integrated Laplacian-based phase unwrapping and background phase removal for quantitative susceptibility mapping." *NMR Biomed* 219-227.

Li W, Wu B, Avram A V, Liu C. 2012. "Magnetic susceptibility anisotropy of human brain in vivo and its molecular underpinnings." *Neuroimage* 59: 2088–97.

Li W, Wu B, Liu C. 2011. " Quantitative susceptibility mapping of human brain reflects spatial variation in tissue composition." *Neuroimage* 1645-1656.

Liang Z-P, Lauterbur PC. 2000. *Principles of Magnetic Resonance Imaging: A Signal Processing Perspective.* IEEE Press.

Liu C, Li W, Tong KA, Yeom KW, Kuzminski S. 2015. "Susceptibility-weighted imaging and quantitative susceptibility mapping in the brain." *J Magn Reson Imaging* 42(1): 23-41.

Liu F, Kijowski R, El Fakhri G, Feng L. 2021. "Magnetic resonance parameter mapping using model-guided self-supervised deep learning." *Magn Reson Med.* 85(6): 3211-3226.

Liu J, Liu T, de Rochefort L, et al. 2012. "Morphology enabled dipole inversion for quantitative susceptibility mapping using structural consistency between the magnitude image and the susceptibility map." *Neuroimage* 59: 2560-2568.

Liu S, Buch S, Haacke EM. 2013. "Background field removal based on local complex phase unwrapping and spherical mean value property." *21st Annual Meeting of ISMRM* . Salt Lake City, Utah. 2496.

Liu T, Eskreis-Winkler S, Schweitzer AD, Chen W, Kaplitt MG, Tsiouris AJ, Wang Y. 2013. "Improved subthalamic nucleus depiction with quantitative susceptibility mapping." *Radiology* 269: 216–23.

Liu T, Spincemaille P, De Rochefort L, Kressler B, Wang Y. 2019. "Calculation of susceptibility through multiple orientation sampling (COSMOS): A method for conditioning the inverse problem from measured magnetic field map to susceptibility source image in MRI." *Magn Reson Med* 61: 196–204. doi:10.1002/mrm.21828.

Liu T, Surapaneni K, Lou M, Cheng L, Spincemaille P, Wang Y. 2012 . "Cerebral microbleeds: burden assessment by using quantitative susceptibility mapping." *Radiology* 262: 269-78.

Liu XS, Zhao HL, Cao Y, et al. 2012. "Comparison of carotid atherosclerotic plaque characteristics by high-resolution black-blood MR imaging between patients with first-time and recurrent acute ischemic stroke." *AJNR Am J Neuroradiol* 33: 1257–61.

Liu, T., Liu, J., Rochefort, L. de, Spincemaille, P., Khalidov, I., Ledoux, J.R., Wang, Y. 2011. "Morphology enabled dipole inversion (MEDI) from a single-angle acquisition: Comparison with COSMOS in human brain imaging." *Magnet Reson Med* 66: 777–783.

Liu, Z., Spincemaille, P., Yao, Y., Zhang, Y., Wang, Y. 2018. "MEDI+0: Morphology enabled dipole inversion with automatic uniform cerebrospinal fluid zero reference for quantitative susceptibility mapping." *Magnet Reson Med* 79: 2795-2803.

Ludovic de Rochefort, Tian Liu, Bryan Kressler, Jing Liu, Pascal Spincemaille, Vincent Lebon, Jianlin Wu, and Yi Wang. 2010. "Quantitative susceptibility map reconstruction from MR phase data using bayesian regularization: Validation and application to brain imaging." *Magnetic Resonance in Medicine* 194-206.

Lukas R. Buschle, Felix T. Kurz, Thomas Kampf, Simon M.F. Triphan, Heinz-Peter Schlemmer, Christian Herbert Ziener. 2015. "Diffusion-mediated dephasing in the dipole field around a single spherical magnetic object,." *Magnetic Resonance Imaging* 1126-1145.

Lustig M, Donoho D, Pauly JM. 2007. "Sparse MRI: The application of compressed sensing for rapid MR imaging." *Magn. Reson. Med* 58: 1182–95.

M, Jenkinson. 2003. "Fast, automated, N-dimensional phase-unwrapping algorithm." *Magn Reson Med* 49: 193-197.

Maclaren, J., Herbst, M., Speck, O. and Zaitsev, M. 2013. "Prospective motion correction in brain imaging: A review." *Magn Reson Med* 69: 621-636.

Manjón JV, Coupé P. 2016. "volBrain: An Online MRI Brain Volumetry System." *Front Neuroinform.*

Mansfield P, Grannell PK. 2001. "NMR “diffraction” in solids?" *J. Phys. C Solid State Phys* 422-426.

María-Trinidad Herrero, Carlos Barcia, Juana Mari Navarro. 2002 . "Functional anatomy of thalamus and basal ganglia." *Child’s Nerv Syst* 386–404.

Marques JP, Bowtell RW. 2005. "Application of a Fourier-based method for rapid calculation of field inhomogeneity due to spatial variation of magnetic susceptibility." *Concepts Magn. Reson. Part B Magn. Reson. Eng.* 25B: 65–78.

McGraw, K. O., & Wong, S. P. . , 1(1), 30. 1996. "Forming inferences about some intraclass correlation coefficients." *Psychological methods* 30-46.

McPhee KC, Wilman AH. 2017. "Transverse relaxation and flip angle mapping: Evaluation of simultaneous and independent methods using multiple spin echoes." *Magn Reson Med* 2057-2065.

Mure H, Hirano S, Tang CC, et al. 2011. "Parkinson's disease tremor-related metabolic network: characterization, progression, and treatment effects." *NeuroImage* 1244-1253.

Neema M, Stankiewicz J, Arora A, Dandamudi VS, Batt CE, Guss ZD, Al-Sabbagh A, Bakshi R. 2007. "T1- and T2-based MRI measures of diffuse gray matter and white matter damage in patients with multiple sclerosis." *J Neuroimaging* 17: Suppl 1:16S-21S.

Ogawa S, Menon RS, Tank DW, Kim SG, Merkle H, Ellermann JM, Ugurbil K. 1993. "Functional brain mapping by blood oxygenation level-dependent contrast magnetic resonance imaging. A comparison of signal characteristics with a biophysical model." *Biophys J* 803-812.

Oishi K, Zilles K, Amunts K, Faria A, Jiang H, Li X, Akhter K, Hua K, Woods R, Toga AW, Pike GB, Rosa-Neto P, Evans A, Zhang J, Huang H, Miller MI, van Zijl PC, Mazziotta J, Mori S. 2008. "Human brain white matter atlas: identification and assignment of common anatomical structures in superficial white matter." *Neuroimage* 447-57.

Ordidge RJ, Gorell JM, Deniau JC, et al. 1994. "Assessment of relative brain iron concentrations using T2-weighted and T2*-weighted MRI at 3 Tesla." *Magn Reson Med* 335-341.

Ordidge RJ, Gorell JM, Deniau JC, Knight RA, Helpern JA. 1994. "Assessment of relative brain iron concentrations using T2-weighted and T2*-weighted MRI at 3 Tesla." *Magn Reson Med* 335-41.

Özbay PS, Deistung A, Feng X, Nanz D, Reichenbach JR, Schweser F. 2017. "A comprehensive numerical analysis of background phase correction with V-SHARP." *NMR Biomed.* 30(4).

Paling D, Tozer D, Wheeler-Kingshott C, Kapoor R, Miller DH, Golay X. 2012. "Reduced R2' in multiple sclerosis normal appearing white matter and lesions may reflect decreased myelin and iron content." *J Neurol Neurosurg Psychiatry* 83(8): 785-92.

Paschal CB, Morris CB. 2004. "K-space in the clinic." *J Magn Reson Imaging* 19: 145–159.

PC, LAUTERBUR. 1973. "Image Formation by Induced Local Interactions: Examples Employing Nuclear Magnetic Resonance." *Nature* 190-191.

Pei, M., Nguyen, T.D., Thimmappa, N.D., Salustri, C., Dong, F., Cooper, M.A., Li, J., Prince, M.R., Wang, Y. 2015. "Algorithm for fast monoexponential fitting based on Auto-Regression on Linear Operations (ARLO) of data." *Magn Reson Med* 843-850.

Pruessmann KP, Weiger M, Scheidegger MB, Boesiger P. 1999. "SENSE: sensitivity encoding for fast MRI." *Magn Reson Med* 42: 952–962.

Qin, Y., Zhu, W., Zhan, C. et al. 2011. "Investigation on positive correlation of increased brain iron deposition with cognitive impairment in Alzheimer disease by using quantitative MR R2′ mapping." *Med. Sci.*

QSM Challenge 2.0 Organization Committee, Bilgic, B, Langkammer, C, Marques, JP, Meineke, J, Milovic, C, Schweser, F. 2021. "QSM reconstruction challenge 2.0: Design and report of results." *Magn Reson Med* 86: 1241- 1255.

Rabi II, Ramsey NF, Schwinger J. 1954. " Use of rotating coordinates in magnetic resonance problems." *Rev Mod Phys* 167-171.

Rauscher A, Barth M, Herrmann KH, Witoszynskyj S, Deistung A, Reichenbach JR. 2008. "Improved elimination of phase effects from background field inhomogeneities for susceptibility weighted imaging at high magnetic field strengths." *Magn Reson Imaging* 26: 1145–1151.

Rauscher A, Sedlacik J, Barth M, Mentzel HJ, Reichenbach JR. 2005. "Magnetic susceptibility-weighted MR phase imaging of the human brain." *AJNR Am J Neuroradiol* 26(4): 736-42.

Robert W. Brown, Yu-Chung N. Cheng, E. Mark Haacke, Michael R. Thompson, Ramesh Venkatesan. 2014. *Magnetic Resonance Imaging: Physical Principles and Sequence Design.* John Wiley & Sons, Inc.

Robinson SD, Bredies K, Khabipova D, Dymerska B, Marques JP, Schweser F. 2017. "An illustrated comparison of processing methods for MR phase imaging and QSM: Combining array coil signals and phase unwrapping." *NMR Biomed.*

RR, Ernst. 2011. "NMR fourier zeugmatography." *J. Magn. Reson* 510–512.

S. Wharton, R. Bowtell. 2015. "Effects of white matter microstructure on phase and susceptibility maps." *Magn. Reson. Med* 1258-1269.

S. Wharton, R. Bowtell. 2012. "Fiber orientation-dependent white matter contrast in gradient echo MRI." *Proceedings of the National Academy of Sciences* 18559-18564.

Salomir R, de Senneville BD, Moonen CT. 2003. "A fast calculation method for magnetic field inhomogeneity due to an arbitrary distribution of bulk susceptibility." *Concepts Magn. Reson* 19B: 26–34.

Samir D. Sharma, Roland Fischer, Bjoern P. Schoennagel, Peter Nielsen, Hendrik Kooijman, Jin Yamamura, Gerhard Adam, Peter Bannas, Diego Hernando, Scott B. Reeder. 2017. "MRI-based quantitative susceptibility mapping (QSM) and R2* mapping of liver iron overload: Comparison with SQUID-based biomagnetic liver susceptometry." *Magn. Reson. Med* 264-270.

Sati P, van Gelderen P, Silva AC, et al. 2013. "Micro-compartment specific T2* relaxation in the brain." *Neuroimage* 77: 268-278.

Schafer A, Wharton S, Gowland P, Bowtell R. 2009. "Using magnetic field simulation to study susceptibility-related phase contrast in gradient echo MRI ." *Neuroimage* 48(1): 126-37.

Schenck, John F. 1996. "The role of magnetic susceptibility in magnetic resonance imaging: MRI magnetic compatibility of the first and second kinds ." *Medical Physics* 815-850.

Schweser F, A. Deistung, K. Sommer and J. R. Reichenbach. 2012. "Disentangling contributions from iron and myelin architecture to brain tissue magnetic susceptibility by using Quantitative Susceptibility Mapping (QSM)." *In: Proc. Int. Soc. Magn. Reson. Med* 20.

Schweser Ferdinand, Andreas Deistung, Berengar Wendel Lehr, Jürgen Rainer Reichenbach. 2011. "Quantitative imaging of intrinsic magnetic tissue properties using MRI signal phase: An approach to in vivo brain iron metabolism." *NeuroImage* 2789-2807.

Schweser Ferdinand, Andreas Deistung, Karsten Sommer, and Jurgen Rainer Reichenbach,. 2013. "Toward online reconstruction of quantitative susceptibility maps: Superfast dipole inversion." *Magnetic Resonance in Medicine* 1581-1593.

Schweser F, Deistung A, Reichenbach JR. 2016. "Foundations of MRI phase imaging and processing for Quantitative Susceptibility Mapping (QSM)." *Z Med Phys* 26(1): 6-34.

Schweser F, Deistung A, Sommer K, Reichenbach JR. 2013. "Toward online reconstruction of quantitative susceptibility maps: Superfast dipole inversion." *Magn. Reson. Med* 1582-1594.

Schweser F, Hagemeier J, Dwyer MG, Bergsland N, Hametner S, Weinstock-Guttman B, Zivadinov R. 2021. "Decreasing brain iron in multiple sclerosis: The difference between concentration and content in iron MRI." *Hum Brain Mapp* 42(5): 1463-1474.

Schweser F, Robinson SD, de Rochefort L, Li W, Bredies K. 2017. "An illustrated comparison of processing methods for phase MRI and QSM: removal of background field contributions from sources outside the region of interest." *NMR Biomed.*

Sedlacik, J., Boelmans, K., Löbel, U., Holst, B., Siemonsen, S., Fiehler, J. 2014. "Reversible, irreversible and effective transverse relaxation rates in normal aging brain at 3T." *Neuroimage* 1032–1041.

Shen, B., Pan, Y., Jiang, X., Wu, Z., Zhu, J., Dong, J., Zhang, W., Xu, P., Dai, Y., Gao, Y., Xiao, C., & Zhang, L. 2020. "Altered putamen and cerebellum connectivity among different subtypes of Parkinson's disease. ." *CNS neuroscience & therapeutics* 207-214.

Shin HG, Lee J, Yun YH, Yoo SH, Jang J, Oh SH, Nam Y, Jung S, Kim S, Fukunaga M, Kim W, Choi HJ, Lee J. 2021. "χ-separation: Magnetic susceptibility source separation toward iron and myelin mapping in the brain." *Neuroimage.*

Shin HG, Lee J, Yun YH, Yoo SH, Jang J, Oh SH, Nam Y, Jung S, Kim S, Fukunaga M, Kim W, Choi HJ, Lee J. 2021. "χ-separation: Magnetic susceptibility source separation toward iron and myelin mapping in the brain." *Neuroimage.*

Shmueli K, de Zwart JA, van Gelderen P, Li TQ, Dodd SJ, Duyn JH. 2009. "Magnetic susceptibility mapping of brain tissue in vivo using MRI phase data." *Magn Reson Med* 62(6): 1510-22.

Smith, S.M. 2002. "Fast robust automated brain extraction." *Hum. Brain Mapp* 17: 143–155.

Snyder J, McPhee KC, Wilman AH. 2021. "T2 quantification in brain using 3D fast spin-echo imaging with long echo trains." *Magn Reson Med.*

SS, Hidalgo-Tabon. 2001. " Theory of gradient coil design methods for magnetic resonance imaging." *Concepts Mag Res Part A* 223-242.

Stanisz GJ, Odrobina EE, Pun J, Escaravage M, Graham SJ, Bronskill MJ, Henkelman RM. 2005. "T1, T2 relaxation and magnetization transfer in tissue at 3T." *Magn Reson Med* 54(3): 507-12.

Sun H, Wilman AH. 2014. "Background field removal using spherical mean value filtering and Tikhonov regularization." *Magn Reson Med* 71(3): 1151-1157.

Sun, Hongfu. 2015. "Quantitative Susceptibility Mapping in Human Brain: Methods Development and Applications." PhD Thesis

TW, Redpath. 1988. "Principles of nuclear magnetic resonance in one and two dimensions." *Magn. Reson. Imaging.*

Van Obberghen E, Mchinda S, le Troter A, Prevost VH, Viout P, Guye M, Varma G, Alsop DC, Ranjeva JP, Pelletier J, Girard O, Duhamel G. 2018. "Evaluation of the Sensitivity of Inhomogeneous Magnetization Transfer (ihMT) MRI for Multiple Sclerosis." *AJNR Am J Neuroradiol* 39(4): 634-64.

Varsha Jain, Osheiza Abdulmalik, Kathleen Joy Propert, and Felix W Wehrli. 2012. "Investigating the magnetic susceptibility properties of fresh human blood for noninvasive oxygen saturation quantification." *Magnetic Resonance in Medicine* 68: 863-867.

Vinayagamani S, Sheelakumari R, Sabarish S, Senthilvelan S, Ros R, Thomas B, Kesavadas C. 2021. "Quantitative Susceptibility Mapping: Technical Considerations and Clinical Applications in Neuroimaging." *J Magn Reson Imaging* 53(1): 23-37.

Wang Y, Liu T. 2015. "Quantitative susceptibility mapping (QSM): Decoding MRI data for a tissue magnetic biomarker." *Magn Reson Med* 73(1): 82-101.

Wei H, Cao S, Zhang Y, Guan X, Yan F, Yeom KW, Liu C. 2019. "Learning-based single-step quantitative susceptibility mapping reconstruction without brain extraction." *Neuroimage.*

Weiskopf N., Suckling J., Williams G., Correia M. M., Inkster B., Tait R., et al. 2013. "Quantitative multi-parameter mapping of R1, PD*, MT, and R2* at 3T: a multi-center validation." *Front. Neurosci.*

Weiskopf, N., Callaghan, M. F., Josephs, O., Lutti, A., & Mohammadi, S. 2014. "Estimating the apparent transverse relaxation time (R2(*)) from images with different contrasts (ESTATICS) reduces motion artifacts." *Frontiers in neuroscience.*

Welker KM, Patton A. 2012. "Assessment of normal myelination with magnetic resonance imaging." *Semin Neurol* 32(1): 15-28.

WG, Hopkins. 2000. "Measures of reliability in sports medicine and science." *Sports Med* 30: 1–15.

Wharton S, Bowtell R. 2012. "Fiber orientation-dependent white matter contrast in gradient echo MRI." *Proc. Natl. Acad. Sci. U. S. A.* 109: 18559–64.

Williams R, Buchheit CL, Berman NE & LeVine SM. 2012. "Pathogenic implications of iron accumulation in multiple sclerosis." *J Neurochem* 120: 7-25.

Wisnieff C, Liu T, Spincemaille P, Wang S, Zhou D, Wang Y. 2013. "Magnetic susceptibility anisotropy: cylindrical symmetry from macroscopically ordered anisotropic molecules and accuracy of MRI measurements using few orientations." *Neuroimage* 70: 363–76.

Wisnieff C, Ramanan S, Olesik J, Gauthier S, Wang Y, Pitt D. 2015. "Quantitative susceptibility mapping (QSM) of white matter multiple sclerosis lesions: Interpreting positive susceptibility and the presence of iron." *Magn Reson Med* 74(2): 564-70.

Woojin Jung, Steffen Bollmann, Jongho Lee. 2020. "Overview of quantitative susceptibility mapping using deep learning: Current status, challenges and opportunities." *NMR in Biomedicine.*

Yablonskiy DA, Haacke EM. 1994. " Theory of NMR signal behavior in magnetically inhomogeneous tissues: the static dephasing regime. ." *Magn Reson Med* 749-763.

Yablonskiy DA, Sukstanskii AL. 2018. "Lorentzian effects in magnetic susceptibility mapping of anisotropic biological tissues." *J Magn Reson* 292: 129-136.

Yan F, He N, Lin H, Li R. 2018. "Iron deposition quantification: Applications in the brain and liver." *J Magn Reson Imaging* 48(2): 301-317.

Yao B, Li T, Gelderen P Van, Shmueli K, de Zwart JA, Duyn JH. 2009. "Susceptibility contrast in high field MRI of human brain as a function of tissue iron content." *Neuroimage* 44: 1259–66.

Zhang Y, Rauscher A, Kames C, Weber AM. 2019. "Quantitative Analysis of Punctate White Matter Lesions in Neonates Using Quantitative Susceptibility Mapping and R2* Relaxation." *AJNR Am J Neuroradiol* 40(7): 1221-1226.

Zhou T, Jia S, Wang X, Wang B, Wang Z, Wu T, Li Y, Chen Y, Yang C, Li Q, Yang Z, Li M, Sun G. 2019. "Diagnostic performance of MRI for detecting intraplaque hemorrhage in the carotid arteries: a meta-analysis." *Eur Radiol* 29: 5129-5138.

Ziemssen T, Derfuss T, de Stefano N, Giovannoni G, Palavra F, Tomic D, Vollmer T, Schippling S. 2016. "Optimizing treatment success in multiple sclerosis." *J Neurol* 263(6): 1053-65.